MOTION COMPENSATION OF SPOTLIGHT SAR IMAGES IN THE PRESENCE OF UNKNOWN TRANSLATIONAL TARGET MOTION

by

Yi Song

A thesis submitted to the
Department of Electrical and Computer Engineering
in conformity with the requirements
for the degree of Master of Science (Engineering)

Queen's University
Kingston, Ontario, Canada
March 1998

Abstract

This thesis addresses the problem of how to remove the smear in a high-resolution airborne spotlight SAR image, which is caused by the target's constant translational motion. Applications include automatic ship identification from real-time airborne spotlight SAR images. A mathematical model for the two-dimensional impulse response of the image smearing process, which is a function of the target velocity is developed. An algorithm employing a Kalman filter is used to estimate the target velocity. With the estimated target velocity, the smear is removed by inverse filtering the phase of the smeared image. The main part of this thesis proposes a new algorithm of target velocity estimation, which uses target centroid measurements taken from subaperture images. Radar imagery simulations are used to study the relationship between target centroid measurement noise and target velocity. No *a priori* knowledge of target velocity is required for the velocity estimation in this algorithm. To evaluate the performance of the estimator, mismatched measurement noise is used in the Kalman filter, as we do not know the true target velocity. The target velocity variance is calculated analytically for comparison purposes. The accuracy of velocity estimation is found to be inversely proportional to the magnitude of the true velocity. It is shown that with appropriate subaperture integration time intervals, it is possible to restore the smeared images despite the mismatched measurement noise.

Acknowledgements

I would like to thank my supervisor, Dr. Steven Blostein, for his research advice, encouragement, and support during the last two years. Without Dr. Blostein's knowledgeable guidance, this research would not have been successfully completed.

I am grateful to Mr. Mark Earnshaw who taught me a lot about LaTeXand Unix. To my labmates and my friend Julian Cheng, I wish to thank everyone for their friendship and support. I will treasure my memories from Queen's for the rest of my life.

The faculty and staff of the Department of Electrical Engineering are thanked for their help during my studies at Queen's University.

Finally, I would like to thank my parents and my brother for their help and continuous encouragement.

This work was supported by Lockheed Martin Electronic Systems Canada and the School of Graduate Studies and Research at Queen's University.

Contents

List of Tables

List of Figures

Chapter 1

Introduction

1.1 Introduction

The important advantages of microwave radar are that microwaves can penetrate cloud cover, and imaging can be performed at night. However, an impractically large antenna is necessary for a conventional microwave radar to achieve high resolution. Using synthetic aperture radar (SAR) technique, high-resolution images can be created from data collected by a small antenna [2] [10]. SAR technology is used in not only military but also civilian applications. There are three modes of SAR: stripmapping, spotlight mode and inverse SAR (ISAR). The radar platform can be either airborne or spaceborne. Spotlight mode SAR is used for imaging a relatively small patch and can achieve a very high resolution.

The project for this thesis is ship identification using images from airborne spotlight SAR. The imaging targets are ships moving in the sea. To obtain the correct ship classification results, high-resolution SAR images are needed. In spotlight SAR, a long integration time is necessary for a high-resolution image. However, the ship motion during the long integration time will smear the high-resolution image, which is undesired. How can we get the unsmeared high resolution images for moving ships? This is the the problem we are going to solve in this thesis.

In this thesis, a mathematical model for smear effect in airborne spotlight SAR images is examined first. Then a motion compensation scheme is proposed such that smeared images can be restored. The investigation is focussed on constant

translational ship motion. The performance of the proposed scheme is discussed and evaluated.

1.2 Summary of Contributions

This thesis makes the following contributions:

1. A mathematical model of the smear effect due to a target's constant translational motion is derived for airborne spotlight SAR. The image degradation is investigated from a mathematical model first, and then confirmed by simulated images.

2. A novel method is developed to achieve motion compensation such that smeared high-resolution spotlight SAR images of moving targets can be restored. The motion compensation is achieved by target velocity estimation. No *a priori* knowledge of ship velocity is required for the velocity estimation in this method.

3. The analytical target centroid estimation variances for both unsmeared and smeared images are derived. The analysis is verified with results from Monte-Carlo simulations.

1.3 Thesis Outline

The thesis is organized as follows. Background material on SAR, especially on spotlight SAR, is presented in Chapter 2. The proposed scheme for obtaining unsmeared, high-resolution spotlight SAR images is described in Chapters 4 and 5. Chapter 4 discusses ship centroid estimation. Chapter 5 discusses ship velocity estimation by Kalman filtering from ship centroid estimation. Image restoration of the smeared spotlight SAR images are examined in Chapter 5 as well. Finally, Chapter 6 summarizes the results and conclusions of the thesis and makes suggestions for future work.

Chapter 2

SAR Image Formation

2.1 Introduction

In this chapter, the synthetic aperture radar (SAR) image formation background material is presented. First, real-aperture radar is examined. Next, three types of SAR – stripmapping mode, spotlight mode and inverse SAR – are examined from a signal-processing point of view, as opposed to the traditional Doppler point of view. Particular emphasis is put on spotlight mode SAR, since it is the focus of this thesis. Speckle phenomenon and speckle reduction in SAR images are presented as well.

2.2 Real-Aperture Radar

A simplified geometry of a side-looking real-aperture radar is shown in Figure 2.1. The radar is carried on a platform which is moving at speed V at a constant altitude. The radar platform can be either airborne or spaceborne. We assume a *broadside* geometry in which the radar beam is directed perpendicular to the flight path of the platform. The radar transmits the pulses and the return echoes are sampled. The coordinate along the line of sight of the radar is termed *slant range*. The coordinate perpendicular to range is called *cross-range*. Figure 2.1 shows the relationship between *slant range* and *ground range*. Slant range indicates the distance between the radar and the target. Ground range is the slant range projected onto the ground plane. In this thesis, unless indicated otherwise, the term *range* means slant range.

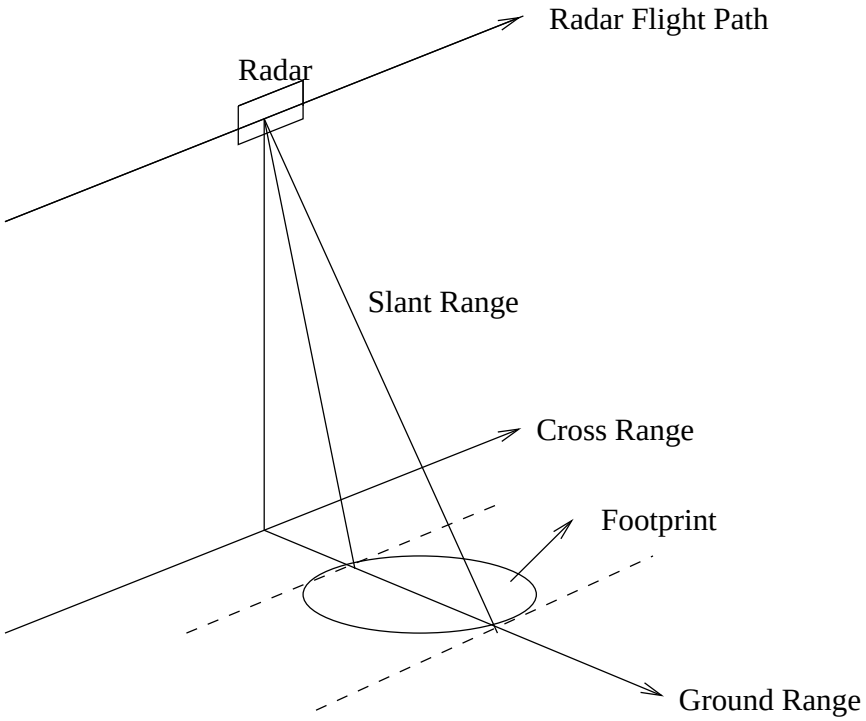

Figure 2.1: Geometry of a side-looking real-aperture radar

2.2.1 Range Resolution

A radar determines the target's range by measuring the time that a transmitted signal travels the roundtrip distance between the radar and the target. The *range resolution* of the radar is defined as the minimum range separation of two points that can be distinguished as separate by the system. To resolve two points in range from the radar echoes, the arrival time of the leading edge of the pulse echo from the more distant point should be later than the arrival time of the trailing edge of the echo from the nearer point. If the time duration of the radar pulse is τ and the speed of light is C, the minimum separation of the two resolvable points is $C\tau/2$.

To achieve a reasonable range resolution, say 3m, the duration of the pulse should be $10^{-8} sec$, which would be too short to deliver adequate energy per pulse to produce a sufficient echo signal-to-noise ratio (SNR) for reliable detection. A technique known as *pulse compression* is commonly employed to achieve high range resolution with long duration pulses. Instead of a short duration pulse, a large-bandwidth dispersed-energy pulse is transmitted, and the received signal is *pulse compressed* so as to compress the

energy into a much narrower pulse. The duration of the compressed pulse is related to the bandwidth of the transmitted signal. The range resolution is then determined by the compressed pulse, as if it had been the transmitted pulse. Matched filtering (cross correlation) and deramp-FFT are two popular approaches to achieve pulse compression [20] [25].

The linear FM chirp signal is the most commonly used waveform in imaging radar systems, since it can achieve both long duration and broad bandwidth. The long duration is required to deliver adequate energy per pulse, and the broad bandwidth is required to achieve high range resolution. A linear FM chirp with duration τ_c is described by $Re\{s(t)\}$ with

$$s(t) = exp[j(\omega_0 t + \alpha t^2)], -\tau_c/2 \leq t \leq \tau_c/2, \tag{2.1}$$

where α is the chirp rate, and ω_0 is the RF center frequency. Although the signal has duration τ_c, after pulse compression, it can behave like a pulse with duration equivalent to $1/B$, where

$$B = \alpha\tau_c/\pi \tag{2.2}$$

is the bandwidth of the signal (in Hertz). As a result, the range resolution of the radar is

$$\delta R = C/2B. \tag{2.3}$$

It is obvious that high range resolution can be obtained by increasing the bandwidth of the transmitted signal.

2.2.2 Cross-range Resolution

To determine the target's position in cross-range, the real-aperture radar requires the footprint be confined to a very narrow strip of cross-range space. As the radar platform moves, the information at different cross-range positions can be collected.

Like range resolution, *cross-range resolution* is the minimum cross-range separation of two resolvable targets. For real-aperture radar, two targets with the same slant range R, can be resolved only if they are not both in the radar footprint at the same time. That is to say, the cross-range resolution is the width of the radar's

footprint. If the diameter of the radar antenna is D, the width of the radar's footprint is $R\lambda/D$, where λ is the wavelength of the illuminating source. Therefore the achievable cross-range resolution is $R\lambda/D$.

To obtain a reasonable cross-range resolution, say 3m, with $R = 100km$ and microwave wavelength $\lambda = 3cm$, it turns out that $D = 1000m$, which means an impractically large antenna must be used. However, by using SAR signal processing techniques, small antennas can be used to obtain high cross-range resolution. It is the improved cross-range resolution that distinguishes the SAR from the real-aperture radar. SAR resolves targets in the range dimension in the same way as real-aperture radar, and both of them achieve the range resolution given in Equation (2.3).

2.3 Synthetic Aperture Radar

The key observation that led to the development of SAR is Doppler frequency shift [2] [8]. Two point targets at the same range but different cross-range, have different velocities relative to the radar. Therefore, the returned signals from the two targets will have different Doppler frequency shifts. Although SAR research began with a true Doppler frequency shift analysis (a true Doppler effect does exist due to the relative motion of the radar and the target), the Doppler effect is not a requirement for SAR imaging. As we will show later, the SAR imaging mechanism can be totally explained from a signal processing viewpoint [6] [8] [10] [17] [23] [25] instead of from a Doppler viewpoint.

There are three modes of SAR: stripmapping SAR, spotlight mode SAR and inverse SAR (ISAR). For stripmapping and spotlight mode SAR, the radar platform may be either airborne or spaceborne. The distance between the sensor and the target in spaceborne SAR is one or two orders of magnitude larger than that in airborne SAR. As a result, the signal processing algorithms for spaceborne SAR are generally more complicated than for airborne SAR.

2.4 Stripmapping SAR

The oldest and most widely known form of SAR is stripmapping SAR [8] [10] [25] in which the antenna remains fixed with respect to the radar platform so that the antenna beam sweeps out a strip on the ground. The path over which the aircraft flies in order to transmit and receive the collection of pulses becomes the *synthetic aperture*. The time in which the aircraft flies the synthetic aperture is called *integration time*. As the platform moves, a sequence of closely spaced pulses is transmitted so that each point in the scene is illuminated by many pulses. The returned signals are processed using a 2-D correlation algorithm (matched filtering) to produce a high resolution SAR image.

Figure 2.2 shows an intuitive way to understand stripmapping SAR. It is from this viewpoint that a large aperture antenna can be substituted with antenna array. Although the very large aperture antenna necessary for real-aperture radar never physically exists, we can use a series of identical small aperture antennas which are evenly distributed in space to form the large aperture antenna. The signal received by the large antenna is equal to the summation of the signals received by the small antennas. One way to achieve the effect of the antenna array is to let a small antenna be sequentially positioned along the line which defines the antenna array. Data collected by the small antenna must be processed as if it were from one element of the antenna array.

The 2-D correlation operation required for a digital stripmapping SAR processor can be expressed as

$$O(n,m) = \sum_i \sum_j s(i,j) S^*(i-n, j-m, n), \tag{2.4}$$

where s is the 2-D range-compressed received signal, S is the reference function which is the range-compressed system response to an isolated point target, and S^* is the complex conjugate of S. The pixel indices i and j are in the region of support of $s(i,j)$. The range-compression (Section 2.2.1) in stripmapping SAR is achieved by matched filtering. $O(n,m)$ represents the complex-valued output image sampled at range position n and cross-range position m. The third variable in the reference function denotes that S is range-varying.

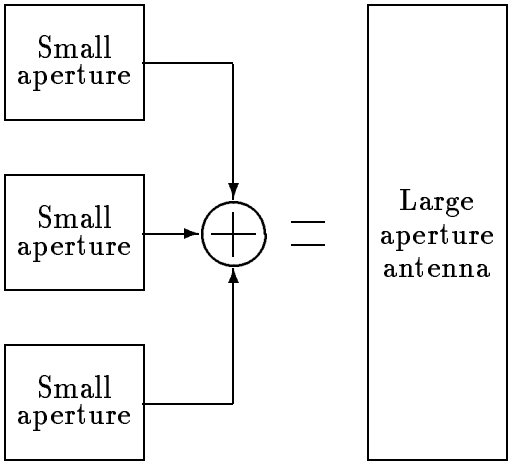

Figure 2.2: Antenna array synthesize a large aperture antenna

The achievable cross-range resolution in stripmapping SAR is $D/2$, where D is the diameter of the antenna aperture. It is achieved when the synthetic aperture is equal to the width of the footprint in cross-range, because this is the maximum distance for which a given point on the ground is in the footprint from all points along the synthetic aperture. The width of the footprint in cross-range is $\lambda R/D$ (Section 2.2.2), thus a finer cross-range resolution requires a larger synthetic aperture. An important condition that accompanies the resolution limit $D/2$ is that pulses must be transmitted with spacing along the flight path also equal to $D/2$ [17]. This is determined from the sampling theorem to avoid spectral aliasing. Thus for a given platform velocity, the finer cross-range resolution requires a higher pulse repetition frequency.

In stripmapping SAR, the size of the footprint is proportional to the range. To achieve the same cross-range resolution, spaceborne SAR needs a much larger synthetic aperture than airborne SAR. Therefore two non-ideal effects, *range curvature* and *range walk* cannot be ignored in spaceborne SAR. Range curvature can be defined as the difference between the range of a stationary point when it is at the center of the footprint, and its range when it is at either edge. The physical reason for range

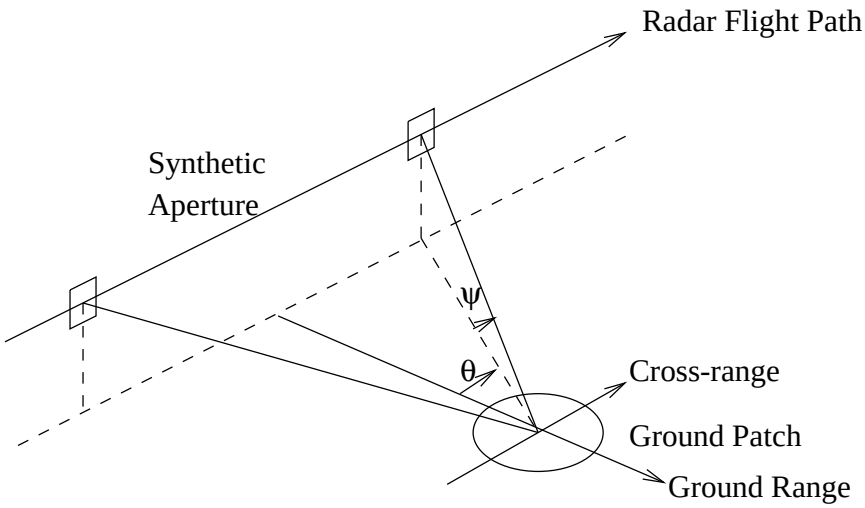

Figure 2.3: Collection geometry of spotlight mode SAR

walk is that a spaceborne SAR takes a much longer time to travel the much larger synthetic aperture. As a result, the movement of the target caused by planetary rotation becomes noticeable. Range walk can be defined as the difference in the range to a point when it leaves the footprint relative to when it enters. Range walk and range curvature together constitute *range migration*. If the total range migration exceeds the range resolution, which is often the case for spaceborne SAR, it must be compensated for in the processing algorithm to avoid image degradation. Range migration correction is only necessary for very high resolution airborne SAR. Therefore, the need to correct for range migration is the primary difference between airborne and spaceborne SAR.

2.5 Spotlight Mode SAR

Stripmapping mode SAR may not be well-suited to all collection scenarios. For the situation where it is desired to image a relatively small patch of the ground with high resolution, spotlight mode SAR [6] [17] [23] is usually a better choice. Figure 2.3 shows the collection geometry for spotlight mode SAR. The antenna is steered to continuously illuminate a single patch of terrain. Thus, the target area is illuminated from different angles. Spotlight mode SAR is able to provide higher resolution than

stripmapping SAR because the synthetic aperture in spotlight mode can be larger than that in stripmapping mode (the synthetic aperture required in stripmapping mode is the width of the radar footprint in cross-range direction).

Munson and his colleagues [23] first analysed the spotlight mode SAR using the *projection-slice theorem* from computer-aided tomography (CAT), and found that spotlight mode SAR is a narrow-band version of CAT. It was shown that the imaging principle employed in spotlight mode SAR is tomographic, rather than Doppler-based. However, in [23], a 2-D terrain reflectivity function was assumed rather than a more general 3-D reflectivity function.

In the following section, a 3-D formulation for spotlight mode SAR [17] is first examined in detail using 3-D extensions of the projection slice theorem. Demodulation errors and autofocus are then discussed.

2.5.1 Extensions of Projection-Slice Theorem

Extensions of the projection-slice theorem from two to three dimensions produce two alternate versions: the *linear trace* version and the *planar slice* version. These two versions are used to explain the 3-D tomographic image formation for spotlight mode SAR.

Consider a complex-valued function in 3-D denoted by $g(x, y, z)$, with its 3-D Fourier transform given by

$$G(X, Y, Z) = \int\int\int g(x, y, z) e^{-j(xX+yY+zZ)} dxdydz \tag{2.5}$$

Linear trace version:

As shown in the top part of Figure 2.4, the linear trace version involves a 1-D projection function formed by integrating $g(x, y, z)$ over two spatial dimensions associated with viewing angles θ and ψ. The theorem states that the 1-D Fourier transform of the projection function is equal to the 3-D Fourier transform $G(X, Y, Z)$ evaluated along a line. As shown in the bottom part of Figure 2.4, the angular orientation of the line in the Fourier transform domain is the same as that of the projection function in the spatial domain. The linear trace version relates linear projection functions to traces of the 3-D Fourier transform.

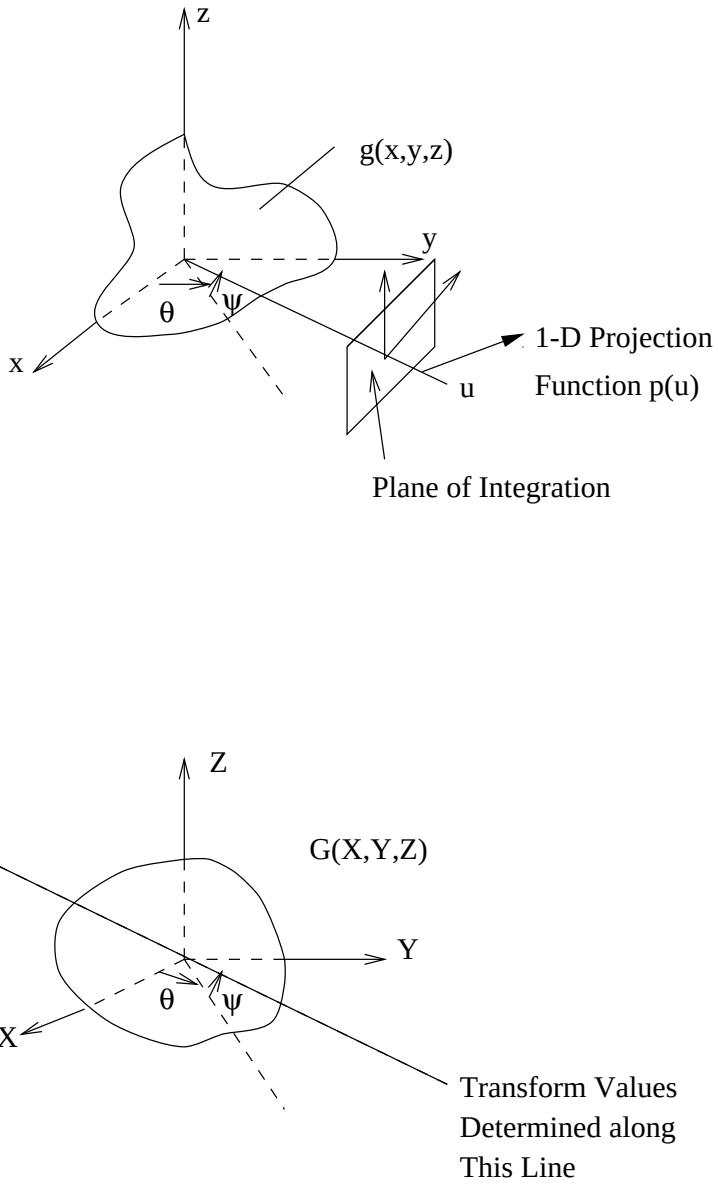

Figure 2.4: Projection-slice theorem (trace version)

Planar slice version:

As shown in the top part of Figure 2.5, the planar slice version involves a 2-D projection function obtained from integrating $g(x, y, z)$ along a single spatial dimension. The bottom part of Figure 2.5 shows a planar slice of the 3-D Fourier transform taken at the same angular orientation as the planar projection of $g(x, y, z)$ above. The theorem states that the planar slice in the Fourier transform is equivalent to the 2-D Fourier transform of the planar projection function.

2.5.2 Spotlight SAR Image Formation

Assume that the 3-D reflectivity function of the scene is modelled by the complex function $g(x, y, z)$ with amplitude function $|g(x, y, z)|$ and phase function $\angle g(x, y, z)$. The radar energy is assumed to be non-penetrating, so the function $g(x, y, z)$ is generally constrained to be zero everywhere except on a surface, and also to be zero at every point on this surface which is shadowed. Furthermore, it is assumed that $g(x, y, z)$ is constant over the range of frequencies and range of viewing angles θ employed by the radar.

The collection geometry in Figure 2.6 describes the scenario that the radar transmits and receives signals at an azimuthal angle θ and a grazing angle ψ. The waveform transmitted by the radar is assumed to be a linear FM chirp pulse given by $Re\{s(t)\}$, where $s(t)$ is described by (2.1).

The returned signal corresponding to radar position (θ, ψ) is

$$r_{\theta,\psi}(t) = A\ Re\{\int_{-u_1}^{u_1} p_{\theta,\psi}(u) s(t - \frac{2(R+u)}{C}) du\}, \tag{2.6}$$

where A is a scale factor that accounts for propagation attenuation and other effects. R is the distance from the radar to the center of the patch. u is the slant range, and u_1 is the maximum slant range for any target illuminated by the beam. $p_{\theta,\psi}(u)$ is the projection function involving 2-D integration of $g(x, y, z)$ over a plane surface associated with viewing angles (θ, ψ). $R + u$ is the distance from the radar to the projection integration plane. To be precise, the surfaces of integration are sections of spheres, since points on the target equidistant from the radar lie on a section of sphere. However, this spherical section can be approximated by a plane, if the patch

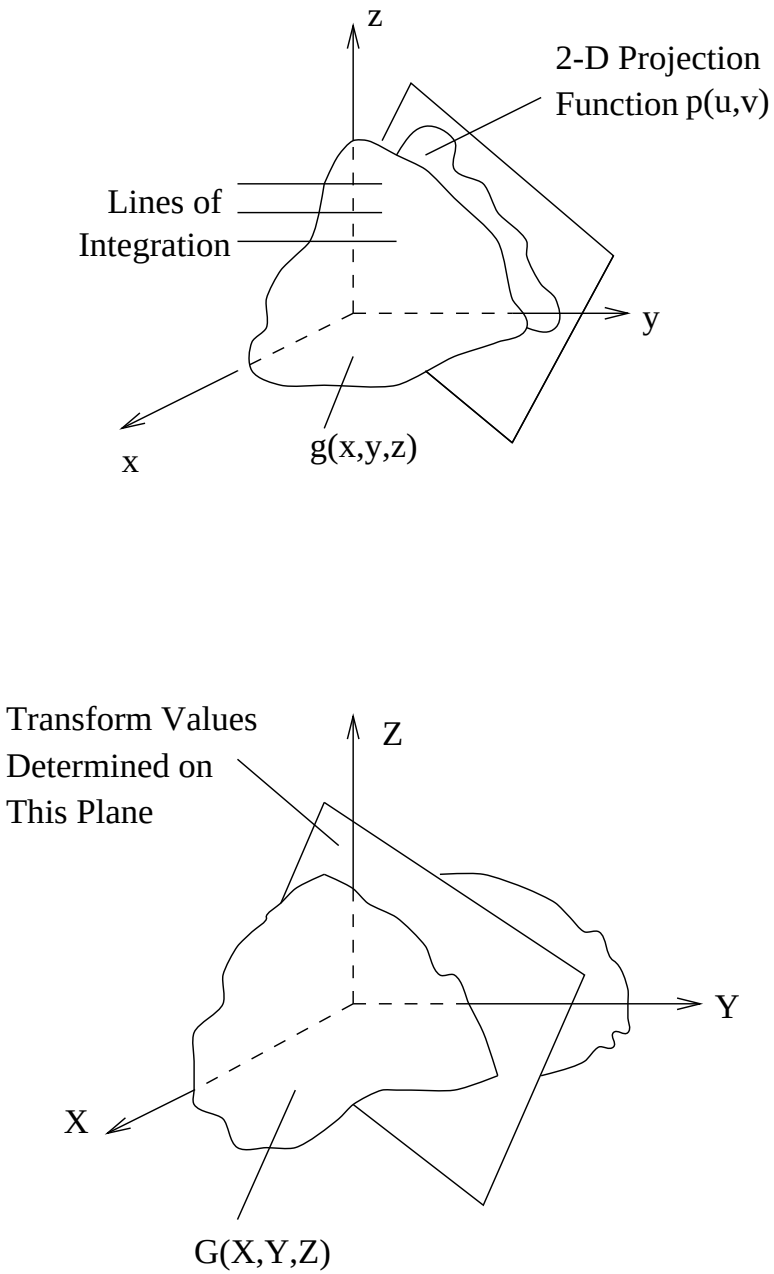

Figure 2.5: Projection-slice theorem (plane version)

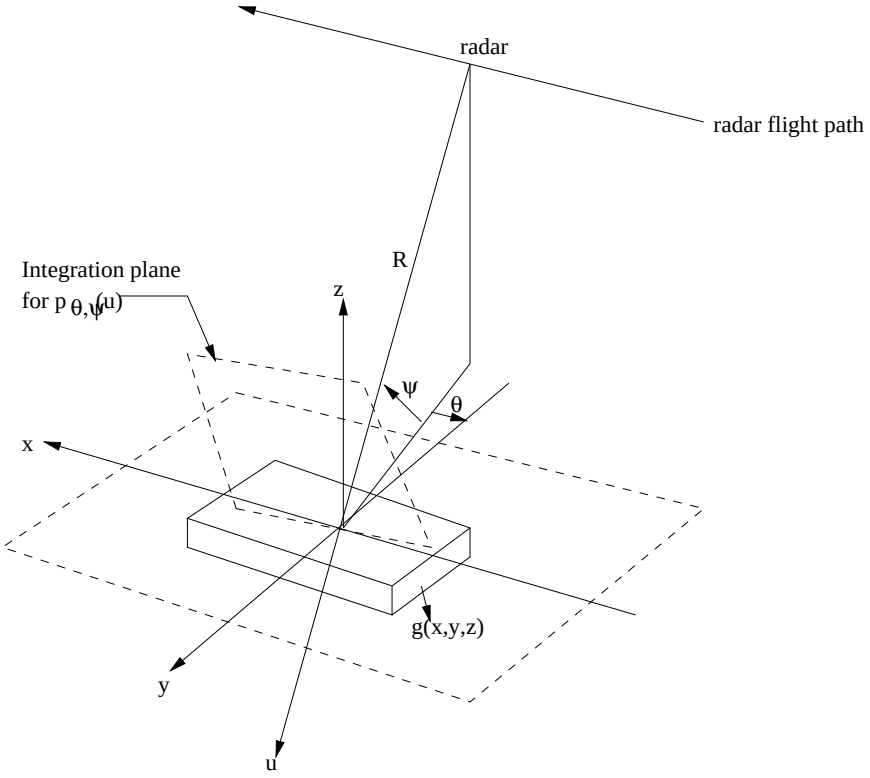

Figure 2.6: Three-dimensional collection geometry of spotlight mode SAR

radius L satisfies the following condition [17]:

$$L \leq \rho_{x'}\sqrt{2R/\lambda}, \tag{2.7}$$

where $\rho_{x'}$ is the cross-range resolution.

Substitution for $s(t)$ from (2.1) into (2.6) gives

$$r_{\theta,\psi}(t) = A\ Re\{\int_{-u_1}^{u_1} p_{\theta,\psi}(u) e^{j\omega_0(t-\tau_0-\frac{2u}{C})+\alpha(t-\tau_0-\frac{2u}{C})^2)} du\}, \tag{2.8}$$

where the modulation time $\tau_0 = \frac{2R}{C}$. However, (2.8) is not valid for all t due to the time restriction of the transmitted signal. The return from the near-edge target exists during $\tau_0 - \tau_p/2 - \tau_c/2 \leq t \leq \tau_0 - \tau_p/2 + \tau_c/2$. The quantity $\tau_p = 2(\frac{2u_1}{C})$ is the difference in two-way propagation delay between a target at the near-edge and a target at the far-edge of the illuminated patch. The return from the far-edge target exists during $\tau_0 + \tau_p/2 - \tau_c/2 \leq t \leq \tau_0 + \tau_p/2 + \tau_c/2$. Thus, the common time segment during which the chirp returns from all targets which exist in the patch simultaneously is

$$\tau_0 - \tau_c/2 + \tau_p/2 \leq t \leq \tau_0 + \tau_c/2 - \tau_p/2. \tag{2.9}$$

In spotlight mode SAR, the size of the illuminated terrain is assumed small such that

$$\tau_c \gg \tau_p. \tag{2.10}$$

Using (2.10), (2.9) is simplified to

$$\tau_0 - \tau_c/2 \leq t \leq \tau_0 + \tau_c/2. \tag{2.11}$$

Thus, the expression of returned signal (2.8) is valid for the time period in (2.11).

Deramp processing is then employed to process the returned signal $r_{\theta,\psi}(t)$. For a given pulse, τ_0 can be determined from the onboard electronic navigation system. The first step in deramp processing is to modulate the returned signal with delayed in-phase and quadrature versions of the transmitted FM chirp,

$$c_I(t) = \cos(\omega_0(t-\tau_0) + \alpha(t-\tau_0)^2) \tag{2.12}$$

and

$$c_Q(t) = -\sin(\omega_0(t-\tau_0) + \alpha(t-\tau_0)^2). \tag{2.13}$$

The second step is to low-pass filter the mixer outputs. As a result, the $c_I(t)$ and $c_Q(t)$ output signals can be represented in complex signal notation as

$$\bar{r}_{\theta,\psi}(t) = \frac{A}{2}\int_{-u_1}^{u_1} p_{\theta,\psi}(u) e^{j[\alpha\frac{2u}{C}^2 - \frac{2u}{C}(\omega_0 + 2\alpha(t-\tau_0))]} du. \tag{2.14}$$

The quadratic phase term in (2.14) can be ignored if the patch radius L satisfies the following condition [17]:

$$L \leq \rho_{x'}\omega_0/(2\sqrt{\pi\alpha}), \tag{2.15}$$

where $\rho_{x'}$ is cross-range resolution.

Ignoring the quadratic phase term, (2.14) is rewritten as

$$\bar{r}_{\theta,\psi}(t) = \frac{A}{2}\int_{-u_1}^{u_1} p_{\theta,\psi}(u) e^{-j\frac{2u}{C}(\omega_0 + 2\alpha(t-\tau_0))} du. \tag{2.16}$$

Furthermore, letting the spatial frequency

$$U = \frac{2}{C}(\omega_0 + 2\alpha(t-\tau_0)), \tag{2.17}$$

Equation (2.16) can be written as

$$\bar{r}_{\theta,\psi}(t) = \frac{A}{2}\int_{-u_1}^{u_1} p_{\theta,\psi}(u) e^{-juU} du = \frac{A}{2} P_{\theta,\psi}(U), \tag{2.18}$$

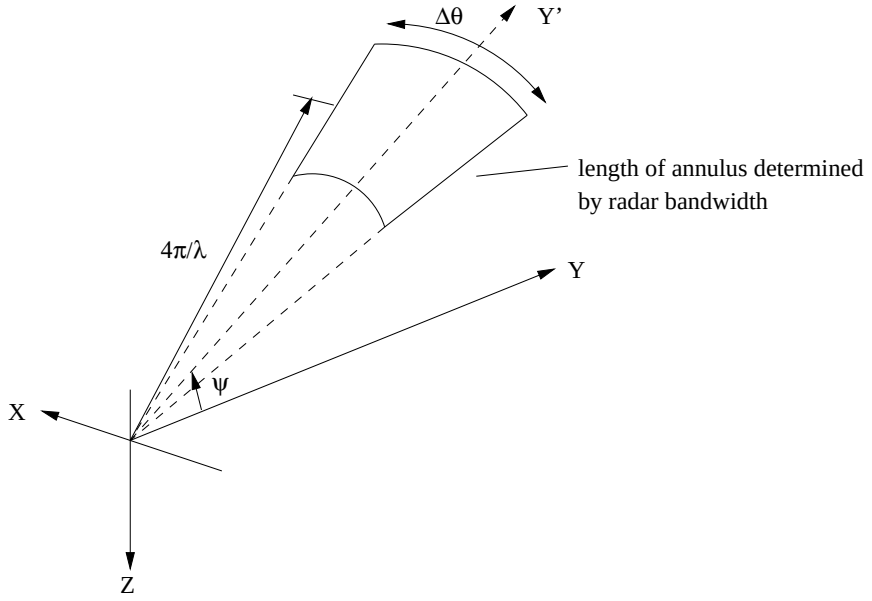

Figure 2.7: A collection of processed pulses sweeps out a ribbon surface in phase-history domain

where $P_{\theta,\psi}(U)$ is the Fourier transform of $p_{\theta,\psi}(U)$. Incorporating (2.11) into (2.17), we obtain a restricted interval in terms of U,

$$\frac{2}{C}(\omega_0 - \alpha\tau_c) \leq U \leq \frac{2}{C}(\omega_0 + \alpha\tau_c). \tag{2.19}$$

From the linear trace version of the projection-slice theorem, $\bar{r}_{\theta,\psi}(t)$ represents a line segment of $G(X,Y,Z)$ at angular orientation (θ,ψ), where the frequency interval is determined by (2.19).

As the radar platform moves through the synthetic aperture, a set of processed radar pulses can be collected over a range of angular orientations. Each processed pulse produces values of $G(X,Y,Z)$ along a certain line segment, the direction of which is determined by the θ and ψ values associated with that pulse transmission point. The collection of pulses will sweep out a ribbon surface in the 3-D Fourier transform space. The precise shape of the ribbon is determined by the platform flight trajectory. The spatial-frequency domain in which the ribbon surface exists is often referred to as the *phase-history domain.*

If the flight path is a straight line through the synthetic aperture, the ribbon surface, as shown in Figure 2.7, lies in a plane. This plane is determined by the line

of the flight path and the center of the patch, and it is called the *slant plane*. In Figure 2.7, all the processed return signals from different angles provide a set of samples of $G(X, Y, Z)$ lying on a polar grid imposed on an annulus segment in the slant plane. The entire annulus is offset from the origin by an amount of $2\omega_0/C = 4\pi/\lambda$. The spatial extent of the annulus in the radial direction is $4\alpha\tau_c/C$, which is proportional to the bandwidth of the transmitted chirp. The angular extent is $4\pi\Delta\theta/\lambda$, which is determined by the range of viewing angles in the synthetic aperture geometry.

The inverse Fourier transform of the data in the slant plane can produce a 2-D SAR image. Consider coordinate axes (X', Y') in the slant plane. The center pulse of the aperture defines the Y' dimension, while the X' axis is orthogonal and also lies in the slant plane. The Y' dimension corresponds to slant range spatial frequencies, while X' corresponds to cross-range spatial frequencies. The 2-D inverse Fourier transform of the data in the slant plane produces an image with x' and y' axes of cross-range and slant range. From the planar slice version of the projection-slice theorem, we know that such a SAR image is an orthogonal projection of the 3-D scene into the slant plane, since the Fourier data $G(X, Y, Z)$ in the slant plane is equal to the 2-D Fourier transform of the projection of $g(x, y, z)$ onto the slant plane.

We define the slant plane patch as the ground patch projected onto the slant plane. The patch radii in (2.7) and (2.15) are in fact slant plane patch radii. Theoretically, an interpolation from the polar collection raster to a Cartesian grid is needed as preprocessing to allow use of the FFT. However, this interpolation can be skipped if the slant plane patch size in the range and cross-range dimensions meet the following conditions [17]:

$$L_{range} \leq 4\rho_{x'}^2/\lambda \tag{2.20}$$

and

$$L_{cross-range} \leq 4\rho_{x'}\rho_{y'}/\lambda, \tag{2.21}$$

where $\rho_{x'}$ is the cross-range resolution, and $\rho_{y'}$ is the range resolution. In general, low-resolution images can be successfully formed by Fourier-transforming the polar data directly, without first performing polar-to rectangular resampling. However, in high-resolution imaging situations, the polar-to-rectangular resampling step is essential.

In spotlight mode SAR image formation, it may seem surprising that acceptable

images can be obtained from a small amount of Fourier data [24]. This is possible because the scene reflectivity in SAR is complex-valued with highly random-like phase, and can be expressed as

$$f(x,y) = m(x,y)e^{j\phi(x,y)}. \tag{2.22}$$

The Fourier transform of $e^{j\phi}$ will have an extremely broad bandwidth due to the randomness of ϕ. The Fourier transform of f, which is the convolution of the Fourier transforms of m and $e^{j\phi}$, will contain magnitude information over a large part of the frequency plane. The random phase acts to modulate the magnitude information over a wide region in Fourier space so that the magnitude of the reflectivity, which is the SAR image, may be recovered from the small number of Fourier samples. However, this reconstruction is a *speckled* version of the scene reflectivity that does not match the true reflectivity magnitude point-for-point. The phenomenon of speckle and speckle reduction will be examined in detail in Section 2.7 and 2.8.

2.5.3 Resolution in Spotlight SAR

It is the extent of the Fourier data annulus in both dimensions that determines the spatial resolutions that can be achieved in the reconstructed image following Fourier inversion. The spatial extent in the range dimension is

$$\Delta Y' = \frac{2}{C} 2\pi B, \tag{2.23}$$

where the bandwidth of the signal B (in Hertz) is given by (2.2). Thus the range resolution is

$$\rho_{y'} = \frac{2\pi}{\Delta Y'} = \frac{C}{2B}. \tag{2.24}$$

As a result, the larger B is, the finer the range resolution becomes.

The nominal cross-range extent is determined by the radius $\frac{4\pi}{\lambda}$ and the angular extent $\Delta\theta$ of the annulus. Since $\Delta\theta$ is typically very small in spotlight mode SAR collections, the spatial extent in cross-range dimension can be approximated by

$$\Delta X' = \frac{4\pi}{\lambda}\Delta\theta. \tag{2.25}$$

Thus the cross-range resolution is

$$\rho_{x'} = \frac{2\pi}{\Delta X'} = \frac{\lambda}{2\Delta\theta}. \tag{2.26}$$

As a result, the larger $\Delta\theta$ is, the finer the cross-range resolution becomes.

In the SAR literature, it is common to refer to an area of size $\rho_{x'}$ by $\rho_{y'}$ in the reconstructed image as a resolution cell.

Though the range resolution in (2.24) is the same as that in (2.3), which is range resolution achieved after pulse compression, it seems that there is no range compression in the image formation of spotlight mode SAR. However, the 2-D inverse Fourier transform can be separated and computed as two 1-D inverse Fourier transforms: one in the range direction, and the other in the cross-range direction. The deramp processing followed by the 1-D inverse Fourier transform in range direction constitutes deramp-FFT, which is one of the pulse compression approaches.

From sampling theory, the minimum spacing of samples along the synthetic aperture to prevent aliasing in the reconstructed image is equal to $D/2$, one-half of the diameter of the physical antenna. It turns out that the same rate is required in stripmapping and spotlight mode SAR. The best cross-range resolution achievable in stripmapping is $D/2$, while this resolution is increased in the spotlight mode SAR.

However, if a large array of samples spanning the desired range and cross-range phase-history extent is downsampled to a similar-sized rectangular grid with fewer samples in each dimension, the resulting image will have the desired resolution but will cover a physically smaller region of scene.

2.5.4 Airborne and Spaceborne SAR

In spotlight mode SAR, the flight path of the platform can be assumed to be a straight line through the synthetic aperture for airborne SAR, while the trajectory of a spaceborne SAR platform cannot be described as a straight-line. Thus for airborne SAR, the phase-history data is simply collected on a plane in the 3-D Fourier space, while it is collected on a non-planar ribbon for spaceborne SAR. An out-of-plane correction is needed for spaceborne SAR to produce a well focussed image. In this thesis, only airborne SAR is considered.

2.5.5 Demodulation Errors and Autofocus

In Section 2.5.2, one assumption dealing with robust image formation is that for each radar pulse, the demodulation time $\tau_0 = 2R/C$ in reference signals (2.12) and (2.13) is known precisely. Errors in estimating R cause demodulation errors. The standard approach for estimating R for each pulse is to employ electronic navigation systems that use inertial measurement units (IMUs) placed on board the collection platform. Even with modern IMU systems, however, the determination of platform position to the required tolerances can prove to be a difficult task. Platform position uncertainty and other effects can cause demodulation errors. For example, propagating radar energy through atmospheric turbulence can cause random delays in the signal. Demodulation errors manifest themselves in exactly the same way from pulse to pulse.

These demodulation errors cause the range-compressed signal to be altered by a constant phase, and shifted by an amount equal to the platform position uncertainty. Usually the shift in the range-compressed pulse is small enough to be ignored. Thus the effect of the demodulation error can be modelled as each range-compressed pulse multiplied by a constant phase. Because a spotlight mode SAR collection comprises many pulses, and each pulse is generally subjected to a different error in demodulation time, a 2-D phase function is induced on the range-compressed phase-history data. This phase function is constant in the range dimension, but can have an arbitrary variation in the cross-range dimension.

The phase errors caused by demodulation errors can be removed by *autofocus algorithms*. There are several practical autofocus techniques [6] [17]. Inverse filtering is the simplest approach. This method needs a strong point-like target that is well-isolated from other surrounding targets. However, such a target is often difficult to find in real defocused SAR images. Mapdrift (MD) (also referred to as subaperture-based technique) and phase difference (PD) are parametric methods. These two approaches assume that the phase-error function in the cross-range dimension can be completely described by a finite polynomial expansion, and both use SAR image data to estimate the polynomial coefficients. Phase gradient autofocus (PGA) is a non-parametric approach that exploits the redundancy of the phase-error function in the range dimension. It is a robust autofocus method. All four of these approaches make

use of the property that the phase error is constant in the range dimension, and only varies in the cross-range dimension. In contrast, prominent point processing (PPP) is an approach that does not use this property. PPP requires three prominent points in the SAR image. The signal from the first prominent point provides a reference signal to compensate for translational motion effects. Signals from two additional prominent points provide an estimate of rotational motion. It may be difficult, however, to find three prominent points in some SAR images.

2.6 Inverse SAR (ISAR)

In spotlight-mode SAR, a fixed ground patch is imaged by sequentially illuminating the patch from different viewing angles. Inverse SAR (ISAR) is the identical problem with the antenna fixed and the target patch moving. That is, ISAR images rotating targets with a fixed antenna. The main problem in this configuration is motion compensation for targets that migrate through more than one resolution cell per illumination time. Significant blurring of images occurs if motion is not correctly compensated. The PPP autofocus technique can be modified to achieve motion compensation in ISAR. ISAR can be interpreted as a tomographic reconstruction problem after the motion compensation.

2.7 Speckle in SAR Images

In this section, we first present certain definitions for SAR images. The SAR image obtained by taking the inverse fast Fourier transform (IFFT) of the phase-history data is the *complex image*, since the result of the IFFT is normally complex-valued. However, when SAR images are displayed, *intensity images* are shown. Intensity images are the squared magnitude of complex images.

In SAR intensity images, the intensity distribution is not smooth. Instead, there are bright and dark spots called *speckle*, such that the SAR images do not match the true scene reflectivity magnitude point to point. Speckle occurs in any form of coherent imaging system, and is due to the roughness of the target surface at the

same order of the illuminating wavelength. For spotlight mode SAR, speckle can be explained from the random phase in the scene reflectivity (Equation (2.22)) and the narrow-band feature of the image formation [23]. Due to the narrow-band feature, the response of spotlight SAR system to a point reflector is approximately a modulated 2-D sinc pulse having the width of a resolution cell. Therefore, responses from adjacent point reflectors in the same resolution cell will overlap and interfere either constructively or destructively. Speckle is formed by random-phased summation of the impulse responses of many point reflectors within a given resolution cell.

The mathematical model for speckle is described in [8] and [9]. If the complex image is denoted as $v(x,y)$, the corresponding intensity image is $I(x,y) = \mid v(x,y) \mid^2$, where x and y indicate the image pixel position. The statistical property of $v(x,y)$ is modelled as a complex Gaussian random variable. The real and imaginary parts of $v(x,y)$ are independent and zero-mean Gaussian with the same variance σ^2. Therefore, the image intensity $I(x,y)$ has an exponential density given by

$$p(I) = \begin{cases} \frac{1}{I_0}\exp(\frac{-I}{I_0}) & I \geq 0 \\ 0 & \text{otherwise} \end{cases} \tag{2.27}$$

where $I_0 = 2\sigma^2$. The mean and variance of the intensity I are:

$$E(I) = I_0 \tag{2.28}$$

$$VAR(I) = I_0^2 \tag{2.29}$$

We can see that the standard deviation of the speckle intensity is equal to the mean I_0. Therefore, the fluctuations of intensity about the mean are quite large, which can make visual interpretation difficult.

2.8 Speckle Reduction

In most applications, speckle is an undesired phenomenon because it reduces image interpretability. A detailed treatment of speckle reduction is beyond the scope of this thesis. A general overview of speckle reduction is presented here, however.

As we know from Section 2.7, the image intensity has an exponential density due to the speckle. In fact, the image intensity $I(x,y)$ in (2.27), where x and y are the

pixel index in a 2-D image, can be represented as a multiplicative noise model [16],

$$I(x,y) = u(x,y)I_0(x,y). \tag{2.30}$$

$I_0(x,y)$ is the mean intensity of pixel (x,y), and $u(x,y)$ is a signal-independent white noise process having a normalized exponential distribution with unit mean and unit variance,

$$p(u(x,y)) = \begin{cases} \exp(-u(x,y)) & u(x,y) \geq 0 \\ 0 & \text{otherwise} \end{cases} \tag{2.31}$$

The speckle reduction problem can be stated as follows: estimate $I_0(x,y)$ from the speckled image $I(x,y)$.

Speckle reduction can be considered as the reduction of signal-dependent noise. There are two approaches to reduce signal-dependent noise [21]. One approach is to transform $I(x,y)$ into a domain where the noise becomes additive signal-independent noise and then to reduce the signal-independent noise. The other approach is to reduce the signal-dependent noise directly in signal domain.

2.8.1 Transformation to Additive Signal-Independent Noise

Multiplicative noise first can be transformed to additive noise by taking logarithms [21],

$$\log I(x,y) = \log I_0(x,y) + \log u(x,y). \tag{2.32}$$

If we denote $\log I(x,y)$ by $I'(x,y)$, and denote $\log I_0(x,y)$ and $\log u(x,y)$ similarly, (2.32) becomes

$$I'(x,y) = I'_0(x,y) + u'(x,y), \tag{2.33}$$

where $u'(x,y)$ is signal-independent additive noise. If we assume that $I'_0(x,y)$ and $u'(x,y)$ are samples of zero-mean stationary random processes, we can use a Wiener filter [1] [12] [21] to get the optimum linear minimum mean-square error (MSE) estimate of $I'_0(x,y)$. The Wiener filter in frequency domain is expressed as:

$$W(u,v) = \frac{S_{I'_0}(u,v)}{S_{I'_0}(u,v) + S_{u'}(u,v)} \tag{2.34}$$

where (u,v) are the Fourier mates of (x,y). $S_{I'_0}(u,v)$ is the power spectrum of signal $I'_0(x,y)$, while $S_{u'}(u,v)$ is the power spectrum of noise $u'(x,y)$. As a result, the estimation $\hat{I}_0(x,y)$ can be obtained by taking the exponential of $\hat{I}'_0(x,y)$, where $\hat{I}'_0(x,y)$ is

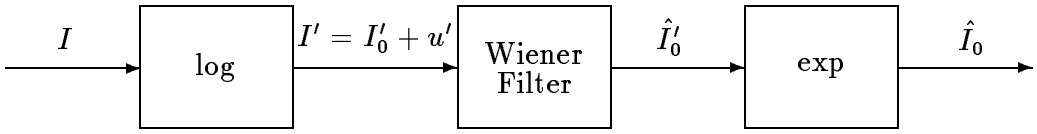

Figure 2.8: Speckle Reduction using Wiener Filter

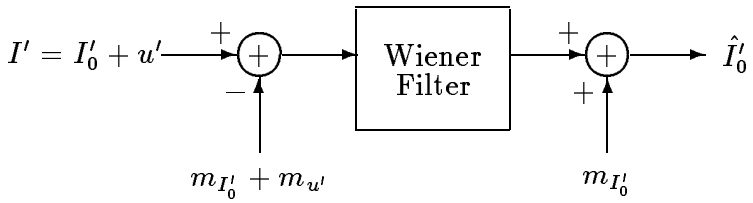

Figure 2.9: Wiener filter for non-zero mean $I'_0(x,y)$ and $u'(x,y)$

the estimation of $I'_0(x,y)$ from Wiener filter, and $\hat{I}_0(x,y)$ is the estimation of $I_0(x,y)$. This is shown in Figure 2.8.

However, if $I'_0(x,y)$ has a mean of $m_{I'_0}$ and $u'(x,y)$ has a mean of $m_{u'}$, then $m_{I'_0}$ and $m_{u'}$ are first subtracted from $I'(x,y)$. The resulting signal $I'(x,y) - (m_{I'_0} + m_{u'})$ is filtered by Wiener filter. The signal mean $m_{I'_0}$ is then added to the filtered signal. This is shown in Figure 2.9. In this case, the Wiener filter in frequency domain is expressed as:

$$W(u,v) = \frac{S_{I'_0 - m_{I'_0}}(u,v)}{S_{I'_0 - m_{I'_0}}(u,v) + S_{u' - m_{u'}}(u,v)} \tag{2.35}$$

Implementation of Wiener filter requires *a priori* knowledge of the power spectrum of the signal and the noise. The method to estimate the signal and noise power spectrum is given in [11] [13].

2.8.2 Reduction of Signal-Dependent Noise in Signal Domain

The multiplicative noise model in (2.30) can also be written directly as an additive noise model:

$$\begin{aligned} I(x,y) &= I_0(x,y) + [u(x,y) - 1]I_0(x,y) \\ &= I_0(x,y) + d(x,y) \end{aligned} \tag{2.36}$$

where the additive noise $d(x,y)$ is signal-dependent. The criterion for estimating $\hat{I}_0(x,y)$ is minimization of the mean square error:

$$\text{error} = \mathbf{E}[(I_0(x,y) - \hat{I}_0(x,y))^2], \tag{2.37}$$

where $\hat{I}_0(x,y)$ is the estimator of $I_0(x,y)$. If we assume that the signal $I_0(x,y)$ and the signal-dependent noise $d(x,y)$ are samples of stationary random processes, then the optimum linear minimum mean square error estimate of $I_0(x,y)$ is

$$\hat{I}_0(x,y) = m_{I_0} + [I(x,y) - m_I] \otimes h(x,y) \tag{2.38}$$

$$H(u,v) = \frac{S_{I_0 I}(u,v)}{S_I(u,v)} \tag{2.39}$$

where $h(x,y)$ indicates a filter, and its expression in frequency domain is given by $H(u,v)$. Parameter $m_{I_0} = \mathbf{E}[I_0(x,y)]$ and $m_I = \mathbf{E}[I(x,y)]$. $S_{I_0 I}(u,v)$ is the cross power spectrum of $I_0(x,y)$ and $I(x,y)$, and $S_I(u,v)$ is the power spectrum of $I(x,y)$. In fact, (2.38) is a Wiener filter solution.

If $I_0(x,y)$ and $d(x,y)$ are not stationary, the filter in (2.38) and (2.39) may be implemented locally in an adaptive manner, where $S_{I_0 I}(u,v)$ and $S_I(u,v)$ are estimated locally [18] [19] [22].

Chapter 3

Impulse Response of Moving Targets in Spotlight Mode SAR

3.1 Introduction

For the image formation algorithm in Section 2.5.2, it is assumed that there is no moving target in the scene. As we know from Equation (2.26), for the given wavelength and radar velocity, the only way to achieve high cross-range resolution in spotlight mode SAR is to use a long integration time. As a result, if the target's motion during the long integration time exceeds the resolution cell, a smeared image will be produced using the image formation algorithm in Section 2.5.2. To restore the smeared images, it is necessary to examine the mathematical model of the smear effect due to target motion.

3.2 Mathematical Model for Moving Targets

A simple collection geometry in slant plane termed *broadside* is shown in Figure 3.1. The radar flight path is level and the center pulse is launched perpendicular to the flight path. In broadside SAR image, the slant range axis is defined to be perpendicular to the flight path, since the center pulse is launched perpendicular to the flight path. In addition to the time variable t, we define another time variable t', which represents the aperture time. It is assumed that the center pulse is launched at $t' = 0$. R_0 is the distance between the radar and the patch center at $t' = 0$. The

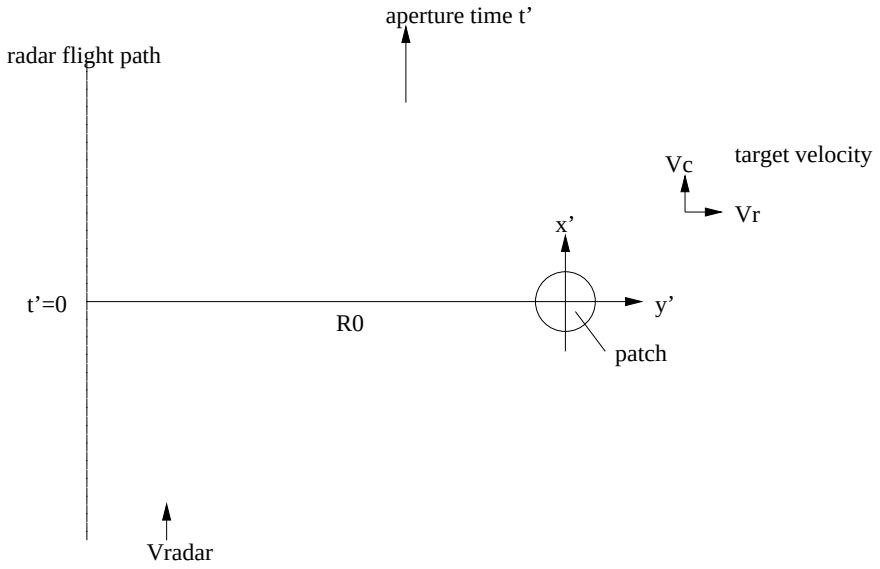

Figure 3.1: broadside collection geometry in slant plane

target is moving at slant range velocity v_r and cross-range velocity v_c. We assume the target only has a translational motion, without any rotational motion. Furthermore, we assume the target is in the patch during the integration time.

For the purpose of examining the smear effect of moving targets in SAR images, we can assume that the scene reflectivity is zero except on the moving targets. This assumption can be justified since we do not care about the image of the scene background. For a translational moving target, the returned signal at radar position (θ, ψ) is

$$r_{\theta,\psi}(t) = ARe\{\int_{-u_1}^{u_1} p_{\theta,\psi}(u) s(t - \frac{2(R + u + \Delta u(u))}{C}) du\}. \tag{3.1}$$

(3.1) is a modification of (2.6), where (2.6) is the returned signal expression for the stationary target. The distance from the radar to the projection integration plane is $R + u$ if the target is stationary, while it is changed to $R + u + \Delta u(u)$ if the target is moving. Δu is the slant range variation due to the target motion. We need to specify a position for the target if it is stationary. A straightforward way to specify this position is to assume that the stationary target is at the same position as that of the moving target at $t' = 0$.

In this case, (3.1) is valid for the same time interval as in (2.11), that is

$$\tau_0 - \tau_c/2 \leq t \leq \tau_0 + \tau_c/2. \tag{3.2}$$

Using the same reference signals as (2.12) and (2.13) to deramp process (3.1), the processed returned signal becomes

$$\bar{r}_\theta(t) = \frac{A}{2}\int_{-u_1}^{u_1} p_\theta(u) e^{j[\alpha\frac{2(u+\Delta u(u))^2}{C} - \frac{2(u+\Delta u(u))}{C}(\omega_0+2\alpha(t-\tau_0))]} du. \tag{3.3}$$

ψ is omitted to simplify the notation, since the radar flight path is level in the collection geometry, which means ψ is the same for every pulse.

If the moving target is in the patch during the integration time, and the patch size satisfies (2.15), the quadratic phase term in (3.3) can be ignored. Thus (3.3) is simplified to

$$\bar{r}_\theta(t) = \frac{A}{2}\int_{-u_1}^{u_1} p_\theta(u) e^{j[-\frac{2(u+\Delta u(u))}{C}(\omega_0+2\alpha(t-\tau_0))]} du. \tag{3.4}$$

As in Section 2.5.2, let the spatial frequency

$$U = \frac{2}{C}(\omega_0 + 2\alpha(t-\tau_0)), \tag{3.5}$$

and (3.4) can be written as

$$\bar{r}_\theta(t) = \frac{A}{2}\int_{-u_1}^{u_1} p_\theta(u) e^{-j(u+\Delta u(u))U} du. \tag{3.6}$$

Obviously, U has the same interval as in (2.19), that is

$$\frac{2}{C}(\omega_0 - \alpha\tau_c) \leq U \leq \frac{2}{C}(\omega_0 + \alpha\tau_c). \tag{3.7}$$

(3.6) could not be further simplified since we do not know the form of Δu.

Now we investigate the slant range variation Δu. An extended target can be considered to be composed of many point targets. Thus, we first examine the slant range variation for a point target.

In Figure 3.1, we define the patch center as the origin of the slant plane. A moving point target is at position (x_0, y_0) at $t' = 0$. That is to say, the point target is at (x_0, y_0) if it is stationary, where x_0 is the cross-range coordinate, and y_0 is the slant range coordinate. The point target is moving at slant range velocity v_r and cross-range velocity v_c. The slant range variation Δu for this point is the distance

difference between the radar to the moving point and the radar to the point if it is stationary. For a radar pulse sent out at aperture time t', Δu is expressed as:

$$\Delta u = \sqrt{(R_0 + y_0 + v_r t')^2 + (V_{radar} t' - v_c t' - x_0)^2} - \sqrt{(R_0 + y_0)^2 + (V_{radar} t' - x_0)^2}. \tag{3.8}$$

In airborne spotlight SAR geometry, the patch size is relative small, thus $R_0 \gg x_0$ and $R_0 \gg y_0$. If the radar velocity is much much greater than the point velocity, and (x_0, y_0) is close to the patch center, Δu can be approximated as (Appendix A):

$$\Delta u \approx v_r t' - \frac{V_{radar} v_c}{R_0} t'^2. \tag{3.9}$$

From (3.9), we can see that Δu is independent of x_0 and y_0, thus Δu is space-invariant. That is to say, Δu is independent of location if the point (x_0, y_0) is stationary. As a result, for a moving extended target (only translational motion), all the points on the target experience the same slant range variation since every point moves at the same velocity. This conclusion can be justified if we consider that the projection functions $p_\theta(u)$ are integrated on planes, and the target has only translational motion. Therefore, Δu is not a function of u. However, Δu varies from pulse to pulse. Using (3.9), (3.6) can be expressed as

$$\bar{r}_\theta(t) = \frac{A}{2} e^{-j\Delta u U} P_\theta(U). \tag{3.10}$$

From the linear trace version of the projection-slice theorem, $\bar{r}_\theta(t)$ represents a line segment of $G(X, Y, Z)$ at angles (θ, ψ) multiplied by an error phase term. The error phase term is related to Δu, which indicates the target's motion. Thus, the phase-history expression for the moving target $G_\epsilon(U)$ can be expressed as

$$G_\epsilon(U) = e^{-j\Delta u U} G(U), \tag{3.11}$$

where $G(U)$ is the phase-history expression if the target is stationary.

As the radar platform moves through the synthetic aperture, a set of processed returned signals can be collected over a range of angular orientations in the phase-history domain. Consider coordinate axes (X', Y') in the slant plane, the center pulse is used to define Y', with X' orthogonal and lying in the plane. Then Y' corresponds to slant range spatial frequencies, and X' corresponds to cross-range spatial frequencies.

After the polar-to-rectangular resampling (in many cases, the effects of the polar to rectangular resampling on the phase-error analysis are negligible), the 2-D phase-history data for the moving target $G_\epsilon(X', Y')$ is expressed as

$$G_\epsilon(X', Y') = e^{-j\Delta u Y'} G(X', Y'). \tag{3.12}$$

The spatial frequency Y' is specified by $\frac{2}{C}(\omega_0 - \alpha\tau_c) \leq Y' \leq \frac{2}{C}(\omega_0 + \alpha\tau_c)$. The extent of the data in the X' dimension is approximated as $\frac{4\pi}{\lambda}\Delta\theta$, thus X' is specified by $-\frac{2\pi}{\lambda}\Delta\theta \leq X' \leq \frac{2\pi}{\lambda}\Delta\theta$. $G(X', Y')$ is the 2-D phase-history data if the target is stationary.

Now we need to express Δu in terms of the spatial frequency X' and Y'. As we know, Δu is a function of t', and t' is related to X'. Thus Δu can be expressed in terms of X'. To find the relationship between t' and X', we assume that T is the integration time. For the broadside collection geometry in Figure 3.1, X' varies from $\frac{2\pi}{\lambda}\Delta\theta$ to $-\frac{2\pi}{\lambda}\Delta\theta$ while t' varies from $-T/2$ to $T/2$. The relationship between X' and t' is expressed by

$$X' = -\frac{t'}{T}\frac{4\pi}{\lambda}\Delta\theta. \tag{3.13}$$

Substituting (3.9) and (3.13) into (3.12), the 2-D phase-history data for the moving target can be rewritten as

$$G_\epsilon(X', Y') = e^{jv_r \frac{T\lambda}{4\pi\Delta\theta} X'Y'} e^{\frac{V_{radar} v_c}{R_0}(\frac{T\lambda}{4\pi\Delta\theta})^2 X'^2 Y'} G(X', Y'). \tag{3.14}$$

From Section 2.5.2, we know that if the target is stationary, the phase-history data will be equal to $G(X, Y, Z)$ in the slant plane. From (3.14) we see that the phase-history data for the moving target is equal to the phase-history data for the stationary target multiplied by a phase-error term. It is the phase-error term that causes the SAR image for moving targets to be smeared.

To obtain the slant plane SAR images for moving targets, we take the inverse Fourier transform of $G_\epsilon(X', Y')$. If we denote $H(X', Y') = e^{jv_r \frac{T\lambda}{4\pi\Delta\theta} X'Y'} e^{\frac{V_{radar} v_c}{R_0}(\frac{T\lambda}{4\pi\Delta\theta})^2 X'^2 Y'}$, the smeared slant plane image for the moving target is given by

$$g_\epsilon(x', y') = IFFT_{X',Y'}\{H(X', Y')\} \otimes g(x', y'), \tag{3.15}$$

where $\otimes$ indicates the discrete convolution operation [26]. x' and y' are the image domain variables for cross-range and slant range. $g_\epsilon(x', y')$ is the smeared image,

and $g(x', y')$ is the unsmeared slant plane image when the target is stationary. From (3.15), we see that the smeared slant plane image is the unsmeared slant plane image convolved with the impulse response due to target motion, where the unsmeared slant plane image is an orthogonal projection of the 3-D scene onto the slant plane when the target is stationary.

3.3 Impulse Response Function

In this section, we are going to examine the impulse response, which is inverse Fourier transform $IFFT_{X',Y'}\{H(X', Y')\}$ in (3.15). X' is the spatial frequency for cross-range, while Y' is the spatial frequency for slant range. In fact, $IFFT_{X',Y'}\{H(X', Y')\}$ is the SAR image for a point target which is at the patch center if it is stationary.

The DFT of a discrete signal is the sampled version of the inverse Fourier transform of the corresponding continuous signal. Thus $IFFT_{X',Y'}\{H(X', Y')\}$ can be examined from $F^{-1}_{X',Y'}\{H(X', Y')\}$ if we look at X' and Y' as continuous variables. Considering X' and Y' as continuous variables, $F^{-1}_{X',Y'}\{H(X', Y')\}$ can be rewritten as:

$$F^{-1}_{X',Y'}\{H(X', Y')\} = F^{-1}_{X',Y'}\{H_1(X', Y')\} * F^{-1}_{X',Y'}\{H_2(X', Y')\}, \tag{3.16}$$

where

$$H_1(X', Y') = e^{jv_r \frac{T\lambda}{4\pi\Delta\theta} X'Y'}, \tag{3.17}$$

and

$$H_2(X', Y') = e^{\frac{V_{radar} v_c}{R_0}(\frac{T\lambda}{4\pi\Delta\theta})^2 X'^2 Y'}. \tag{3.18}$$

the symbol $*$ indicates the continuous convolution operation. Therefore, we can examine $F^{-1}_{X',Y'}\{H(X', Y')\}$ from $F^{-1}_{X',Y'}\{H_1(X', Y')\}$ and $F^{-1}_{X',Y'}\{H_2(X', Y')\}$. $H_1(X', Y')$ is only related to v_r and $H_2(X', Y')$ is only related to v_c. As a result, $F^{-1}_{X',Y'}\{H_1(X', Y')\}$ represents the effect of v_r, and $F^{-1}_{X',Y'}\{H_2(X', Y')\}$ represents the effect of v_c.

In Appendix B, $F^{-1}_{X',Y'}\{H_1(X', Y')\}$ and $F^{-1}_{X',Y'}\{H_2(X', Y')\}$ are examined. We show that v_r causes a image shift in cross-range dimension, which is similar to that in stripmapping SAR [31]. The amount of shift is $v_r R_0 / V_{radar}$, which is proportional to v_r. If the amount of shift exceeds the size of radar footprint (patch size), the image may be reshifted by an integral number of the radar footprints to satisfy the *a priori*

Parameter	Spotlight mode
radar height	3km
radar ground range at $t' = 0$	100km
patch size in slant plane (D)	2km$\times$2km
slant range resolution ($\rho_{y'}$)	0.5m
cross-range resolution ($\rho_{x'}$)	0.5m
radar frequency (f_0)	9.5GHz
radar pulse (FM chirp) width (τ_c)	4×10^{-4}sec
radar velocity (V_{radar})	200m/sec

Table 3.1: Spotlight mode SAR parameters used in this thesis

condition that the target was, in fact, in the radar footprint when it was illuminated by the radar. v_r causes the image to be smeared in the cross-range dimension as well. The smear length is $\frac{\alpha\tau_c}{\omega_0}\frac{v_r}{V_{radar}}R_0$, which is proportional to v_r. The velocity v_c causes the image to be smeared in the cross-range dimension, where the smear length is proportional to v_c. The moving target is smeared in the range dimension in the image domain as well. The smear length is related to the target's moving distance in the range dimension during the integration time, which is related to both v_r and v_c.

3.4 SAR Parameters

The important spotlight SAR parameters used in this thesis are listed in Table 3.1. The radar is at the west of the patch at $t' = 0$. From the parameters in this table, we can calculate some related parameters:

- The radar grazing angle: $\psi = \arctan(3/100) = 1.72$degree
- The wavelength of the illuminating source: $\lambda = C/f_0 = 0.032$m
- The nominal range: $R_0 = \sqrt{100^2 + 3^2} = 100.045$km
- The LFM bandwidth B: $\rho_{y'} = C/2B \Rightarrow B = 300$MHz

- The chirp rate α: $B = \alpha\tau_c/\pi \Rightarrow \alpha = 2.36 \times 10^{12} rad^2/sec^2$
- The antenna aperture d: $D = R_0\lambda/d \Rightarrow d = 1.58$m
- The integration time T: $\rho_{x'} = \lambda/(2\Delta\theta)$ and $\Delta\theta = V_{radar}T/R_0$
  $\Rightarrow \Delta\theta = 0.032$rad and $T = 15.8$sec
- The radar pulse repetition frequency(PRF): $PRF = V_{radar}/(d/2) = 253$Hz
- Number of samples in range: $D/\rho_{y'} = 4000$
- Number of samples in cross-range: $D/\rho_{x'} = 4000$

We need to check whether the assumptions in the SAR image formation are valid with these parameters.

- One assumption we have for the SAR image formation is (2.10), which is $\tau_c \gg \tau_p$. With the above parameters, $\tau_p = 4u_1/C = 4 \times 1000/C = 1.33 \times 10^{-5} sec \ll \tau_c$.
- The projection functions are approximated by integration on planes if the slant plane patch radius L satisfies (2.7), which is $L \leq \rho_{x'}\sqrt{2R/\lambda}$. This condition is most severe when R is at its minimum. For the broadside collection geometry, R reaches its minimum at $t' = 0$. Thus with the above parameters, $R_{min} = 100.045km$, and $\rho_{x'}\sqrt{2R_{min}/\lambda} = 1250m$. Since our slant plane patch radius is 1000m, which is smaller than 1250m, the projection functions can be approximated to be integrals on planes.
- The quadratic phase term in (2.14) can be ignored if the slant plane patch radius L satisfies (2.15), which is $L \leq \rho_{x'}\omega_0/(2\sqrt{\pi\alpha})$. With the above parameters, $\rho_{x'}\omega_0/(2\sqrt{\pi\alpha}) = 5480.4m$. Since our patch radius $1000m$ is much less than this bound, we can ignore the quadratic phase term.

3.5 Simulation Results

With the parameters in Section 3.4, a computer was used to simulate the impulse response for moving targets. The impulse response is also the SAR image for a point

target which is at the patch center if it is stationary. The image size in the following figures is $400m \times 400m$.

Figure (3.2) shows the impulse responses for a point target at different velocities.

The upper-left figure is the SAR image for the stationary point target. It is the unsmeared image for the point target. The point is in the middle of the image, and has no smear.

The upper-right figure is the SAR image if the point target moves at $v_r = 0.2m/sec$ and $v_c = 0$. It is shown that the point target, which is supposed to be at the patch center, is shifted in the cross-range dimension. The amount of shift is around 100m, which is equal to $v_r R_0 / V_{radar}$. The point is smeared in the cross-range dimension as well. The smear length is about 3.2m, which is equal to $\frac{2\alpha\tau_c}{\omega_0}\frac{v_r}{V_{radar}}R_0$. The smear length in the range dimension is equal to the target's moving distance in the range dimension during the integration time. Since $v_c = 0$, the target's moving distance in the range dimension is $v_r T = 3.16m$.

The bottom-left figure is the SAR image if the point target moves at $v_r = 0$ and $v_c = 0.2m/sec$. It is shown that the point is smeared in the cross-range dimension as well as in the range dimension, but there is no image shift. The smear length in the range dimension is equal to the target's moving distance in the range dimension during the integration time. Since $v_r = 0$, the target's moving distance in the range dimension is $\frac{V_{radar} v_c}{R_0}(\frac{T}{2})^2 = 0.025m$, which is much smaller than the range resolution. This is the reason that the smear in the range dimension is not obvious in this figure.

The bottom-right figure is the SAR image if the point target moves at $v_r = 0.2m/sec$ and $v_c = 0.2m/sec$. We can see the smear effect in this figure is the combination of the smear in upper-right figure and bottom-left figure. From the image, we can also see that the point target moves at a 45 degree heading.

The simulated SAR images show that the smear effect due to the target motion cannot be ignored in high resolution SAR images, even with small target velocities. This is a consequence of the long integration time required for a high resolution image. The target motion during such a long time may exceed the size of the resolution cell even with a small velocity. As a result, a smeared image is produced using the conventional image formation.

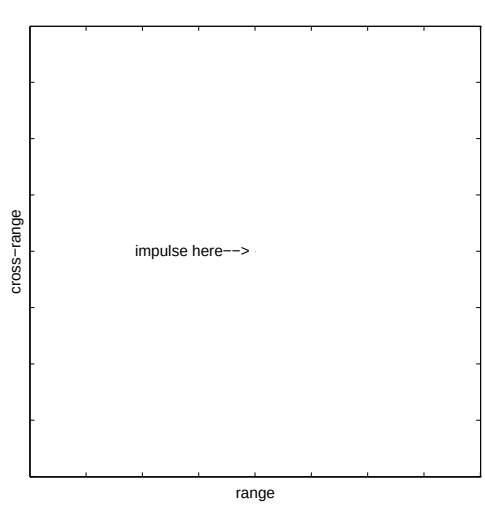

$v_r = v_c = 0$

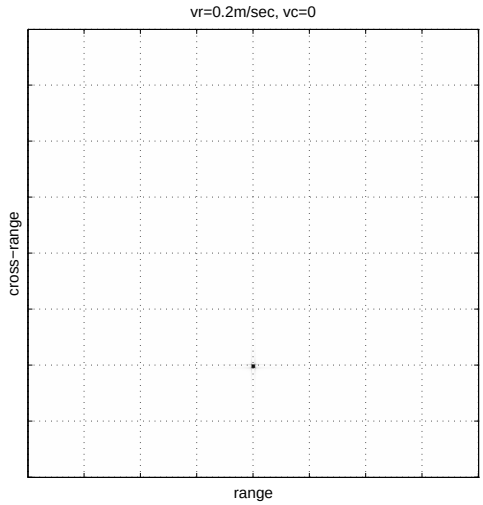

$v_r = 0.2\text{m/sec},\ v_c = 0$

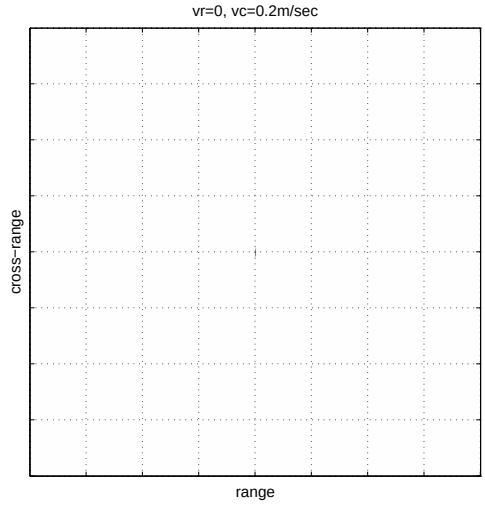

$v_c = 0.2\text{m/sec},\ v_r = 0$

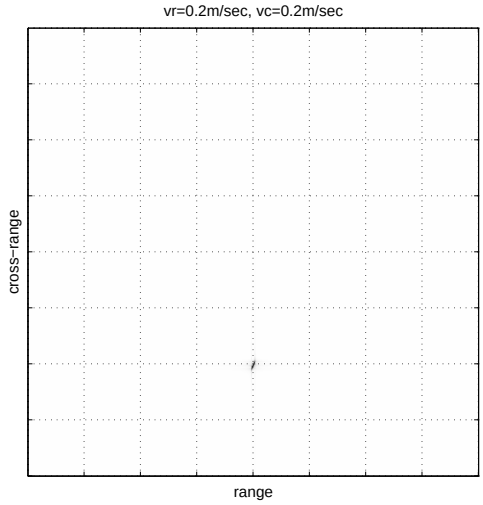

$v_r = v_c = 0.2\text{m/sec}$

Figure 3.2: impulse responses for a point target with different velocities

3.6 Summary

In this section, the mathematical model for the smear effect due to a target's constant translational motion has been investigated for airborne spotlight SAR. Simulated images are used to highlight the main sources of degradation.

The conclusions on smear effect from this chapter are:

- If the target is close to the patch center at aperture time $t' = 0$, and the target velocity is much smaller than the radar velocity, then the phase history data for the moving target is equal to the phase-history data for the stationary target multiplied by a phase-error term. The phase-error term is related to the target velocity. As a result, in the image domain, the smeared image for the moving target is the unsmeared image convolved with an impulse response due to target motion.

- The target slant range velocity v_r causes an image shift in the cross-range dimension. The image shift amount is $v_r R_0 / V_{radar}$. If the amount of shift exceeds the size of radar footprint (patch size), the image may be reshifted by an integral number of radar footprints.

- The target slant range velocity causes image smear in the cross-range dimension. The smear length is $\frac{\alpha \tau_c}{\omega_0} \frac{v_r}{V_{radar}} R_0$.

- The target cross-range velocity, v_c, causes an image smear in the cross-range dimension, where the smear length is proportional to v_c.

- The moving target is smeared in the range dimension in the image domain. The smear length is related to the target's moving distance in the range dimension during the integration time, which is related to both the slant range and the cross-range velocity.

Chapter 4

Ship Centroid Estimation

4.1 Introduction

In Chapter 3, we have shown that we cannot ignore the smear effect caused by target motion in a high resolution SAR image, even if the target is moving at low velocity. This is a consequence of the long integration time required for high resolution images. In practice, we deal with a moving target whose velocity we do not know. How can we restore the smeared image with unknown target motion? This is the focus of the next two chapters.

In this chapter, the state of the art for restoring smeared images due to target motion is reviewed. Then, an overview of the method developed here to remove the smear due to target motion is presented. The first step in this method, ship centroid estimation is examined in this chapter. Simulation results and conclusions for the ship centroid estimation variance are given at the end of the chapter.

In ship centroid estimation, analytical expressions of the centroid estimation variance for both unsmeared and smeared images are derived. The work for unsmeared images is a generalization of [4] and [27], while the work for smeared images, to the best of our knowledge, does not appear in the literature. These analyses are verified by simulation results from Monte-Carlo runs.

4.2 Literature Review

When conventional SAR image formation is applied to a scene with moving targets, the images of the moving targets are typically mislocated in cross-range, and smeared in range and cross-range due to phase errors induced by the motion. The amount of mislocation and smear are related to the target velocity during the integration time.

To restore the smeared images due to target motion, we may consider autofocus (refer to Section 2.5.5). Can autofocus be applied to remove the smear due to target motion? Unfortunately, most of the autofocus methods cannot. Recall that autofocus is a restoration algorithm that can remove the smear due to demodulation error. Demodulation error is normally caused by radar platform motion. Although the smear due to radar platform motion and target motion are both caused by the relative motion between the radar platform and target, reasonable knowledge of radar platform motion can be provided by an inertial navigation system, while target motion is generally unknown. The most important reason why autofocus cannot be applied to remove smear due to target motion is that the phase error in the phase-history domain caused by radar platform motion has a different form from that caused by target motion. In the mathematical model for demodulation error, the phase error in the phase-history domain is constant in the range dimension, and only varies in the cross-range dimension. However, in the mathematical model for a moving target, Equation (3.14) shows that the phase error is a function of both range spatial frequency Y' and cross-range spatial frequency X' instead of being constant in range. Most of the autofocus algorithms make use of the property that the phase error due to demodulation error is constant in the range dimension, thus they cannot be used to remove the smear caused by target motion.

Prominent point processing (PPP) is the only autofocus method that can be applied to remove the smear due to target motion [33]. As one of the autofocus methods, PPP does not exploit the property that the phase error is constant in the range dimension. In PPP, signals from three prominent points on the target are tracked across the synthetic aperture. These signals are used as reference signals to estimate and compensate for the target's translational and rotational motion. The first prominent point is used to measure and remove translational motion effects,

which makes the first point become the scene center. The second prominent point estimates and removes the effects of any nonuniformity in the rotation rate relative to this new scene center. The third prominent point provides a measure of the actual rotation rate. This measurement leads to an estimate of the cross-range scale factor of the resulting image. These motion estimates are used to eliminate motion-induced phase errors, and thus remove the smear. The advantage of PPP is that it can deal with both translational and rotational target motion. However, the disadvantage of this algorithm is that the performance of the algorithm depends on the availability of target prominent points. The chosen prominent points should have high signal-to-background ratio. In real SAR images, such prominent points are not easy to find. In addition, PPP assumes a rigid-body relationship between the three selected prominent points.

The algorithm described in [15] was used to remove smear caused by a target's nonuniform rotation. The integration time was divided into small consecutive sections. The rotation velocity was assumed to be uniform for the small section. The low-resolution images for the small sections were corrected for changes in rotation rates between the consecutive sections. Comparison of changes in the angular position and the scale of the successive target images yielded the change in the rotation rate. A final, high-resolution, compensated image was provided by combining the corrected low-resolution images. The final image obtained would be the image formed if the rotation rate was not varying. This algorithm only compensates for rotational motion, and does not consider translational motion. However, this method uses subaperture processing to estimate the rotation velocity.

Inverse SAR (ISAR) is similar to spotlight SAR, except that in ISAR, the radar is fixed while the target is moving. Motion compensation for targets is also an important issue in ISAR. We briefly review the important literature for motion compensation in ISAR.

Among motion compensation methods used in ISAR, the phase correction method exploits the phase changes of reference points, analogous to PPP [31]. Another method is to estimate the target velocity via centroid tracking [14]. The algorithm provided in [14] compensates for a target's radial motion, where the radial velocity

may not be constant. This is achieved by estimating the radial motion of the target centroid. However, the algorithm estimates the target velocity by a second-order least squares method with only two centroid measurements, and it is questionable whether two centroid measurements can yield good velocity estimation. In addition, the target centroid estimation procedure used was not detailed in the paper.

4.3 An Overview of the Proposed Method

In this thesis, the SAR imaging targets are moving ships at sea. We assume that the dominant ship motion is translational. The rotational motion is assumed to be small enough to be ignored. This assumption is reasonable since a ship's pitch, yaw or roll frequencies may be very low if the sea is calm. Thus, only the smear caused by a ship's translational motion is considered. In addition, in this thesis, we assume that the ship is moving at a constant translational velocity during the long integration time in SAR imaging, and the ship is close to the patch center at aperture time $t' = 0$.

With the above assumptions, Equation (3.14) shows that the error phase term in the phase-history domain is a function of the target velocity. Once we have accurate knowledge of the target velocity, we can compensate the phase error and restore the smeared images. Therefore, in our proposed method, first the ship velocity is estimated, and then the smeared high-resolution image is restored.

Ship velocity is estimated by subaperture processing. The long integration time is divided into a set of consecutive short integration times. Low-resolution subaperture images are formed for the short integration time. The ship centroid is estimated for each subaperture image. Thus, a set of ship centroid measurements can be obtained from the subaperture image sequence. The ship velocity is estimated from these centroid measurements using a Kalman filter. Although the subaperture images have low resolution and may be smeared by ship motion, the smears are not severe due to the minimal target movement during the short integration time. In addition, from the simulation results in Section 3.5, we can see that the smear caused by target motion is symmetric around the unsmeared image. Therefore, we can estimate the ship centroids in subaperture images to a certain accuracy even though smears may

exist.

Using the estimated ship velocity, the phase error is compensated in the phase-history domain for the high-resolution image. The restored high-resolution image is formed from the compensated phase-history data. Since the estimated ship velocity from the Kalman filter may not be perfectly correct, we may not restore the smeared image perfectly. Because variances of the ship velocity estimates can be obtained from the Kalman filter, we will be able to assess how well we can restore the smeared high resolution image.

4.4 The Radar Imagery Generator (RIG)

The Radar Imagery Generator (RIG) is a simulation tool for creating SAR imagery [32]. The target model database used for RIG is that of [28]. Given the specifications of the geometric model between the radar and the target, the target motion parameters and the radar parameters, SAR intensity images of target scenes can be simulated by RIG. However, the RIG images are not similar to real SAR images. RIG does not consider the random phase in the scene reflectivity, thus RIG images do not have any speckle. As a result, we can consider the RIG images as providing the mean intensity of the speckled SAR images.

We can simulate the speckled SAR intensity images from the RIG images, if we consider the RIG images as mean intensity images. The pixel intensity in the speckled SAR image is a realization of a random variable that is exponentially distributed by that pixel's mean intensity. One way to obtain a realization of such an exponential random variable is to find out the corresponding complex Gaussian random variable. In Section 2.7, the variance of the real and imaginary part of the complex Gaussian random variable σ^2 can be expressed by the pixel mean intensity I_0:

$$\sigma^2 = I_0/2. \tag{4.1}$$

Since the real and imaginary parts of the complex Gaussian random variable are zero-mean, we can generate a realization of the complex image. The squared magnitude of the complex image will be used as our simulated speckled SAR intensity image.

4.5 Centroid Estimation

Consider a target consisting of N pixels. Each pixel is denoted by a single index i, $i = 1, \ldots, N$. If each point has an intensity I_i, then the target centroid is defined as

$$x_{nc} = \frac{\sum_i x_{ni} I_i}{\sum_i I_i}, \tag{4.2}$$

where x_{ni} is the nth coordinate of point i.

If the pixel intensities are random variables, the target centroid measurement in (4.2) will also be random. The expressions for the variance of the centroid measurement are given in [4] and [27]. However, in [4], the pixel intensity I_i is assumed to be Gaussian. In [27], to avoid use of the correlation coefficient between the denominator and numerator in (4.2), the authors use the coordinate system origin as the target true centroid which is not generally known. In addition, the effect of image quantization is not considered in [27]. In this section, the general expression for the centroid measurement variance will be given.

Suppose that I_i are independent random variables with mean μ_i and standard deviation σ_i. In order to calculate the expectation and variance of x_{nc}, we consider x_{nc} as the ratio $\frac{M_n}{S}$ where both M_n and S are random variables. The expectation and variance of x_{nc} can be approximated as [29]:

$$E(x_{nc}) = \frac{\eta_{M_n}}{\eta_S} - \frac{r\sigma_{M_n}\sigma_S}{\eta_S^2} + \frac{\eta_{M_n}}{\eta_S^3}\sigma_S^2, \tag{4.3}$$

$$VAR(x_{nc}) = \frac{\sigma_{M_n}^2}{\eta_S^2} - \frac{2\eta_{M_n}}{\eta_S^3} r\sigma_{M_n}\sigma_S + \frac{\eta_{M_n}^2}{\eta_S^4}\sigma_S^2, \tag{4.4}$$

where

$$M_n = \sum_i x_{ni} I_i \tag{4.5}$$

$$S = \sum_i I_i \tag{4.6}$$

$$\eta_{M_n} = E(M_n) \tag{4.7}$$

$$\eta_S = E(S) \tag{4.8}$$

$$\sigma_{M_n}^2 = VAR(M_n) \tag{4.9}$$

$$\sigma_S^2 = VAR(S), \tag{4.10}$$

$$r\sigma_{M_n}\sigma_S = E[(M_n - \eta_{M_n})(S - \eta_S)] \tag{4.11}$$

and r is the correlation coefficient between M_n and S.

The centroid measurement in (4.2) does not consider the effect of image quantization. To include this effect, an extra random variable due to the image resolution must be added to (4.2). The error due to the quantized image resolution can be characterized by a random variable which is uniformly distributed within the image resolution size. Consequently, the target centroid measurement is expressed as

$$x'_{nc} = x_{nc} + \xi. \tag{4.12}$$

The random variable ξ is uniformly distributed within $[-\Delta x_n/2, \Delta x_n/2]$, where Δx_n denotes the image resolution of the nth coordinate. It is easy to show that $E(\xi) = 0$ and $VAR(\xi) = (\Delta x_n)^2/12$. As a result, the variance of the centroid measurement is:

$$VAR(x'_{nc}) = VAR(x_{nc}) + (\Delta x_n)^2/12. \tag{4.13}$$

4.6 Ship Centroid Estimation without Smear Effect

The ship pixel intensity I_i in an unsmeared SAR image can be modelled as an independent random variable with exponential distribution. The parameter of the exponential distribution is the mean intensity of the pixel, where we assume the RIG images provide the mean intensity.

Since I_i is independent of I_j if $i \neq j$, Equations (4.7) to (4.10) can be rewritten as:

$$\eta_{M_n} = E(\sum_i x_{ni} I_i) = \sum_i x_{ni} E(I_i) \tag{4.14}$$

$$\eta_S = E(\sum_i I_i) = \sum_i E(I_i) \tag{4.15}$$

$$\sigma^2_{M_n} = VAR(\sum_i x^2_{ni} I_i) = \sum_i x^2_{ni} VAR(I_i) \tag{4.16}$$

$$\sigma^2_S = VAR(\sum_i I_i) = \sum_i VAR(I_i) \tag{4.17}$$

$$r\sigma_{M_n}\sigma_S = E\{[\sum_i x_{ni}(I_i - E[I_i])][\sum_j (I_j - E[I_j])]\} \quad (4.18)$$

$$= \sum_i x_{ni} VAR(I_i) \quad (4.19)$$

To derive (4.19) from (4.18), the following relationship is used:

$$E\{[I_i - E(I_i)][I_j - E(I_j)]\} = \begin{cases} VAR(I_i) & i = j \\ 0 & i \neq j \end{cases} \quad (4.20)$$

This is due to the independence between I_i and I_j when $i \neq j$.

Substituting Equations (4.14) to (4.19) into (4.4) and (4.13), we obtain the variance of the centroid estimation for an unsmeared ship.

4.7 Pixel Intensity Model for Smeared SAR Images

If the smear due to the ship motion cannot be ignored in SAR images, we cannot model the image pixel intensity as independent random variables. The smeared image can be modelled as the discrete convolution (circular convolution) of the unsmeared image and the impulse response due to ship motion. Without loss of generality, we consider the unsmeared SAR image and the impulse response as 1-D data sequences with the same length N. Therefore the resultant smeared image will be a 1-D data sequence with length N. We denote the unsmeared complex image as $\{v_i\}_{i=0}^{N-1}$, while the corresponding unsmeared intensity image as $\{I'_i\}_{i=0}^{N-1}$ with mean intensity $\{I'_{i0}\}_{i=0}^{N-1}$. The complex-valued impulse response is denoted as $\{h_i\}_{i=0}^{N-1}$, and the smeared intensity image is $\{I_i\}_{i=0}^{N-1}$. The pixel intensity I_i in the smeared image can be expressed as

$$I_i = \mid \sum_{m=0}^{N-1} v_{(m)_N} h_{(i-m)_N} \mid^2, \quad 0 \leq i \leq N-1. \quad (4.21)$$

The notation $(n)_N$ is used to denote n modulo N. To have more insight to (4.21), we rewrite (4.21) into a simple way:

$$I_i = \mid \sum_{m=0}^{N-1} v_m h_m \mid^2 . \quad (4.22)$$

Since v_m and h_m are complex numbers, $\sum_{m=0}^{N-1} v_m h_m$ is complex. With $*$ denoting complex conjugate, (4.22) can be expanded as:

$$\begin{aligned} I_i &= (\sum_{m=0}^{N-1} v_m h_m)(\sum_{m=0}^{N-1} v_m h_m)^* \\ &= (h_1 v_1 + h_2 v_2 + \cdots + h_{N-1} v_{N-1})(h_1^* v_1^* + h_2^* v_2^* + \cdots + h_{N-1}^* v_{N-1}^*) \\ &= \mid h_1 \mid^2 \mid v_1 \mid^2 + \cdots + \mid h_{N-1} \mid^2 \mid v_{N-1} \mid^2 + \sum_{k<j} (h_k h_j^* v_k v_j^* + h_k^* h_j v_k^* v_j) \\ &= \mid h_1 \mid^2 \mid v_1 \mid^2 + \cdots + \mid h_{N-1} \mid^2 \mid v_{N-1} \mid^2 + \sum_{k<j} 2Re[h_k h_j^* v_k v_j^*] \\ &= \mid h_1 \mid^2 I_1' + \cdots + \mid h_{N-1} \mid^2 I_{N-1}' + \sum_{k<j} 2Re[h_k h_j^* v_k v_j^*] \end{aligned} \tag{4.23}$$

where $Re[\cdot]$ denotes the real part of a complex number.

From (4.23), we can see that the pixel intensity in the smeared image is the weighted summation of the unsmeared image pixel intensity, where the weight is related to the impulse response. Thus, correlations exist between the pixel intensities in the smeared image, even though the unsmeared image intensities are modelled as independent random variables. The smeared image intensities should therefore be modelled as correlated random variables.

4.8 Ship Centroid Estimation with Smear Effect

Since the smeared image pixel intensities cannot be modelled as independent random variables, we cannot use the equations in Section 4.6 to evaluate the centroid estimation variance for a smeared image. In this section and Appendix C, the target centroid estimation variance for a smeared image will be given. To our knowledge, the following expressions do not appear in the literature.

With the pixel intensity model in (4.23), the variance of centroid estimation in smeared images can be obtained by substituting (4.23) into the equations in Section 4.5. Recalling that the pixel intensities are not independent random variables in smeared images, Equations (4.7) to (4.10) are rewritten as:

$$\eta_{M_n} = E(\sum_i x_{ni} I_i) = \sum_i x_{ni} E(I_i) \tag{4.24}$$

$$\eta_S = E(\sum_i I_i) = \sum_i E(I_i) \tag{4.25}$$

$$\begin{aligned}
\sigma^2_{M_n} &= VAR(\sum_i x_{ni} I_i) \\
&= E\{[\sum_i x_{ni}(I_i - E(I_i))]^2\} \\
&= \sum_i x^2_{ni} VAR(I_i) + \sum_{i<j} 2x_{ni}x_{nj} E[(I_i - E(I_i))(I_j - E(I_j))] \qquad (4.26)
\end{aligned}$$

$$\begin{aligned}
\sigma^2_S &= VAR(\sum_i I_i) \\
&= E\{[\sum_i (I_i - E(I_i))]^2\} \\
&= \sum_i VAR(I_i) + \sum_{i<j} 2E[(I_i - E(I_i))(I_j - E(I_j))] \qquad (4.27)
\end{aligned}$$

$$\begin{aligned}
r\sigma_{M_n}\sigma_S &= E[(M_n - \eta_{M_n})(S - \eta_S)] \\
&= E\{[\sum_i x_{ni}(I_i - E[I_i])][\sum_i (I_i - E[I_i])]\} \\
&= \sum_i x_{ni} VAR(I_i) + \sum_{i<j} (x_{ni} + x_{nj}) E[(I_i - E(I_i))(I_j - E(I_j))] \qquad (4.28)
\end{aligned}$$

Equations (4.24) to (4.28) are easy to evaluate numerically if $E(I_i)$, $VAR(I_i)$ and $E[(I_i - E(I_i))(I_j - E(I_j))]$ are known. Expressions for $E(I_i)$, $VAR(I_i)$ and $E[(I_i - E(I_i))(I_j - E(I_j))]$ are quite lengthy to derive and are given in Appendix C. It is interesting to note that the centroid estimation variance for an unsmeared ship in Section 4.6 is a special case of the variance for a smeared ship given in this section. If we consider the impulse response sequence $\{h_i\}_{i=0}^{N-1}$ as a unit-sample sequence, Equations (4.24) to (4.28) will be the same as (4.14) to (4.19).

The computational complexity of the centroid estimation variance for a smeared image is proportional to N^4, where N is the number of pixels in the image.

4.9 Experimental Results for Ship Centroid Estimation

In this section, results are provided for subaperture time images that are smeared due to ship motion. To be precise, the impulse responses due to ship motion are different for different subapertures, since the radar imaging geometries are different. When a long synthetic aperture is divided into a set of subapertures, only one of the

subapertures may be of broadside geometry (see Section 3.2), while the others are *non-broadside*. In non-broadside (also referred as *squinted*) imaging geometry, the center pulse is not launched perpendicular to the radar flight path. Compared to the images from broadside geometry, image rotations exist in images from non-broadside geometry [17]. The rotation angle is the same as the squint angle from the broadside case. However, in our case, the angle diversity for the long synthetic aperture is small ($\Delta\theta = 0.032\text{rad} = 1.83$ degrees for the parameters in Section 3.4). Thus, image rotations in the subaperture images are small enough to be ignored, and the impulse responses for different subapertures can be considered to be the same as that of the broadside case. The impulse response due to target motion for the broadside case is given in Section 3.2.

Using the SAR parameters given in Section 3.4, two sets of simulations were conducted for ship centroid estimation. Integration times for subaperture were chosen to be 0.3sec and 1.5sec, respectively, for the two sets. In each set, different ship headings (0, 45 and 90 degrees) were considered. The ship heading angle is the angle moving clockwise from north. A heading of 0 degrees means only cross-range velocity exists if the ship is moving, a 45 degree heading means that both range and cross-range velocity exist, and a 90 degree heading consists purely of range velocity. For each ship heading, different ship velocities were considered. The case of ship velocity $v = 0$ is equivalent to the unsmeared image case, while $v \neq 0$ case is smeared image case. The results for ship centroid estimation variance are given in Tables 4.1 to 4.6. The results in these tables are only the $VAR(x_{nc})$ part in (4.13), and the variances due to the image resolution have to be added to get the total centroid estimation variances. For 0.3sec integration time, results from Monte-Carlo runs (300 runs) are compared with the analytical results. However, as explained in the next paragraph, for 1.5sec integration time, only results from Monte-Carlo runs (300 runs) are given for the smeared image case, while results from both Monte-Carlo runs and analysis are given for the unsmeared image case. Analytical calculations for unsmeared and smeared images used equations in Section 4.6 and 4.8, respectively. Selected ship images and impulse responses for each case are shown in Figures 4.1 to 4.6. In our simulations, the image shift in cross-range dimension due to ship slant range velocity

has been removed, since this shift does not affect centroid estimation variance.

The analytically derived centroid estimation variance for smeared images of 1.5sec integration time was not conducted due to the excessively long CPU time required for the calculations. As mentioned in Section 4.8, the computational complexity of the calculation for a smeared image is proportional to N^4, where N is the number of image pixels. Due to the finer cross-range resolution for 1.5sec integration time, the number of ship pixels in a 1.5sec integration time image is larger than that in a 0.3sec integration time image. For example, as shown in Figure 4.1 and Figure 4.4, the ship size in the image for the case of 0.3sec integration time with 0 degrees heading, is about 10×27 pixels. In the corresponding image for 1.5sec integration time, the ship size is about 30×27 pixels, which is three times as large as that of the 0.3sec case. To find the analytical centroid estimation variance for the smeared image of 0.3sec integration time and 0 degrees ship heading, requires about 1 hour CPU time on an Ultrasparc 1 work station. Thus, about $3^4 = 81$ CPU hours are needed for the analytical calculation for the smeared image of 1.5sec integration time.

The range resolution of SAR images is related only to the bandwidth of the radar transmitted FM chirp (recall Section 2.5.3), thus with the parameters in Section 3.4, the range resolution is 0.5m for both integration times. As a result, the variance due to the image range resolution is $0.02m^2$. However, the cross-range resolution is dependent on the integration time. The cross-range resolution is 26.5m for 0.3sec integration time, and 5.26m for 1.5sec integration time. The variance due to the image cross-range resolution is $58.5m^2$ for 0.3sec integration time, and $2.30m^2$ for 1.5sec integration time.

The ship velocity in the tables and figures in this section refers to ship ground velocity. However, ship velocity in the slant plane is needed for the simulations. The slant plane velocity is the ground velocity projected onto the slant plane. If the ground velocity is denoted as v, the ship heading angle is φ, and the radar grazing angle is ψ as shown in Figure 2.6, then the slant range velocity is $v_r = v \sin\varphi \cos\psi$, and the cross-range velocity is $v_c = v \cos\varphi$.

The same ship model is used in Figures 4.1 to 4.6. However, due to the finer cross-range resolution for 1.5sec integration time, the ship for 1.5sec has more pixels

in cross-range direction than the ship for 0.3sec. Since the range resolutions are the same for both 0.3sec and 1.5sec integration time, the images have the same number of pixels in the range direction.

As expected, the analytical results for both the unsmeared and smeared images in Tables 4.1 to 4.6 are close to the Monte-Carlo results. In addition, the variances from Monte-Carlo runs are somewhat larger than the analytical results, which is as expected.

Comparing the results for the 0.3sec and 1.5sec integration times, we observe that the centroid estimation variance for 1.5sec is lower than that for 0.3sec. The variance decrease in the cross-range for 1.5sec integration time is due to the finer cross-range resolution. The decrease in the range direction is because in 1.5sec integration time images, there are more pixels in the same range line, which gives us more information about where the range centroid is. As a result, lower centroid estimation variances are obtained for 1.5sec integration time.

Comparing the centroid estimation variance in Tables 4.1 to 4.3 for 0.3sec integration time, we can see that the variance in the range direction increases, while the variance in the cross-range decreases when the ship heading changes from 0 degrees to 90 degrees. The reason for this is that, generally speaking, with the same image resolution, the larger the target size is, the more uncertainty in the centroid estimation, which leads to a higher centroid estimation variance. In Figures 4.1 to 4.3, we can see that when the ship heading turns from 0 degrees to 90 degrees, the pixel number increases in the range direction, and decreases in the cross-range direction. That is to say, the ship size is getting larger in range and getting smaller in cross-range. Thus, the centroid estimation variance increases in range and decreases in cross-range. The same thing happens to the results for 1.5sec integration time in Tables 4.4 to 4.6.

It can be observed that, the smear effect increases the centroid estimation variance, with respect to both Monte-Carlo and analytical results in Tables 4.1 to 4.6. This observation is more obvious for cross-range variance. However, the range variances do not always increase with increasing ship velocity. This phenomenon can be explained as follows: we believe that on one hand, the smear due to the ship motion will enlarge the ship size which leads to an increase of the centroid estimation variance. On the

other hand, the smear may have some smoothing effect on the speckle, which leads to a decrease of the centroid estimation variance. These two effects offset each other. For the short integration time in subaperture images, the cross-range resolution is low, and the variance increase from the smeared ship size is a dominant effect. Thus the cross-range centroid estimation variance increases with increasing ship velocity. In the range dimension, since the range resolution is high, the variance decrease due to the smoothing effect on the speckle cannot be ignored compared to the variance increase from the smeared ship size. Thus the range centroid estimation variance may not always increase with increasing ship velocity. Observing the results in the tables, we can see that the range variance decreases from $v = 0$ to $v = 4m/sec$, and increases from $v = 4m/sec$ to $v = 8m/sec$. The range variance for $v = 8m/sec$ is higher than that for $v = 0$, which implies that eventually the smear effect enlarges the range centroid estimation variance.

For the ship heading of 0 degrees, in Table 4.1 and Table 4.4, the range centroid estimation variance does not change much since there is no slant range velocity and thus little smear in range dimension. However, for the ship heading of 90 degrees, the slant range velocity causes smear in cross-range dimension which leads to an increase in the cross-range centroid estimation variance.

The cross-range centroid estimation variance is extremely small for the unsmeared image with 0.3sec integration time and 90 degrees ship heading. As we can see from Figure 4.3, in this case, the ship image becomes a line due to the low cross-range resolution, and the ship image only occupies one pixel in the cross-range dimension. As a result, the cross-range variance is extremely small. However, it will not be so small if we add the variance due to the image resolution.

We can observe that for the same ship velocity increase, the cross-range centroid estimation variances for the 0.3sec case increase faster than for the 1.5sec case. This is because the cross-range resolution is much coarser in the 0.3sec case than in the 1.5sec case.

As a whole, the conclusions from the experimental results are:

- For the ship centroid estimation variance in smeared and unsmeared images, the analytical results from Section 4.6 and 4.8 are close to the results from

Monte-Carlo runs.

- With the same ship velocity and ship heading, the centroid estimation variances are smaller for 1.5sec integration time than for 0.3sec integration time, due to the higher resolution in 1.5sec case.

- With the same subaperture integration time and ship heading, the centroid estimation variance increases when the ship velocity increases.

- With the same image resolution, the centroid estimation variance is larger for a larger size ship.

- With the same ship velocity increase, the increase in the centroid estimation variance is larger for 0.3sec subaperture integration time than for 1.5sec case. The reason for this is that 1.5sec integration time images have higher resolution.

Ship Speed(m/sec)	Range(m^2)		Cross-range(m^2)	
	Monte-Carlo	Eq. (4.4)	Monte-Carlo	Eq. (4.4)
$v = 0$	0.0860	0.0803	13.1175	12.8541
$v = 2$	0.0832	0.0803	13.0122	12.8550
$v = 4$	0.0849	0.0803	13.5699	12.8589
$v = 6$	0.0857	0.0803	14.0341	12.8646
$v = 8$	0.0838	0.0803	14.6126	12.8735
$v = 10$	0.0873	0.0803	14.7600	12.8849

Table 4.1: Centroid estimation variance for subaperture integration time 0.3sec and ship heading 0 degrees ($VAR(x_{nc})$ in Eq. (4.13))

4.10 Summary

In this chapter, the first step in our proposed method, ship centroid estimation is examined. Both analysis and simulation results of ship centroid estimation variance for unsmeared and smeared images are given. The analysis is verified by the simulation results from Monte-Carlo runs. The most important conclusions on the ship centroid estimation variance we have quantified from this chapter are:

- With the same ship velocity, the centroid estimation variance is smaller for suitably long subaperture integration times.
- With the same subaperture integration time, the centroid estimation variances increase with increasing ship velocity.

Ship Speed(m/sec)	Range(m^2)		Cross-range(m^2)	
	Monte-Carlo	Eq. (4.4)	Monte-Carlo	Eq. (4.4)
$v = 0$	1.1313	1.0734	3.8428	3.8310
$v = 4$	1.0500	1.0224	5.5668	4.8980
$v = 8$	1.1597	1.0740	8.3242	8.0156

Table 4.2: Centroid estimation variance for subaperture integration time 0.3sec and ship heading 45 degrees ($VAR(x_{nc})$ in Eq. (4.13))

Ship Speed(m/sec)	Range(m^2)		Cross-range(m^2)	
	Monte-Carlo	Eq. (4.4)	Monte-Carlo	Eq. (4.4)
$v = 0$	2.1748	2.0366	3.62e-8	2.91e-11
$v = 4$	2.0835	1.9200	5.5973	4.8840
$v = 8$	2.3991	2.2799	14.2874	12.3754

Table 4.3: Centroid estimation variance for subaperture integration time 0.3sec and ship heading 90 degrees ($VAR(x_{nc})$ in Eq. (4.13))

Ship Speed(m/sec)	Range(m^2)	Cross-range(m^2)
	Monte-Carlo	Monte-Carlo
$v = 0$	0.0204	2.4685
$v = 4$	0.0205	2.6831
$v = 8$	0.0200	2.9136

Table 4.4: Centroid estimation variance for subaperture integration time 1.5sec and ship heading 0 degrees ($VAR(x_{nc})$ in Eq. (4.13)). The analytical centroid estimation variance (Eq. (4.4)) in range and cross-range dimension at $v = 0$ is $0.0200m^2$ and $2.3248m^2$ respectively.

Ship Speed(m/sec)	Range(m^2)	Cross-range(m^2)
	Monte-Carlo	Monte-Carlo
$v = 0$	0.4350	1.1467
$v = 4$	0.3775	1.5588
$v = 8$	0.5055	2.7804

Table 4.5: Centroid estimation variance for subaperture integration time 1.5sec and ship heading 45 degrees ($VAR(x_{nc})$ in Eq. (4.13)). The analytical centroid estimation variance (Eq. (4.4)) in range and cross-range dimension at $v = 0$ is $0.3901m^2$ and $1.0370m^2$ respectively.

Ship Speed(m/sec)	Range(m^2)	Cross-range(m^2)
	Monte-Carlo	Monte-Carlo
$v = 0$	0.6250	0.0889
$v = 4$	0.5137	1.0302
$v = 8$	0.7570	3.2884

Table 4.6: Centroid estimation variance for subaperture integration time 1.5sec and ship heading 90 degrees ($VAR(x_{nc})$ in Eq. (4.13)). The analytical centroid estimation variance (Eq. (4.4)) in range and cross-range dimension at $v = 0$ is $0.5954m^2$ and $0.0809m^2$ respectively.

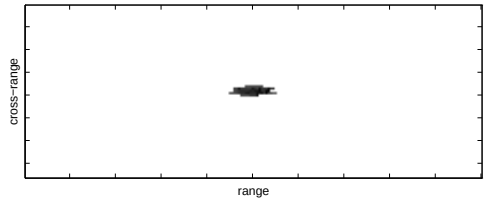

RIG image (76×200 pixels)

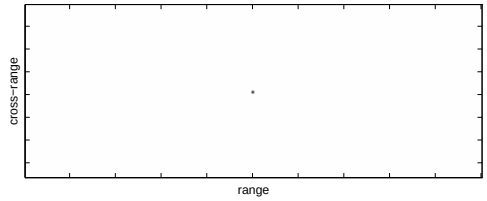

Impulse response with ship speed 4m/sec (76×200 pixels)

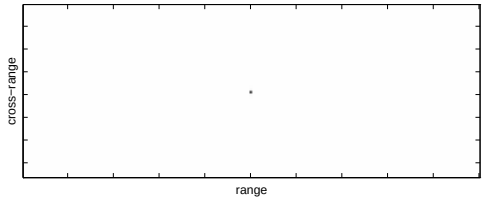

Impulse response with ship speed 8m/sec (76×200 pixels)

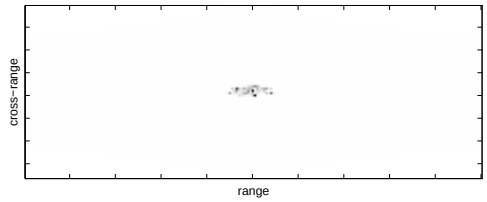

Smeared ship with ship speed 4m/sec (76×200 pixels)

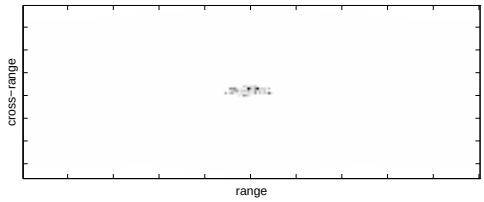

Smeared ship with ship speed 8m/sec (76×200 pixels)

Figure 4.1: Images of ship with heading of 0 degrees and integration time 0.3sec

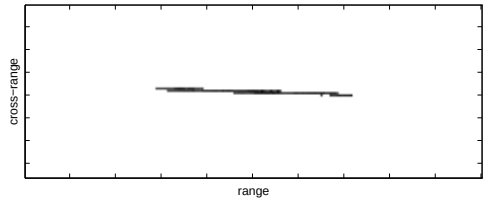

RIG image (76×200 pixels)

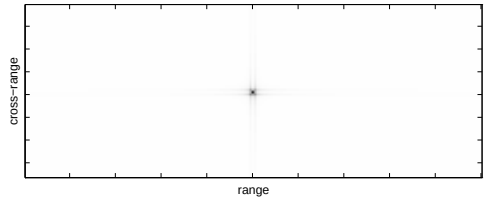

Impulse response with ship speed 4m/sec (76×200 pixels)

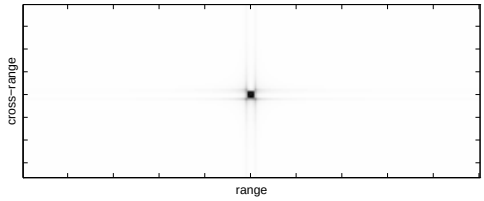

Impulse response with ship speed 8m/sec (76×200 pixels)

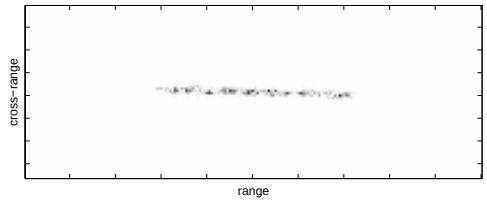

Smeared ship with ship speed 4m/sec (76×200 pixels)

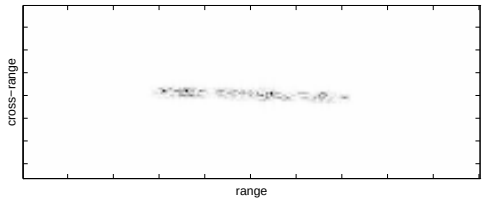

Smeared ship with ship speed 8m/sec (76×200 pixels)

Figure 4.2: Images of ship with heading of 45 degrees and integration time 0.3sec

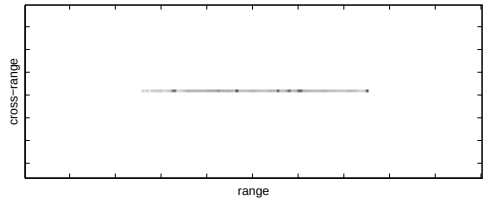

RIG image (76×200 pixels)

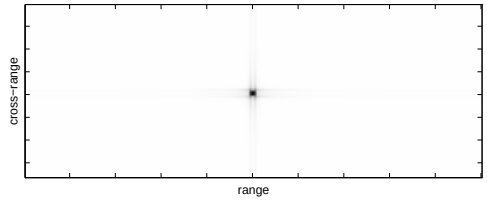

Impulse response with ship speed 4m/sec (76×200 pixels)

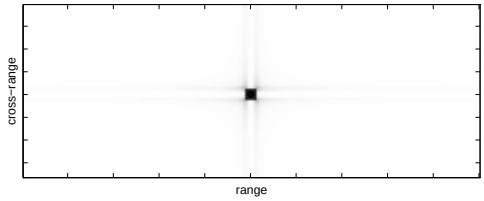

Impulse response with ship speed 8m/sec (76×200 pixels)

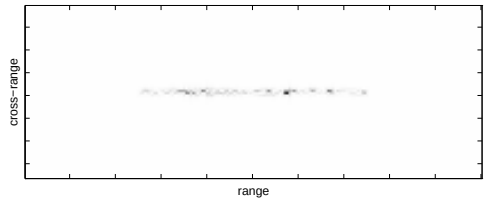

Smeared ship with ship speed 4m/sec (76×200 pixels)

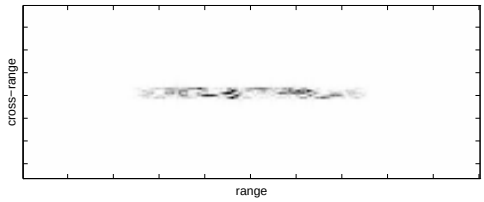

Smeared ship with ship speed 8m/sec (76×200 pixels)

Figure 4.3: Images of ship with heading of 90 degrees and integration time 0.3sec

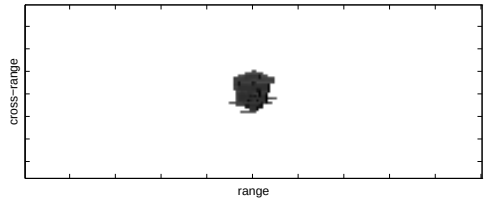

RIG image (76×200 pixels)

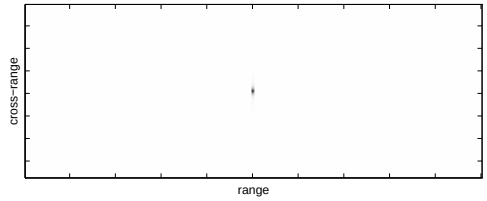

Impulse response with ship speed 4m/sec (76×200 pixels)

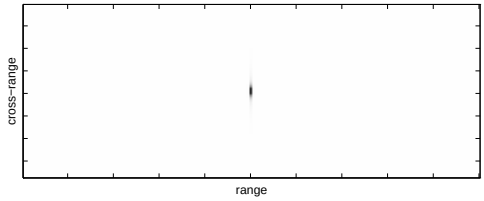

Impulse response with ship speed 8m/sec (76×200 pixels)

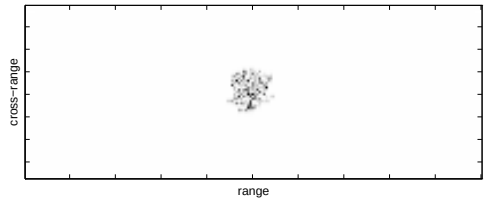

Smeared ship with ship speed 4m/sec (76×200 pixels)

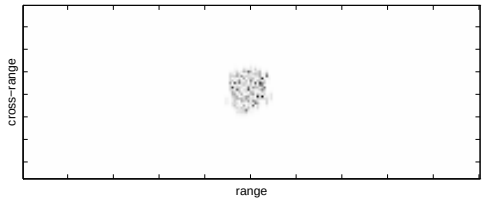

Smeared ship with ship speed 8m/sec (76×200 pixels)

Figure 4.4: Images of ship with heading of 0 degrees and integration time 1.5sec

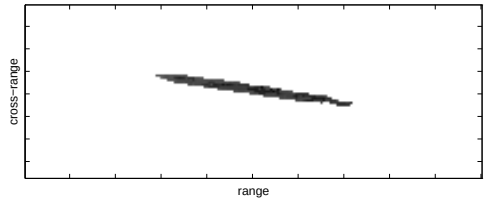

RIG image (76×200 pixels)

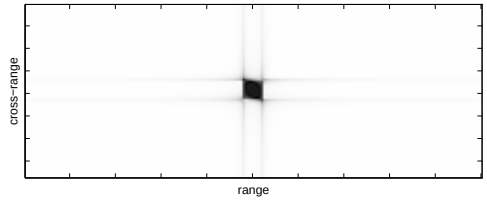

Impulse response with ship speed 4m/sec (76×200 pixels)

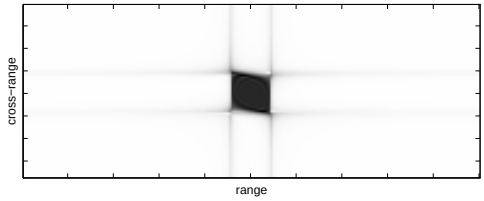

Impulse response with ship speed 8m/sec (76×200 pixels)

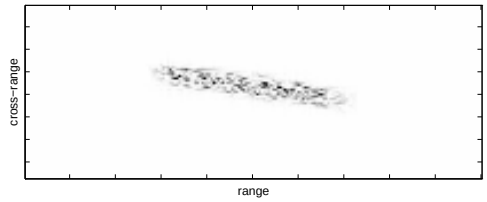

Smeared ship with ship speed 4m/sec (76×200 pixels)

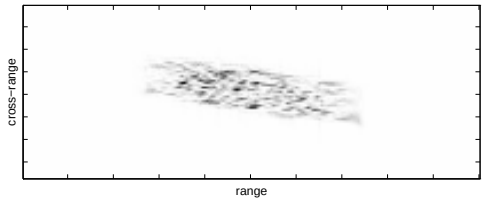

Smeared ship with ship speed 8m/sec (76×200 pixels)

Figure 4.5: Images of ship with heading of 45 degrees and integration time 1.5sec

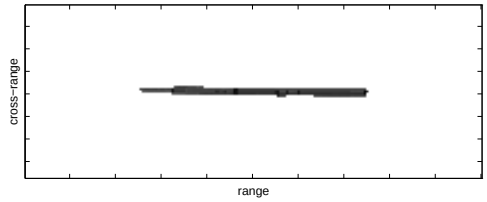

RIG image (76×200 pixels)

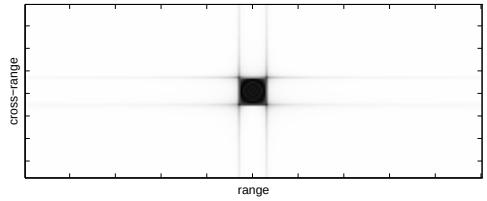

Impulse response with ship speed 4m/sec (76×200 pixels)

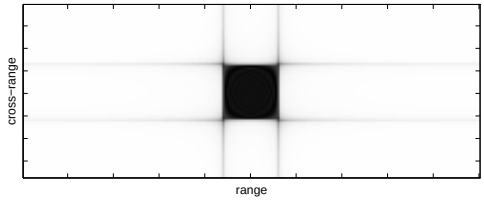

Impulse response with ship speed 8m/sec (76×200 pixels)

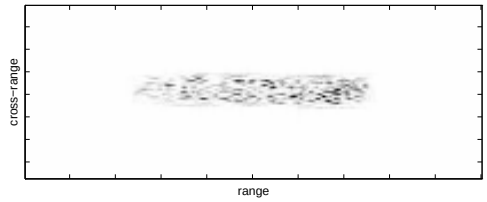

Smeared ship with ship speed 4m/sec (76×200 pixels)

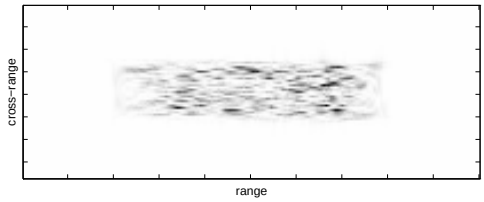

Smeared ship with ship speed 8m/sec (76×200 pixels)

Figure 4.6: Images of ship with heading of 90 degrees and integration time 1.5sec

Chapter 5

Ship Velocity Estimation

5.1 Introduction

In this chapter, the second and third step in our proposed method, ship velocity estimation and SAR image restoration, will be examined. A set of ship centroid estimates can be obtained from the subaperture image sequence. In the following, we estimate the ship velocity from these centroid estimates recursively using a Kalman filter. A general overview of Kalman filter theory is given first. Then the Kalman filter model for ship velocity estimation is set up. Since the measurement noise covariance matrix in our Kalman filter does not match the true measurement noise, it is interesting to see whether we can still estimate the ship velocity well by the Kalman filter. Finally, SAR image restoration using the estimated ship velocity will be investigated.

5.2 Discrete Linear Kalman Filter

Kalman filtering is an optimal state estimation process applied to a dynamic system that involves random perturbations. Quoting Chui[7], "the Kalman filter gives a linear, unbiased, and minimum error variance recursive algorithm to optimally estimate the unknown state of a dynamic system from noisy data taken at discrete real-time intervals". A general overview of the discrete linear Kalman filter is necessary background for this chapter. The detailed treatment of Kalman filter theory can be found

in [3] [5] [7] [30].

5.2.1 Kalman Filter Algorithm

Consider a linear stochastic system with state equation:

$$\underline{X}_{t+1} = \mathbf{F}_t \underline{X}_t + \mathbf{G}_t \underline{U}_t, \quad t = 0, \ldots, \tag{5.1}$$

and observation (measurement) equation:

$$\underline{Y}_t = \mathbf{H}_t \underline{X}_t + \underline{V}_t, \quad t = 0, \ldots. \tag{5.2}$$

$\underline{X}_t$ represents the *state* of the system at time t, and $\underline{U}_t$ represents the *process noise* or input disturbance to the system at time t. $\underline{Y}_t$ is the *output* of the system at time t, while $\underline{V}_t$ is the observation (measurement) noise at time t.

The problem we want to solve is: we have an observation sequence from the stochastic system $\underline{Y}_0, \ldots, \underline{Y}_t$, and we wish to estimate the state of the system $\underline{X}_t$ from the observation sequence. The Kalman filter gives us a solution of how to determine the optimal estimate $\hat{\underline{X}}_t$ of $\underline{X}_t$. The optimality criterion used in the Kalman filter is the minimum-mean-norm-squared-error (MMSE), which can be expressed as

$$\hat{\underline{X}}_t = \mathbf{E}_{\min}\{|| \hat{\underline{X}}_t - \underline{X}_t ||^2\}. \tag{5.3}$$

It can be shown that the optimum estimate $\hat{\underline{X}}_t$ is:

$$\hat{\underline{X}}_t = \mathbf{E}\{\underline{X}_t \mid \underline{Y}_0, \ldots, \underline{Y}_t\}. \tag{5.4}$$

In the Kalman filter, it is assumed that the input sequence $\{\underline{U}_t\}_{t=0}^{\infty}$ and the observation noise $\{\underline{V}_t\}_{t=0}^{\infty}$ are independent sequences of independent zero-mean Gaussian random vectors. It is also assumed that the initial condition $\underline{X}_0$ is a Gaussian random vector independent of $\{\underline{U}_t\}_{t=0}^{\infty}$ and $\{\underline{V}_t\}_{t=0}^{\infty}$.

With $\underline{Y}_0^t$ denoting the sequence $\underline{Y}_0, \ldots, \underline{Y}_t$, the estimates of $\underline{X}_t$ and $\underline{X}_{t+1}$ given observations $\underline{Y}_0^t$ can be expressed respectively as $\hat{\underline{X}}_{t|t} \triangleq E\{\underline{X}_t \mid \underline{Y}_0^t\}$ and $\hat{\underline{X}}_{t+1|t} \triangleq E\{\underline{X}_{t+1} \mid \underline{Y}_0^t\}$. With the above assumptions, $\hat{\underline{X}}_{t|t-1}$ and $\hat{\underline{X}}_{t|t}$ are given recursively by the following equations:

$$\hat{\underline{X}}_{t|t-1} = \mathbf{F}_{t-1} \hat{\underline{X}}_{t-1|t-1} \quad t = 1, \ldots \tag{5.5}$$

and

$$\underline{\hat{X}}_{t|t} = \underline{\hat{X}}_{t|t-1} + \mathbf{K}_t(\underline{Y}_t - \mathbf{H}_t\underline{\hat{X}}_{t|t-1}) \quad t = 1, \ldots \tag{5.6}$$

with the initialization $\underline{\hat{X}}_{0|0} \stackrel{\triangle}{=} \mathbf{E}\{\underline{X}_0\}$. The matrix $\mathbf{K}_t$, called the *Kalman gain matrix*, is given by

$$\mathbf{K}_t = \mathbf{\Sigma}_{t|t-1}\mathbf{H}_t^T(\mathbf{H}_t\mathbf{\Sigma}_{t|t-1}\mathbf{H}_t^T + \mathbf{R}_t)^{-1}, \tag{5.7}$$

where $\mathbf{\Sigma}_{t|t-1} \stackrel{\triangle}{=} COV(\underline{X}_t \mid \underline{Y}_0^{t-1})$ is the covariance matrix of the prediction error $\underline{X}_t - \underline{\hat{X}}_{t|t-1}$, conditioned on $\underline{Y}_0^{t-1}$. $\mathbf{R}_t \stackrel{\triangle}{=} COV(\underline{V}_t)$ is the covariance matrix of the t^{th} measurement noise. The role of the Kalman gain can be easily seen from (5.6). If the Kalman gain is too small, the contribution of the current measurement will be ignored, and we trust the previous estimate $\underline{\hat{X}}_{t|t-1}$ much more than we trust the observation. If the Kalman filter gain is too large, the filter will weigh the current measurement more.

If we use $\mathbf{\Sigma}_{t|t}$ denoting the covariance matrix of the filtering error $\underline{X}_t - \underline{\hat{X}}_{t|t}$ conditioned on $\underline{Y}_0^t$, $\mathbf{\Sigma}_{t|t-1}$ can be computed jointly with $\mathbf{\Sigma}_{t|t}$ from the following recursion:

$$\mathbf{\Sigma}_{t|t-1} = \mathbf{F}_{t-1}\mathbf{\Sigma}_{t-1|t-1}\mathbf{F}_{t-1}^T + \mathbf{G}_{t-1}\mathbf{Q}_{t-1}\mathbf{G}_{t-1}^T \quad t = 1, \ldots \tag{5.8}$$

$$\mathbf{\Sigma}_{t|t} = \mathbf{\Sigma}_{t|t-1} - \mathbf{K}_t\mathbf{H}_t\mathbf{\Sigma}_{t|t-1} \quad t = 1, \ldots \tag{5.9}$$

with the initialization $\mathbf{\Sigma}_{0|0} \stackrel{\triangle}{=} COV(\underline{X}_0)$. Matrix $\mathbf{Q}_t \stackrel{\triangle}{=} COV(\underline{U}_t)$ is the covariance matrix of the tth process noise.

It can be shown that the *predicted measurement* is

$$\underline{\hat{Y}}_{t|t-1} = \mathbf{H}_t\underline{\hat{X}}_{t|t-1}, \tag{5.10}$$

and the covariance matrix of the measurement prediction error $\underline{Y}_t - \underline{\hat{Y}}_{t|t-1}$, conditioned on $\underline{Y}_0^{t-1}$ is

$$\mathbf{S}_t = \mathbf{H}_t\mathbf{\Sigma}_{t|t-1}\mathbf{H}_t^T + \mathbf{R}_t \quad t = 1, \ldots \tag{5.11}$$

The measurement prediction error $\underline{Y}_t - \underline{\hat{Y}}_{t|t-1}$ is also called the *innovation* sequence.

5.2.2 Steady-State Kalman Filter

Equations (5.9) and (5.8) can be combined into a single recursion, known as the discrete-time *Riccati equation*:

$$\mathbf{\Sigma}_{t+1|t} = \mathbf{F}_t \mathbf{\Sigma}_{t|t-1} \mathbf{F}_t^T - \mathbf{F}_t \mathbf{K}_t \mathbf{H}_t \mathbf{\Sigma}_{t|t-1} \mathbf{F}_t^T + \mathbf{G}_t \mathbf{Q}_t \mathbf{G}_t^T \quad t = 1, \ldots \tag{5.12}$$

As we can see, the covariance equations (5.9), (5.8) and (5.12) are independent of the measurements and can be iterated forward off-line (*i.e.* , without processing any measurements).

If the system is time-invariant ($\mathbf{F}$, $\mathbf{G}$ and $\mathbf{H}$ are constant) and the noises are stationary ($\mathbf{Q}$ and $\mathbf{R}$ are constant), then the solution to the Riccati equation will converge to a positive definite matrix $\bar{\Sigma}$ as $t \rightarrow \infty$ if the system is completely *controllable* and *observable*. The resulting constant covariance matrix $\bar{\Sigma}$ yields the *steady-state gain* for the Kalman filter, $\bar{\mathbf{K}} = \bar{\mathbf{\Sigma}} \mathbf{H}^T (\mathbf{H} \bar{\mathbf{\Sigma}} \mathbf{H}^T + \mathbf{R})^{-1}$. Once the steady state is reached, the Kalman filter is governed by the time-invariant version.

The observability and controllability of the system are the conditions for the existence of the steady-state solution. A useful interpretation of this condition is given in [3]. Observability guarantees the existence of the steady-state solution, and controllability causes the steady-state solution to be positive definite. The observability and controllability of the system can be verified as follows [5] [7]. A system with constant $\mathbf{F}$ and $\mathbf{H}$ is completely observable if and only if the following matrix $\mathbf{M}$ has rank n where n is the dimension of the state vector $\underline{X}_t$:

$$\mathbf{M} = \begin{bmatrix} \mathbf{H} \\ \mathbf{HF} \\ \vdots \\ \mathbf{HF}^{n-1} \end{bmatrix}. \tag{5.13}$$

A system with constant $\mathbf{F}$ and $\mathbf{G}$ is completely controllable if and only if the following matrix $\mathbf{W}$ has rank n, where n is the dimension of the state vector $\underline{X}_t$:

$$\mathbf{W} = \left[\mathbf{G}, \mathbf{FG}, \ldots, \mathbf{F}^{n-1} \mathbf{G} \right]. \tag{5.14}$$

5.2.3 Consistency of State Estimators

State estimator $\underline{\hat{X}}_{t|t}$ is called *consistent* if it is unbiased and its state estimation errors satisfy

$$\mathbf{E}\{[\underline{X}_t - \underline{\hat{X}}_{t|t}][\underline{X}_t - \underline{\hat{X}}_{t|t}]^T \mid \underline{Y}_0^t\} = \mathbf{\Sigma}_{t|t}. \tag{5.15}$$

That is to say, the estimation errors should be "consistent" with the filter-calculated covariance matrix. As we know, the system model consists of the dynamic state equation, the measurement equation, the initial state, and the statistical properties of the random noises. If all of these are completely accurate, then (5.15) holds exactly. In practice, however, all models contain some approximations, and (5.15) may not hold. For example, we get a sequence of observations from a system. To estimate the system state, we set up a system model. If our system model is exactly the same as the true system, then (5.15) will hold. However, if our system model does not match the true system, (5.15) will not hold. Therefore, (5.15) can be used to check whether the system model matches the true system.

The most common criteria for consistency of a filter are [3]:

1. The state errors should be zero-mean (unbiased) and their covariances are compatible with the filter-calculated covariance matrices.

2. The innovations should be zero-mean and their covariances are compatible with the filter-calculated covariance matrices.

Denoting the filtering error as $\underline{\tilde{X}}_t = \underline{X}_t - \underline{\hat{X}}_{t|t}$, we define the *normalized state estimation error* squared,

$$\epsilon_t = \underline{\tilde{X}}_t^t \mathbf{\Sigma}_{t|t}^{-1} \underline{\tilde{X}}_t. \tag{5.16}$$

If the filter is consistent (criterion 1), ϵ_t has a Chi-square distribution with n degrees of freedom, where n is the dimension of the state vector $\underline{X}_t$. This criterion can only be tested by simulation, where the true state is available.

Denoting the measurement prediction error as $\underline{\tilde{v}}_t = \underline{Y}_t - \underline{\hat{Y}}_{t|t-1}$, we define the *normalized innovations* squared,

$$\epsilon_t' = \underline{\tilde{v}}_t^t \mathbf{S}_t^{-1} \underline{\tilde{v}}_t. \tag{5.17}$$

If the filter is consistent (criterion 2), ϵ_t' has a Chi-square distribution with n' degrees of freedom, where n' is the dimension of the measurement vector $\underline{Y_t}$. The normalized state estimation error squared and normalized innovations squared have no units.

5.3 Kalman Filter for Ship Velocity Estimation

5.3.1 State Equation and Measurement Equation

As we know from Chapter 3, the ship slant range velocity causes a image shift in the cross-range direction. The amount of shift is $v_r R_0 / V_{radar}$, where R_0 is the distance between the radar and the patch center at aperture time $t' = 0$. If the amount of shift exceeds the size of radar footprint (patch size), the image may be reshifted by an integral number of patch sizes to satisfy the condition that the ship was in the radar footprint when it was illuminated by the radar. Therefore, in the cross-range dimension, the *actual ship position* is different from its *image position* if ship slant range velocity exists. To distinguish between actual ship position and its image position, we use two sets of coordinates. Coordinates (x'', y'') denote the actual ship position, which is the ship position in the slant patch. Coordinates (x', y') denote the ship image position. Axes x'' and x' denote cross-range direction, while y'' and y' denote range direction. In addition, we let the patch center be the origins of the two coordinates.

We denote the subaperture integration time as Δ, the ship slant range velocity as v_r, and the ship cross-range velocity as v_c. If we choose the the image position of the ship centroid and the ship velocity as the state variables, the state equation is set up as:

$$\begin{pmatrix} x'_{n+1} \\ y'_{n+1} \\ v_{c,n+1} \\ v_{r,n+1} \end{pmatrix} = \underbrace{\begin{pmatrix} 1 & 0 & \Delta & 0 \\ 0 & 1 & 0 & \Delta \\ 0 & 0 & 1 & 0 \\ 0 & 0 & 0 & 1 \end{pmatrix}}_{\mathbf{F}} \begin{pmatrix} x'_n \\ y'_n \\ v_{c,n} \\ v_{r,n} \end{pmatrix} + \underbrace{\begin{pmatrix} \frac{\Delta^2}{2} & -\frac{\Delta}{V_{radar}} R_0 \\ 0 & \frac{\Delta^2}{2} \\ \Delta & 0 \\ 0 & \Delta \end{pmatrix}}_{\mathbf{G}} \begin{pmatrix} u_x \\ u_y \end{pmatrix} \tag{5.18}$$

Since the maneuver strategies of the ship are unknown to us, one way to model the ship motion is to assume that the ship undergoes random accelerations. We use u_x

and u_y to represent the random accelerations in cross-range and range direction. It is reasonable to assume the accelerations are i.i.d. from subaperture to subaperture, and are zero-mean Gaussian. It is assumed that u_x and u_y are uncorrelated. If $u_x \sim N(0, \sigma_{px}^2)$, $u_y \sim N(0, \sigma_{py}^2)$, the covariance matrix of the process noise $\mathbf{Q}$ can be written as:

$$\mathbf{Q} = \begin{pmatrix} \sigma_{px}^2 & 0 \\ 0 & \sigma_{py}^2 \end{pmatrix} \tag{5.19}$$

In state equation (5.18), the term $-\frac{\Delta}{V_{radar}} R_0$ in matrix $\mathbf{G}$ reflects the effect of range velocity on the image cross-range position.

If we choose the ship centroid measurements from the subaperture images as the measurement variables, then the measurement equation can be set up as:

$$\begin{pmatrix} z_{x,n} \\ z_{y,n} \end{pmatrix} = \underbrace{\begin{pmatrix} 1 & 0 & 0 & 0 \\ 0 & 1 & 0 & 0 \end{pmatrix}}_{\mathbf{H}} \begin{pmatrix} x'_n \\ y'_n \\ v_{c,n} \\ v_{r,n} \end{pmatrix} + \begin{pmatrix} \epsilon_x \\ \epsilon_y \end{pmatrix}, \tag{5.20}$$

where $z_{x,n}$ and $z_{y,n}$ are the centroid measurements in cross-range and range dimension respectively at subaperture n, and ϵ_x and ϵ_y are the ship centroid measurement noises. We assume that the measurement noises are i.i.d. from subaperture to subaperture, and are zero-mean Gaussian. It is reasonable to assume that the measurement noise in range and cross-range ϵ_x and ϵ_y are uncorrelated, and $\epsilon_x \sim N(0, \sigma_x^2)$, $\epsilon_y \sim N(0, \sigma_y^2)$. The variances of the ship centroid measurement noise σ_x^2 and σ_y^2 have been investigated in Chapter 4. The covariance matrix of the measurement noise $\mathbf{R}$ can be written as:

$$\mathbf{R} = \begin{pmatrix} \sigma_x^2 & 0 \\ 0 & \sigma_y^2 \end{pmatrix}. \tag{5.21}$$

With the state equation (5.18) and the measurement equation (5.20), we can see that the system is time-invariant and the noises are stationary. It is easy to show that both of the matrices $\mathbf{M}$ and $\mathbf{W}$ in (5.13) and (5.14) have rank 4, thus the system is completely observable and controllable. As a result, the system has a steady-state solution.

We remark that the state equation (5.18) holds under a certain assumption. Equation (5.18) is derived from the equations of ship actual position. For the ship actual

positions in the subapertures, we have:

$$x''_{n+1} = x''_n + v_{c,n}\Delta + \frac{\Delta^2}{2}u_x \tag{5.22}$$

$$y''_{n+1} = y''_n + v_{r,n}\Delta + \frac{\Delta^2}{2}u_y \tag{5.23}$$

$$v_{c,n+1} = v_{c,n} + u_x\Delta \tag{5.24}$$

$$v_{r,n+1} = v_{r,n} + u_y\Delta \tag{5.25}$$

For the ship image position, the range image position is the same as the actual range position. Thus the state equation for the ship range image position in (5.18) is given by

$$y'_{n+1} = y'_n + v_{r,n}\Delta + \frac{\Delta^2}{2}u_y. \tag{5.26}$$

However, the cross-range image position is different from the actual cross-range position if the ship has slant-range velocity. The relationship between the image position and the actual position in cross-range dimension can be expressed as:

$$x' = (x'' - \frac{v_r}{V_{radar}}R_0 + \frac{D}{2}) \text{ modulo } D - \frac{D}{2}, \tag{5.27}$$

where D is the patch size in cross-range dimension. In (5.27), terms $+\frac{D}{2}$ and $-\frac{D}{2}$ are added since the patch center is assumed to be origins of coordinates (x', y') and (x'', y''). We define A modulo D as:

$$A \text{ modulo } D = A \pm nD, \tag{5.28}$$

where n is an integer which makes $0 \leq A + nD < D$.

At subaperture $n+1$, the cross-range image position can be expressed as:

$$x'_{n+1} = (x''_{n+1} - \frac{v_{r,n+1}}{V_{radar}}R_0 + \frac{D}{2}) \text{ modulo } D - \frac{D}{2}. \tag{5.29}$$

Substituting (5.22) and (5.25) into (5.29), we have

$$x'_{n+1} = (x''_n + v_{c,n}\Delta + \frac{\Delta^2}{2}u_x - \frac{v_{r,n}}{V_{radar}}R_0 - \frac{u_y\Delta}{V_{radar}}R_0 + \frac{D}{2}) \text{ modulo } D - \frac{D}{2}. \tag{5.30}$$

If we assume that

$$\begin{aligned} & (x''_n + v_{c,n}\Delta + \tfrac{\Delta^2}{2}u_x - \tfrac{v_{r,n}}{V_{radar}}R_0 - \tfrac{u_y\Delta}{V_{radar}}R_0 + \tfrac{D}{2}) \text{ modulo } D \\ = \; & (x''_n - \tfrac{v_{r,n}}{V_{radar}}R_0 + \tfrac{D}{2}) \text{ modulo } D + v_{c,n}\Delta + \tfrac{\Delta^2}{2}u_x - \tfrac{u_y\Delta}{V_{radar}}R_0, \end{aligned} \tag{5.31}$$

then (5.30) can be rewritten as:

$$\begin{aligned} x'_{n+1} &= (x''_n - \frac{v_{r,n}}{V_{radar}} R_0 + \frac{D}{2}) \text{ modulo } D + v_{c,n}\Delta + \frac{\Delta^2}{2}u_x - \frac{u_y\Delta}{V_{radar}}R_0 - \frac{D}{2} \\ &= x'_n + v_{c,n}\Delta + \frac{\Delta^2}{2}u_x - \frac{u_y\Delta}{V_{radar}}R_0 \end{aligned} \tag{5.32}$$

since $x'_n = (x''_n - \frac{v_{r,n}}{V_{radar}} R_0 + \frac{D}{2})$ modulo $D - \frac{D}{2}$. Equation (5.32) is the state equation for the ship cross-range image position in (5.18).

The assumption in (5.31) can be rewritten as:

$$\begin{aligned} & ((x''_n - \tfrac{v_{r,n}}{V_{radar}} R_0 + \tfrac{D}{2}) \text{ modulo } D + v_{c,n}\Delta + \tfrac{\Delta^2}{2}u_x - \tfrac{u_y\Delta}{V_{radar}}R_0) \text{ modulo } D \\ = \quad & (x''_n - \tfrac{v_{r,n}}{V_{radar}} R_0 + \tfrac{D}{2}) \text{ modulo } D + v_{c,n}\Delta + \tfrac{\Delta^2}{2}u_x - \tfrac{u_y\Delta}{V_{radar}}R_0 \end{aligned} \tag{5.33}$$

since $(A + B)$ modulo $D = (A$ modulo $D + B)$ modulo D. Thus, the assumption in Equation (5.33) is valid if

$$0 \le (x''_n - \frac{v_{r,n}}{V_{radar}} R_0 + \frac{D}{2}) \text{ modulo } D + v_{c,n}\Delta + \frac{\Delta^2}{2}u_x - \frac{u_y\Delta}{V_{radar}}R_0 < D \tag{5.34}$$

That is to say, the assumption in (5.31) holds if the summation of the ship movement during Δ and the perturbation in cross-range $\delta = v_{c,n}\Delta + \frac{\Delta^2}{2}u_x - \frac{u_y\Delta}{V_{radar}}R_0$, does not make $(x''_n - \frac{v_{r,n}}{V_{radar}} R_0 + \frac{D}{2})$ modulo D exceed region [0,D). This usually holds when $|\delta|$ is small compared to D, and $(x''_n - \frac{v_{r,n}}{V_{radar}} R_0 + \frac{D}{2})$ modulo D is not at the boundary 0 or D.

5.3.2 Simulating Noisy Measurements

In RIG images, the target centers-of-mass are located at the center of the images. Thus, we cannot get the actual ship centroid measurements from the images produced by RIG. As a result, the ship centroid measurement from the subaperture images must be *simulated* by (5.18) and (5.20). To simulate the noisy measurement, we have to determine the process noise covariance matrix **Q** and the measurement noise covariance matrix **R**.

The process noise covariance matrix and the measurement noise covariance matrix play important roles in the overall performance of a Kalman filter. The Kalman gain is directly proportional to the process noise covariance matrix and inversely proportional

to the measurement noise covariance matrix. This makes sense because if we do not trust our state model, then $\mathbf{Q}$ will be large. A large $\mathbf{Q}$ will increase the Kalman gain, which will force the filter to weigh the measurement more. Conversely, if the measurements are very noisy, then $\mathbf{R}$ will be large. A large $\mathbf{R}$ will decrease the Kalman gain, which will allow the filter to weigh the measurement less. Therefore, it is important to estimate both the $\mathbf{Q}$ and $\mathbf{R}$ accurately.

However, the "proper amount" of process noise is application-dependent and no systematic procedure exists for determining it. In our study, the ship is assumed to be moving at a nearly constant velocity. Thus we choose the variances of the random accelerations in range and cross-range to be very small, which is $1 \times 10^{-8} m^2/sec^2$. Therefore,

$$\mathbf{Q} = \begin{pmatrix} 1 \times 10^{-8} & 0 \\ 0 & 1 \times 10^{-8} \end{pmatrix}. \tag{5.35}$$

The variances of the ship centroid measurement noise have been given in Chapter 4. The measurement noise is caused by two sources, one is the image noise (the image pixel intensity is noisy), and the other is the image resolution. The measurement noise from image noise is affected by the statistical properties of the ship pixel intensity, the ship shape, and the ship velocity. Therefore, the centroid measurement noise variances may vary from subaperture to subaperture. However, in our study, it is assumed that the ship rotational motion is small enough to be ignored. Thus the ship shape in the subaperture image sequence does not change significantly, and the centroid measurement noise does not change significantly from subaperture to subaperture with the same ship velocity. As a result, we can assume that the measurement noise covariance matrix is time-invariant. We use the average centroid measurement variance of the subaperture image sequence to determine the measurement noise covariance matrix $\mathbf{R}$.

5.3.3 Initialization of Kalman Filter

Recall from Section 5.2.3, a Kalman filter is called consistent if the state estimation errors are compatible with the filter-calculated covariance. To make a Kalman filter consistent, it is important for the initial state covariance $\Sigma_{0|0}$ to reflect its accuracy

realistically. If we initialize $\Sigma_{0|0}$ with a small value, but a large error actually exists in the initial estimate, then the error will persist for a long time. It is because the small $\Sigma_{0|0}$ leads to a low Kalman gain, and thus the new measurement receives a low weighting.

How can we initialize the Kalman filter properly if we only have the ship centroid measurements from the subaperture images? A practical way to initialize the Kalman filter can be done as follows [3]. We denote the first two measurements as $(z_{x,-1}, z_{y,-1})^T$ and $(z_{x,0}, z_{y,0})^T$. The initial state estimate $\underline{\hat{X}}_{0|0}$ is:

$$\hat{x}'_{0|0} = z_{x,0} \tag{5.36}$$

$$\hat{y}'_{0|0} = z_{y,0} \tag{5.37}$$

$$\hat{v}_{c,0|0} = \frac{z_{x,0} - z_{x,-1}}{\Delta} \tag{5.38}$$

$$\hat{v}_{r,0|0} = \frac{z_{y,0} - z_{y,-1}}{\Delta} \tag{5.39}$$

The initial covariance matrix $\Sigma_{0|0}$ is:

$$\Sigma_{0|0} = \begin{pmatrix} \sigma_x^2 & 0 & \sigma_x^2/\Delta & 0 \\ 0 & \sigma_y^2 & 0 & \sigma_y^2/\Delta \\ \sigma_x^2/\Delta & 0 & 2\sigma_x^2/\Delta^2 & 0 \\ 0 & \sigma_y^2/\Delta & 0 & 2\sigma_y^2/\Delta^2 \end{pmatrix} \tag{5.40}$$

This method guarantees consistency of the Kalman filter [3].

5.4 Experimental Results for Ship Velocity Estimation

The ship centroid measurement noise is caused by two sources, image noise and image resolution. As shown in Section 4.9, the measurement noise due to image noise is related to the statistical properties of image pixel intensity and the ship velocity. The measurement noises increase with increased ship velocity.

When we simulate the observations, we assume that we know the statistical properties of the pixel intensities and the ship velocity. Thus, the exact measurement

ship heading 45 degrees	range(m^2)	cross-range(m^2)
$v = 4$, 0.3sec integration time	1.0300	4.8133
$v = 4$, 1.5sec integration time	0.3823	1.6597
$v = 8$, 0.3sec integration time	1.0750	8.0226
$v = 8$, 1.5sec integration time	0.5066	2.7503

Table 5.1: Centroid measurement noise variances used in the simulations in this section ($VAR(x_{nc})$ in Eq. (4.13))

noise variances are used in the measurement noise covariance matrix $\mathbf{R}$ when the observations are simulated. However, when we use a Kalman filter to estimate the ship velocity from the observations, it is unreasonable to assume that we know the exact measurement noises, since it is unreasonable to assume that we know the statistical properties of image pixel intensities and the ship velocity. Therefore, the centroid measurement noise due to image resolution is used as the measurement noise in our Kalman filter model for the ship velocity estimation. The measurement noise variances due to image resolution can be easily calculated from the SAR parameters. As a result, it is necessary to determine how well the Kalman filter can estimate the ship velocity when the measurement noise covariance matrix in our model does not perfectly reflect the true measurement noise. In addition, we assume that the process noise covariance matrix can be estimated correctly. That is to say, the same process noise covariance matrix is used for the observation simulation and in the Kalman filter model for ship velocity estimation.

The measurement noise variances, due to image noise, required for the observation simulations in this section are listed in Table 5.1. The variance in this table is the average noise variance of the subaperture image sequence, and it is obtained with 300 Monte-Carlo runs. With the SAR parameters in Section 3.4, the integration time for a high-resolution image is 15.8sec. Thus, there are 53 subaperture images with subaperture integration time 0.3sec, and 11 subaperture images with subaperture integration time 1.5sec.

In Figures 5.1 to 5.20, the performance of a Kalman filter with both perfect and imperfect measurement noise are investigated for integration times 0.3sec and 1.5sec, with ship heading 45 degrees and ship velocity 4m/sec. Figures 5.1 to 5.6 (0.3sec integration time), and Figures 5.13 to 5.16 (1.5sec integration time) show the results for the cases in which we assume that the measurement noise is known exactly when we use the Kalman filter to estimate the ship velocity. Figures 5.7 to 5.12 (0.3sec integration time), and Figures 5.17 to 5.20 (1.5sec integration time) show the results for the cases in which only the measurement noise due to image resolution is used as the measurement noise for the Kalman filter. For each case, the bias and the variance of ship velocity estimation are given. The consistency performance from Monte-Carlo runs is given for subaperture integration time 0.3sec.

The bias and the variance of the state estimation from Monte-Carlo runs are calculated as

$$b = \frac{1}{N}\sum_{i=1}^{N}(\hat{x}_{t|t,i} - x_t) \tag{5.41}$$

and

$$v = \frac{1}{N}\sum_{i=1}^{N}(\hat{x}_{t|t,i} - x_t)^2 \tag{5.42}$$

where N is the number of Monte-Carlo runs, x_t is the true state value at time t, and $\hat{x}_{t|t}$ is the state estimation.

The consistency of the Kalman filter is checked from the results of Monte-Carlo runs. Recall in Section 5.2.3, we define the normalized state estimation error squared ϵ_t and the normalized innovations squared ϵ_t'. In our simulation, 25 Monte-Carlo runs are conducted. Thus 25 independent samples of the random variable ϵ_t and ϵ_t' are obtained for every t.

The sample mean of the normalized state estimation error squared is:

$$\bar{\epsilon}_t = \frac{1}{25}\sum_{i=1}^{25}\epsilon_t^i. \tag{5.43}$$

In our Kalman filter model, the dimension of the state vector is 4. Therefore, if the state estimation errors are consistent with filter-calculated covariances, $\sum_{i=1}^{25}\epsilon_t^i$ should have a Chi-square density with $25 \times 4 = 100$ degrees of freedom. For a 100-degree-of-freedom Chi-square random variable, the 95% confidence region is

$$P\{\chi^2_{100} \in [74.2, 129.6]\} = 0.95. \tag{5.44}$$

Dividing the above results by 25, the 95% confidence region for $\bar{\epsilon}_t$ is $[2.968, 5.184]$.

The sample mean of the normalized innovations squared is:

$$\bar{\epsilon}'_t = \frac{1}{25}\sum_{i=1}^{25} \epsilon_t'^i. \tag{5.45}$$

In our Kalman filter model, the dimension of the measurement vector is 2. Therefore, if the filter is consistent, $\sum_{i=1}^{25} \epsilon_t'^i$ should be Chi-square distributed with $25 \times 2 = 50$ degrees of freedom, For a 50-degree-of-freedom Chi-square random variable, the 95% confidence region is

$$P\{\chi^2_{50} \in [32.3, 71.4]\} = 0.95. \tag{5.46}$$

Dividing the above results by 25, the 95% confidence region for $\bar{\epsilon}_t$ is $[1.292, 2.856]$.

From Figures 5.1 to 5.4 and Figures 5.13 to 5.16, we can see that with perfect measurement noise, the Kalman filter can estimate the ship velocity well. The bias and the variance of the velocity estimation from 100 Monte-Carlo runs are close to zero after some frames. The velocity estimation variance from 100 Monte-Carlo runs matches with the filter-calculated variance in Figures 5.3, 5.4, 5.15 and 5.16. The consistency of the Kalman filter is verified by Figures 5.5 and 5.6, which show the average normalized state error squared and innovation squared from 25 Monte-Carlo runs. The dotted lines indicate the 95% confidence region, and we can see that almost all the points fall inside the confidence region.

From Figures 5.7 to 5.10 and Figures 5.17 to 5.20, we can see that with imperfect measurement noise, the Kalman filter can still estimate the ship velocity well, since the bias and the variance of the velocity estimation from 100 Monte-Carlo runs are close to zero after some frames. However, from Figures 5.9, 5.10, 5.19 and 5.20, we can see that the velocity estimation variance from 100 Monte-Carlo runs does not match the filter-calculated variance. The inconsistency of the Kalman filter is verified by Figures 5.11 and 5.12, which show the average normalized state error squared and innovation squared from 25 Monte-Carlo runs. The dotted lines indicate the 95% confidence region, and we can see that all the points fall far away outside the confidence region, indicating a mismatch between our Kalman filter model and the true system. This inconsistency is because the measurement noise covariance matrix in our system model does not reflect the true measurement noise.

In Figures 5.10 and 5.20, for the cross-range velocity estimation, the mismatch between the variance from the Monte-Carlo runs and the filter-calculated variance is not that obvious. This is because the cross-range resolution in subaperture images is low, which leads to a large measurement noise. As a result, the measurement noise caused by image noise is small compared to the noise caused by image resolution, and the imperfect noise is close to the perfect noise in the cross-range. Thus, the performance of the mismatched filter is close to that of a matched filter for cross-range velocity estimation.

In Figures 5.21 and 5.22, the ship velocity estimation variances from 100 Monte-Carlo runs are shown on a log scale for 0.3sec and 1.5sec integration time with imperfect measurement noise at ship velocity 4m/sec. There are 53 subaperture images with the subaperture integration time 0.3sec, and 11 subaperture images with the subaperture integration time 1.5sec. From Figures 5.21 and 5.22, we can see that the velocity estimation variances at 11 frames for 1.5sec are smaller than the variances at 53 frames for 0.3sec, when the ship velocity is 4m/sec and ship heading is 45 degrees. The numerical results are give in Table 5.2.

From Figures 5.21 and 5.22, we can see that with the same frame number, the velocity estimation variance for the 1.5sec case is smaller than that for the 0.3sec case. This is because with the same ship velocity, the centroid estimation variance for 1.5sec is smaller than that for 0.3sec, as we mentioned in the conclusion of Section 4.9. Therefore, there is a tradeoff on how to choose the subaperture integration time. More ship centroid measurements can be obtained to make the Kalman filter converge if we choose a short subaperture integration time. However, the measurement noise can be reduced if we choose a suitably long subaperture integration time. From Figure 5.21 and 5.22, we can find out the proper frame number and subaperture integration time with the given velocity estimation variances.

In Figure 5.23 and 5.24, the ship velocity estimation variances with different true ship velocities $v = 4m/sec$ and $v = 8m/sec$, for 1.5sec subaperture integration time are given on a log scale. We can see that the smaller the true ship velocity is, the smaller the estimation variance is, which means the better we can estimate the velocity. This observation is a result of the conclusion in Section 4.9: with the same

ship heading is 45 degrees	range(m^2/sec^2)	cross-range(m^2/sec^2)
$v = 4$, 0.3sec int.time, 53 frame	0.0020	0.0546
$v = 4$, 1.5sec int.time 11 frame	0.0012	0.0149
$v = 8$, 1.5sec int.time 11 frame	0.0017	0.0195

Table 5.2: Ship velocity estimation variance with imperfect measurement noise from 100 Monte-Carlo runs

subaperture integration time, the smaller the ship velocity is, the smaller the ship centroid measurement noise variance is. This observation is obvious with cross-range velocity estimation in Figure 5.24, while not obvious with range velocity estimation in Figure 5.23. This is because the increase of measurement noise variance in cross-range is much larger than that in range (see Table 5.1), when the ship velocity increases from 4m/sec to 8m/sec.

The results in Figures 5.21 to 5.24 and Table 5.2 are from Monte-Carlo runs. Since our Kalman filter model for the ship velocity estimation does not match the true system, it is not necessary to consider the filter-calculated results.

The conclusions we obtained from this section are:

- Despite a mismatch between the measurement noise in our Kalman filter and the true measurement noise, we can still estimate ship velocity well.
- No *a priori* knowledge of ship velocity is required for the velocity estimation.
- With the same ship velocity, 1.5sec subaperture integration time can achieve more accurate ship velocity estimation than 0.3sec integration time within 15.8sec.
- With the same subaperture integration time, the smaller the true ship velocity is, the better we can estimate the velocity. This follows from the conclusion in Section 4.9: with the same subaperture integration time, the smaller the ship velocity is, the smaller the ship centroid measurement noise variance is.

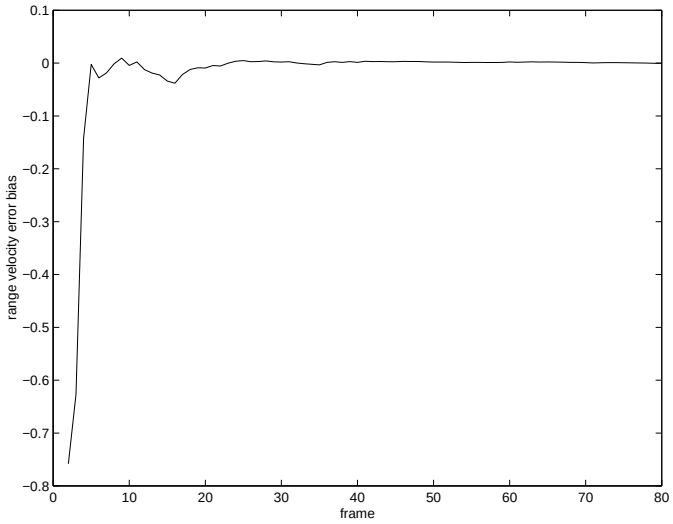

Figure 5.1: The bias of ship slant range velocity estimation at ship speed v=4m/sec and heading 45 degrees with integration time 0.3sec (100 Monte-Carlo runs with perfect measurement noise)

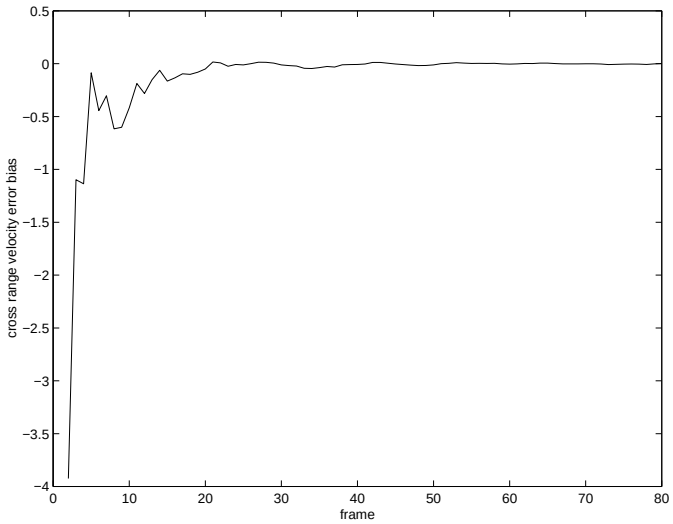

Figure 5.2: The bias of ship cross-range velocity estimation at ship speed v=4m/sec and heading 45 degrees with integration time 0.3sec (100 Monte-Carlo runs with perfect measurement noise)

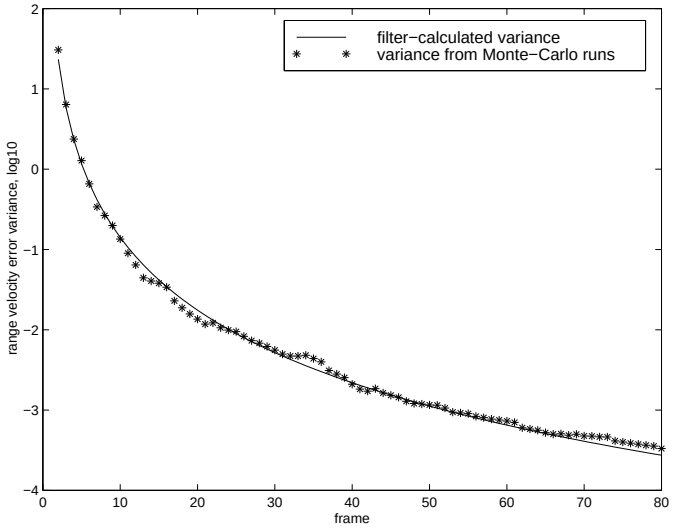

Figure 5.3: The variance of ship slant range velocity estimation at ship speed v=4m/sec and heading 45 degrees with integration time 0.3sec (100 Monte-Carlo runs with perfect measurement noise). The figure is plotted on a log scale.

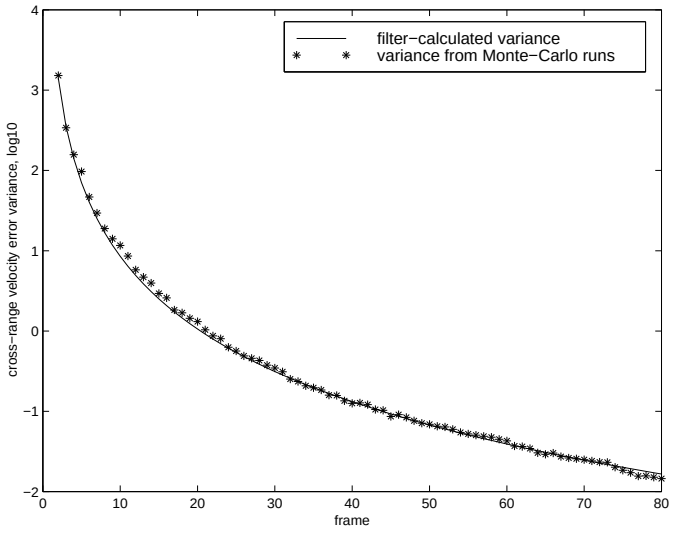

Figure 5.4: The variance of ship cross-range velocity estimation at ship speed v=4m/sec and heading 45 degrees with integration time 0.3sec (100 Monte-Carlo runs with perfect measurement noise). The figure is plotted on a log scale.

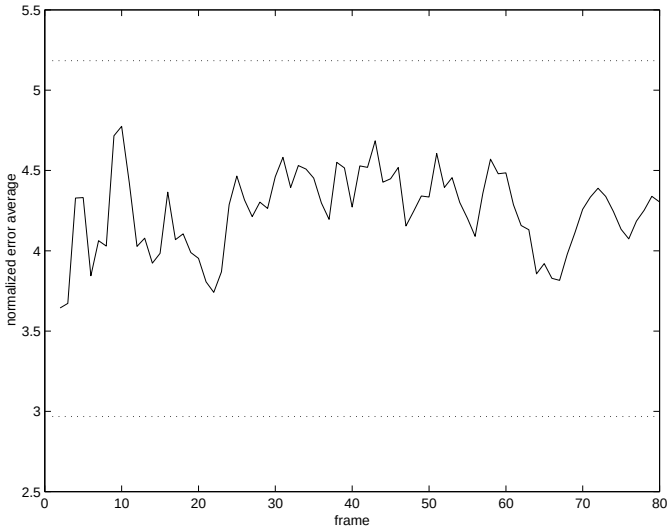

Figure 5.5: Average of normalized state error squared from 25 Monte-Carlo runs with 95% confidence region for integration time 0.3sec, ship speed v=4m/sec and heading 45 degrees, with perfect measurement noise

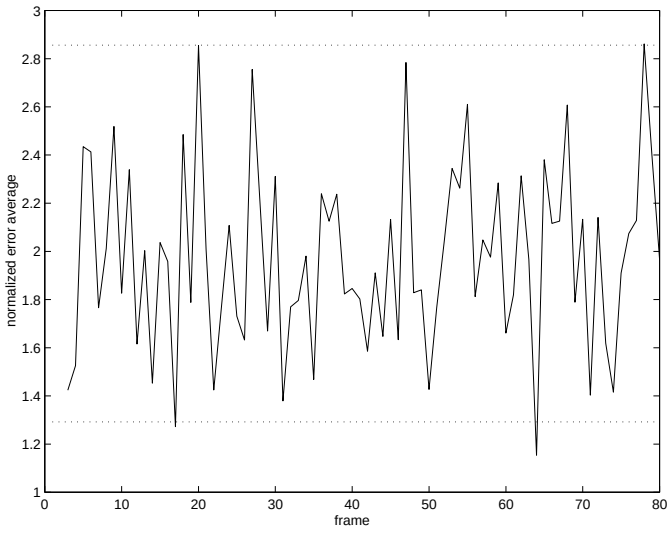

Figure 5.6: Average of normalized innovation squared from 25 Monte-Carlo runs with 95% confidence region for integration time 0.3sec, ship speed v=4m/sec and heading 45 degrees, with perfect measurement noise

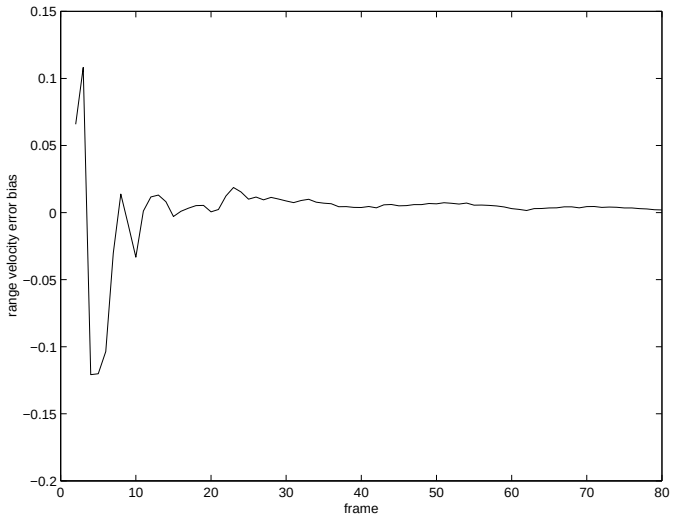

Figure 5.7: The bias of ship slant range velocity estimation at ship speed v=4m/sec and heading 45 degrees with integration time 0.3sec (100 Monte-Carlo runs with imperfect measurement noise)

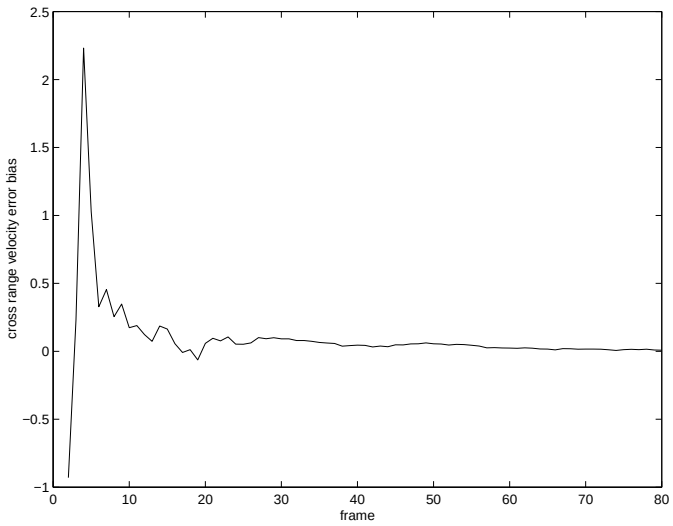

Figure 5.8: The bias of ship cross range velocity estimation at ship speed v=4m/sec and heading 45 degrees with integration time 0.3sec (100 Monte-Carlo runs with imperfect measurement noise)

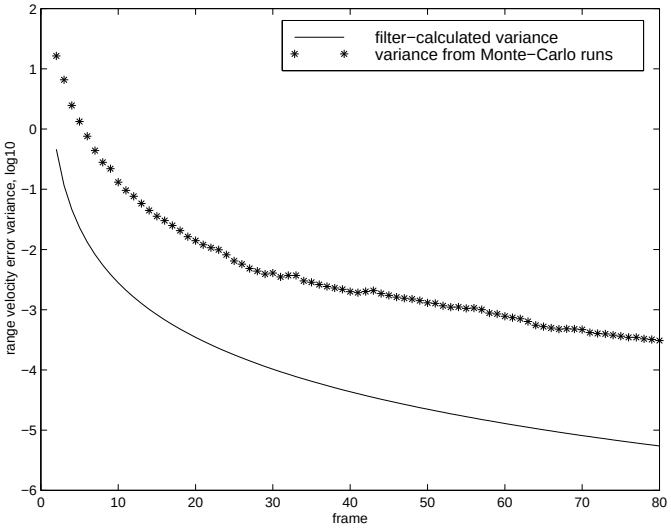

Figure 5.9: The variance of ship slant range velocity estimation at ship speed v=4m/sec and heading 45 degrees with integration time 0.3sec (100 Monte-Carlo runs with imperfect measurement noise). The figure is plotted on a log scale.

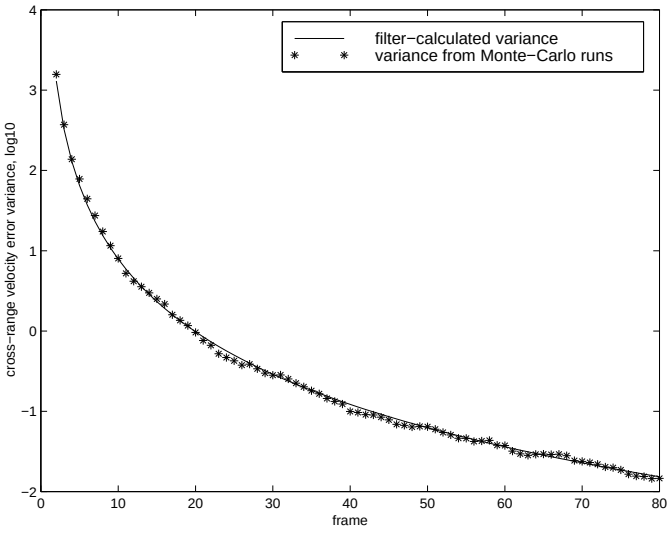

Figure 5.10: The variance of ship cross-range velocity estimation at ship speed v=4m/sec and heading 45 degrees with integration time 0.3sec (100 Monte-Carlo runs with imperfect measurement noise). The figure is plotted on a log scale.

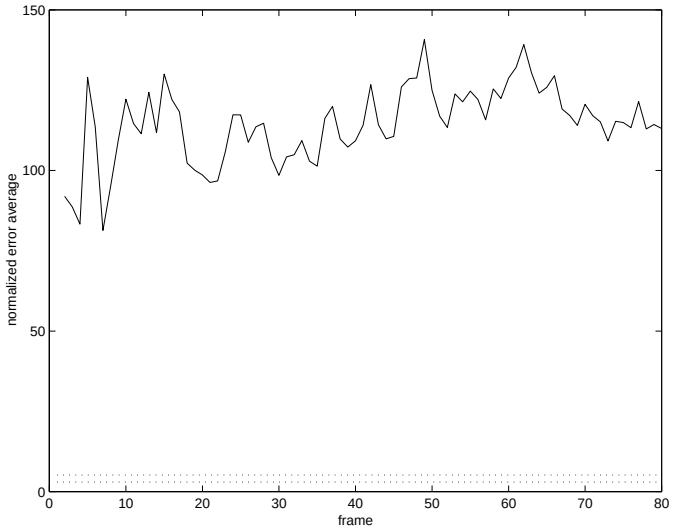

Figure 5.11: Average of normalized state error squared from 25 Monte-Carlo runs with 95% confidence region for integration time 0.3sec, ship speed v=4m/sec and heading 45 degrees, with imperfect measurement noise

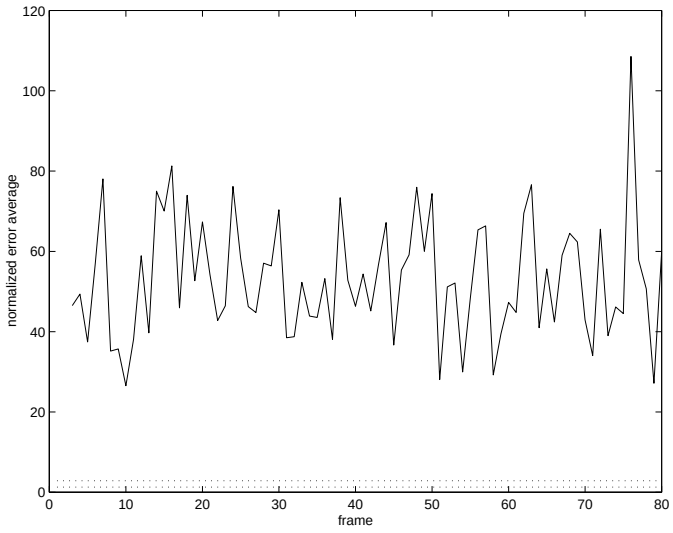

Figure 5.12: Average of normalized innovation squared from 25 Monte-Carlo runs with 95% confidence region for integration time 0.3sec, ship speed v=4m/sec and heading 45 degrees, with imperfect measurement noise

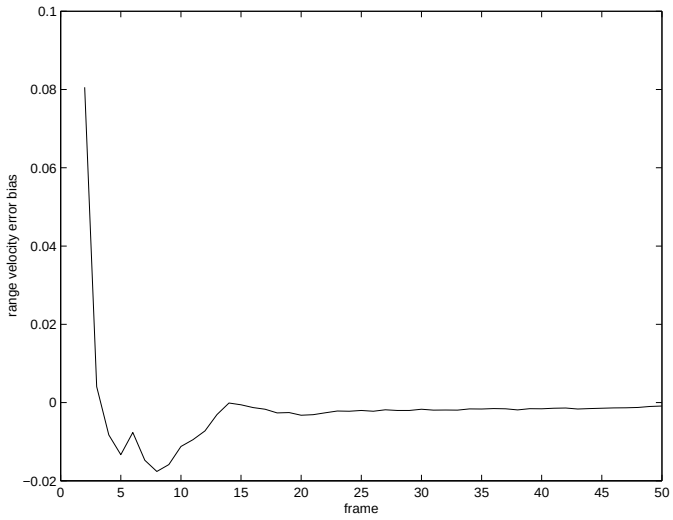

Figure 5.13: The bias of ship slant range velocity estimation at ship speed v=4m/sec and heading 45 degrees with integration time 1.5sec (100 Monte-Carlo runs with perfect measurement noise)

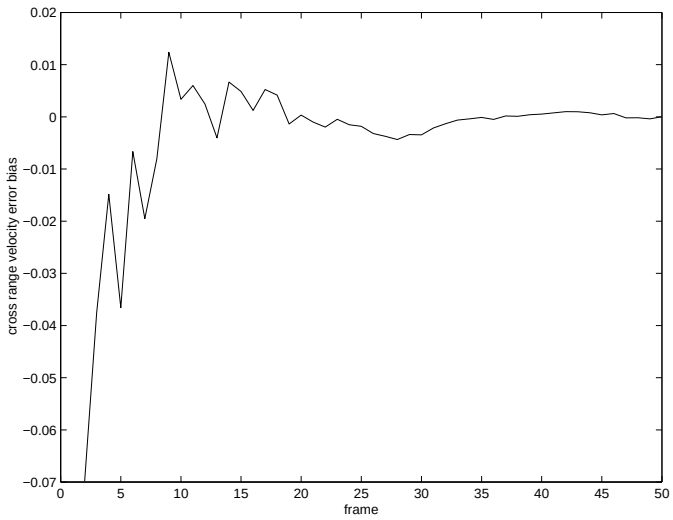

Figure 5.14: The bias of ship cross-range velocity estimation at ship speed v=4m/sec and heading 45 degrees with integration time 1.5sec (100 Monte-Carlo runs with perfect measurement noise)

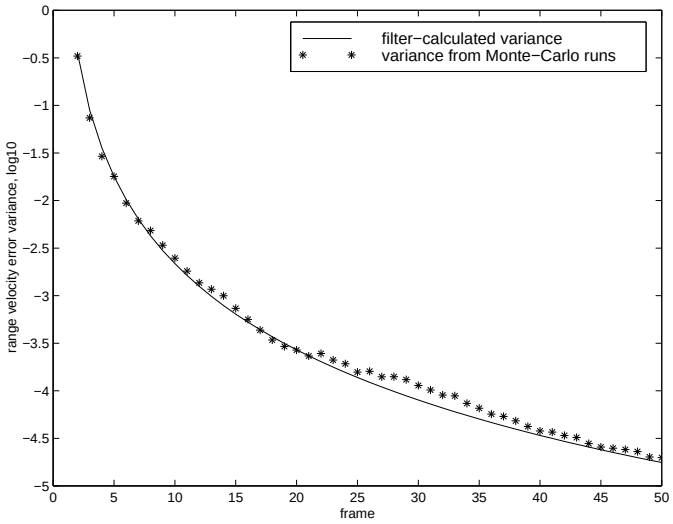

Figure 5.15: The variance of ship slant range velocity estimation at ship speed v=4m/sec and heading 45 degrees with integration time 1.5sec (100 Monte-Carlo runs with perfect measurement noise). The figure is plotted on a log scale.

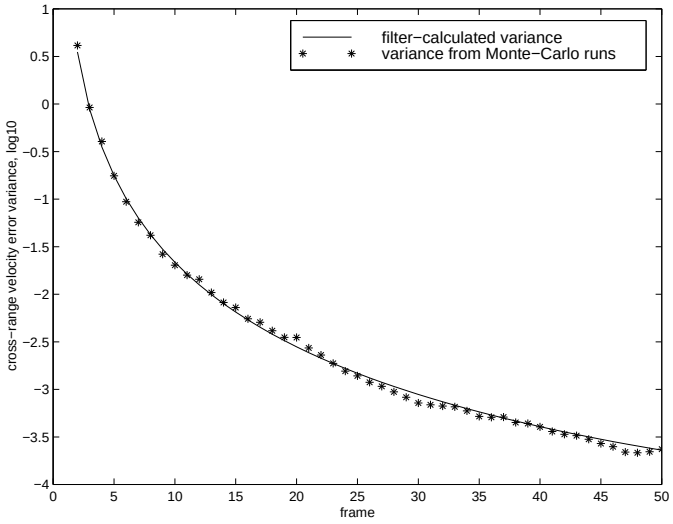

Figure 5.16: The variance of ship cross-range velocity estimation at ship speed v=4m/sec and heading 45 degrees with integration time 1.5sec (100 Monte-Carlo runs with perfect measurement noise). The figure is plotted on a log scale.

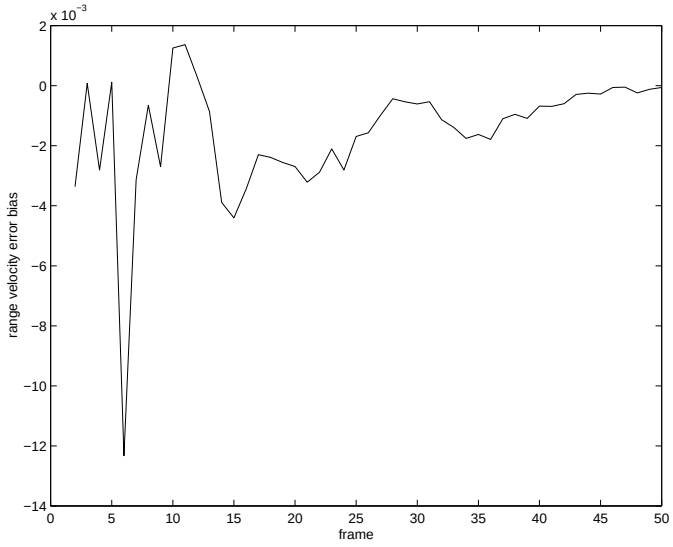

Figure 5.17: The bias of ship slant range velocity estimation at ship speed v=4m/sec and heading 45 degrees with integration time 1.5sec (100 Monte-Carlo runs with imperfect measurement noise)

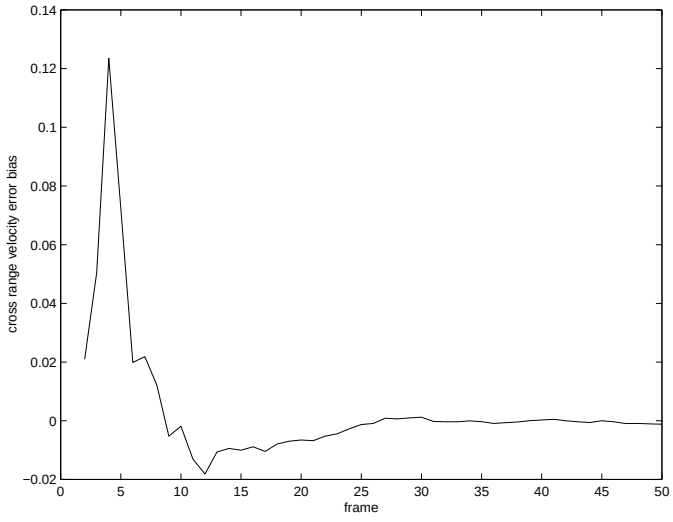

Figure 5.18: The bias of ship cross range velocity estimation at ship speed v=4m/sec and heading 45 degrees with integration time 1.5sec (100 Monte-Carlo runs with imperfect measurement noise)

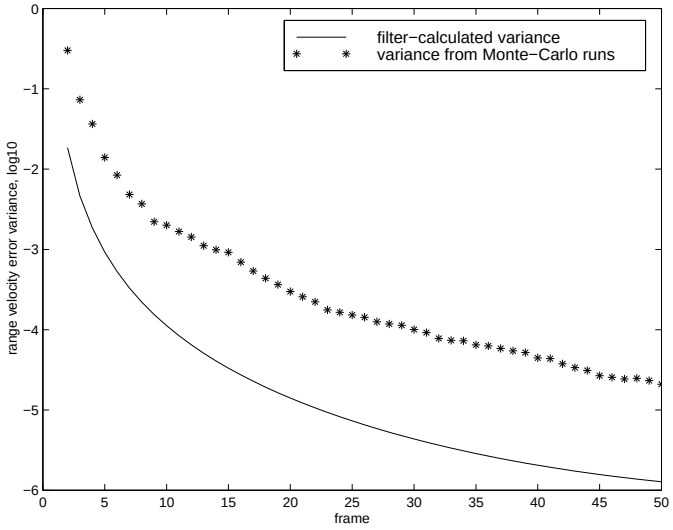

Figure 5.19: The variance of ship slant range velocity estimation at ship speed v=4m/sec and heading 45 degrees with integration time 1.5sec (100 Monte-Carlo runs with imperfect measurement noise). The figure is plotted on a log scale.

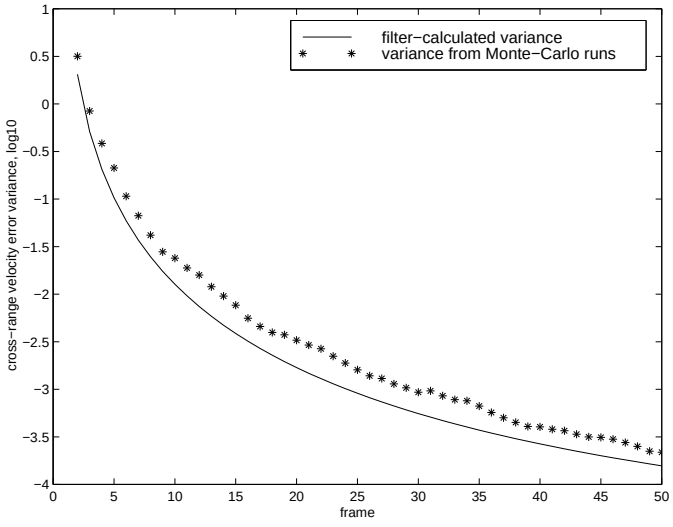

Figure 5.20: The variance of ship cross-range velocity estimation at ship speed v=4m/sec and heading 45 degrees with integration time 1.5sec (100 Monte-Carlo runs with imperfect measurement noise). The figure is plotted on a log scale.

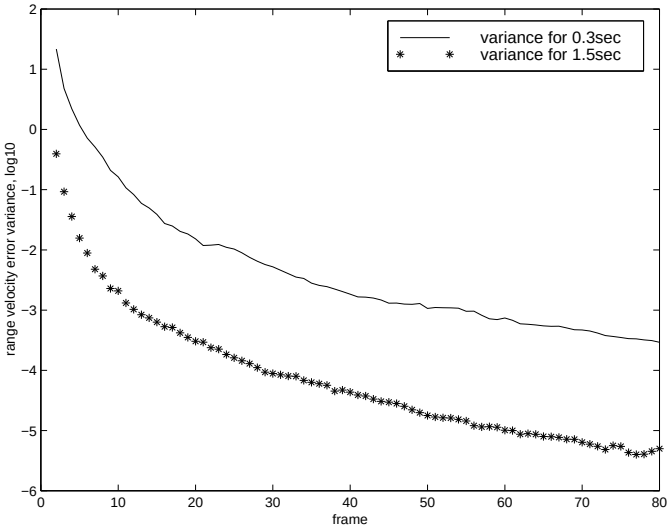

Figure 5.21: The comparison of ship slant range velocity estimation variance for integration time 0.3sec and 1.5sec at ship speed v=4m/sec and heading 45 degrees (100 Monte-Carlo runs with imperfect measurement noise). The figure is plotted on a log scale.

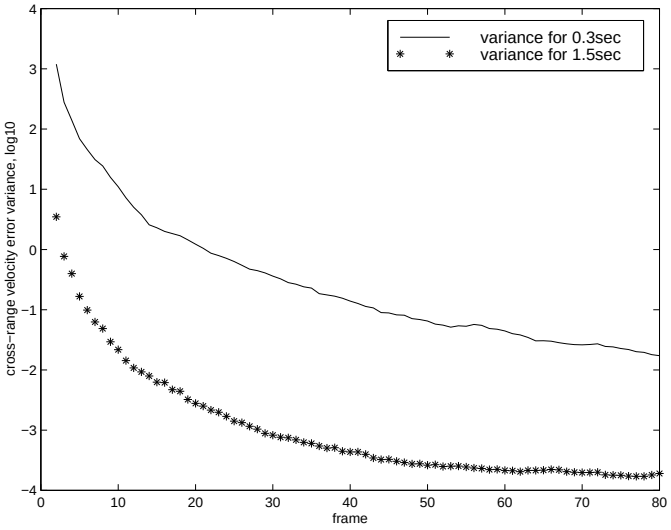

Figure 5.22: The comparison of ship cross-range velocity estimation variance for integration time 0.3sec and 1.5sec at ship speed v=4m/sec and heading 45 degrees (100 Monte-Carlo runs with imperfect measurement noise). The figure is plotted on a log scale.

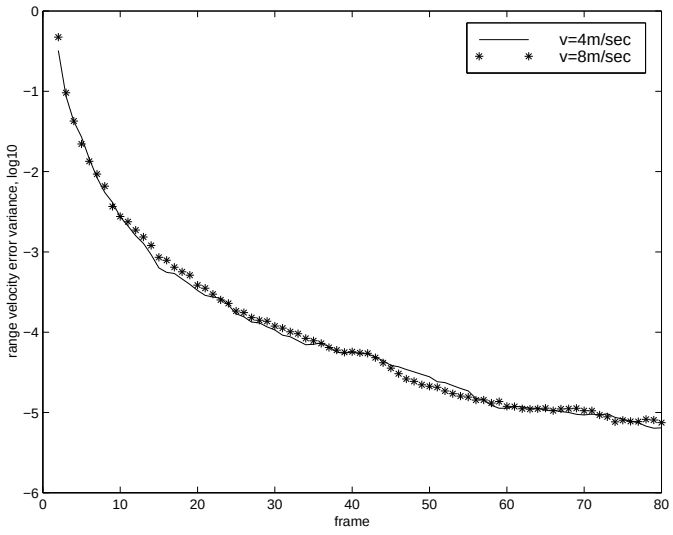

Figure 5.23: The comparison of ship slant range velocity estimation variance for ship speed at v=4m/sec and v=8m/sec, heading 45 degrees with integration time 1.5sec (100 Monte-Carlo runs with imperfect measurement noise). The figure is plotted on a log scale.

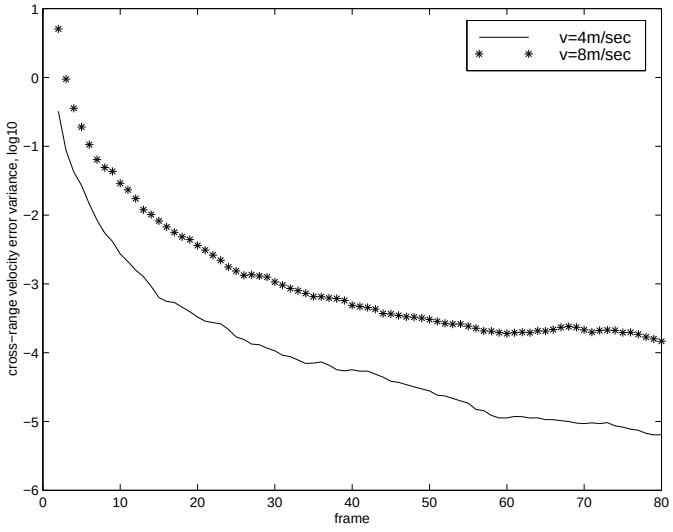

Figure 5.24: The comparison of ship cross-range velocity estimation variance for ship speed at v=4m/sec and v=8m/sec, heading 45 degrees with integration time 1.5sec (100 Monte-Carlo runs with imperfect measurement noise). The figure is plotted on a log scale.

5.5 Application to Spotlight SAR Image Restoration

In Chapter 3, Equation (3.14) shows that in the phase-history data of smeared images, the error phase term is a function of ship velocity. Thus, if we have accurate knowledge of ship velocity, we can compensate the phase error term, and restore the high-resolution smeared images. In the previous sections, we used a Kalman filter to estimate the ship velocity from the ship centroid estimations. In this section, we will use the estimated ship velocity to compensate the phase error term, and see how well we can restore the smeared image.

Assume the true ship velocity is v_r in range and v_c in cross-range, while the estimated velocity from the Kalman filter is $\hat{v}_r$ and $\hat{v}_c$. Recall the phase-history data for the smeared image can be expressed as:

$$G_\epsilon(X', Y') = H(X', Y')G(X', Y'), \tag{5.47}$$

where $H(X', Y') = e^{jv_r \frac{T\lambda}{4\pi\Delta\theta} X'Y'} e^{\frac{V_{radar} v_c}{R_0}(\frac{T\lambda}{4\pi\Delta\theta})^2 X'^2 Y'}$ is the phase error term due to ship motion, and $G(X', Y')$ is the phase-history data of the unsmeared image. To restore the smeared image, we use the estimated ship velocity to compensate the phase error term. The compensated phase-history data $\hat{G}(X', Y')$ is given by:

$$\hat{G}(X', Y') = G_\epsilon(X', Y')/\hat{H}(X', Y'), \tag{5.48}$$

where $\hat{H}(X', Y') = e^{j\hat{v}_r \frac{T\lambda}{4\pi\Delta\theta} X'Y'} e^{\frac{V_{radar} \hat{v}_c}{R_0}(\frac{T\lambda}{4\pi\Delta\theta})^2 X'^2 Y'}$. Furthermore, $\hat{G}(X', Y')$ can be written as:

$$\hat{G}(X', Y') = H_\Delta(X', Y')G(X', Y'), \tag{5.49}$$

where $H_\Delta(X', Y') = e^{j\Delta v_r \frac{T\lambda}{4\pi\Delta\theta} X'Y'} e^{\frac{V_{radar} \Delta v_c}{R_0}(\frac{T\lambda}{4\pi\Delta\theta})^2 X'^2 Y'}$, with $\Delta v_r = v_r - \hat{v}_r$ and $\Delta v_c = v_c - \hat{v}_c$. $H_\Delta(X', Y')$ is the residual phase error term. If the estimated ship velocity is exactly equal to the true velocity, then $H_\Delta(X', Y') = 1$, and the compensated phase-history data $\hat{G}(X', Y')$ is equal to the phase-history data of the unsmeared image. However, if the estimated ship velocity from the Kalman filter is not perfectly accurate, the residual phase error term $H_\Delta(X', Y')$ will exist. As a result, we may not remove the smear completely.

The restored image $\hat{g}(x', y')$ can be obtained with the inverse Fourier transform of the compensated phase-history data $\hat{G}(X', Y')$:

$$\begin{aligned} \hat{g}(x', y') &= IFFT\{\hat{G}(X', Y')\} \\ &= IFFT\{H_{\Delta}(X', Y')\} \otimes g(x', y') \end{aligned} \tag{5.50}$$

Therefore, the restored image is the unsmeared image convolved with an error term which is caused by the inaccuracy of the estimated ship velocity. In Section 5.4, the variances of ship velocity estimation from the Kalman filter were obtained. With the variances of the estimated velocity, we have information concerning Δv_r and Δv_c, and are able to assess how well we can restore the smeared image.

5.6 Experimental Results for Spotlight SAR Image Restoration

In Section 5.4, we found that we can estimate the ship velocity well by Kalman filter even with the mismatched measurement noise covariance matrix. Ship velocity estimation variance was obtained from Monte-Carlo runs. Since the state estimation errors are not consistent with the filter-calculated covariance matrix, there is no meaning to use the filter-calculated variance as the ship velocity estimation variance.

To assess how well we can restore a high-resolution smeared image, we assume the estimated ship velocities are $\hat{v}_r = v_r \pm \sigma_{vr}$ and $\hat{v}_c = v_c \pm \sigma_{vc}$, where v_r and v_c are the true velocities, σ_{vr} and σ_{vc} are the standard deviations of the velocity estimations. Figure 5.25 shows unsmeared and smeared high-resolution images ($0.5m \times 0.5m$ resolution with the parameters in Section 3.4). Figure 5.26 to 5.27 show the results of the restoration for ship velocity $v = 4m/sec$ and $v = 8m/sec$ with ship heading 45 degrees. The ship velocity estimation variances are from Table 5.2. The more accurate the estimated ship velocity is, the better we can restore the smeared image. The resultant images show that we cannot obtain perfect unsmeared high-resolution images if the ship velocities are not estimated exactly. However, within the velocity estimation accuracy from the Kalman filter, we can restore the smeared images to an extent which is good enough for ship classification.

The restored images we obtained contain speckle noise. Speckle reduction techniques in Section 2.8 can be used to improve the resultant image quality.

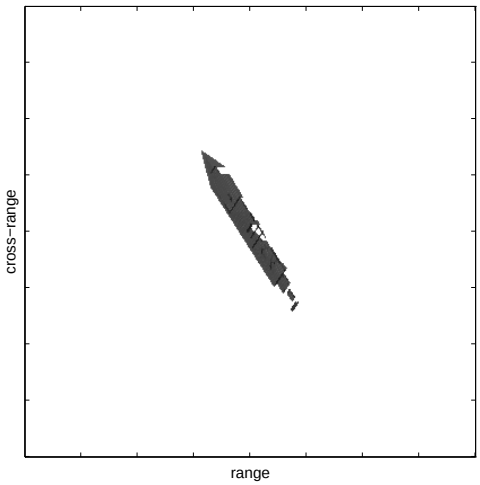

RIG image (400×400 pixels)

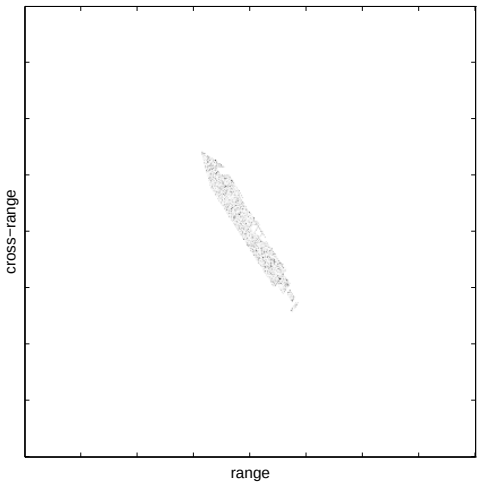

Speckled unsmeared image
(400×400 pixels)

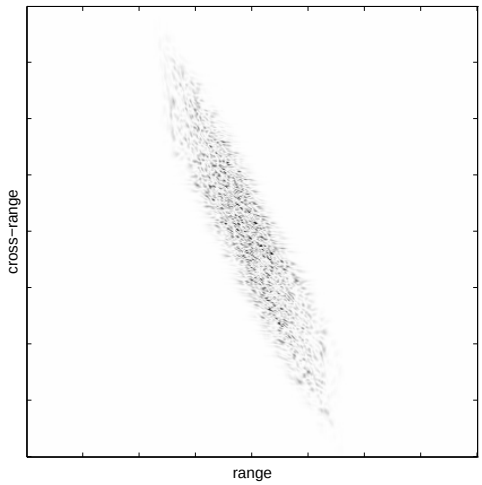

Smeared image with ship speed
$v = 4m/sec$ (400×400 pixels)

Figure 5.25: Images with ship heading 45 degrees and resolution $0.5m \times 0.5m$

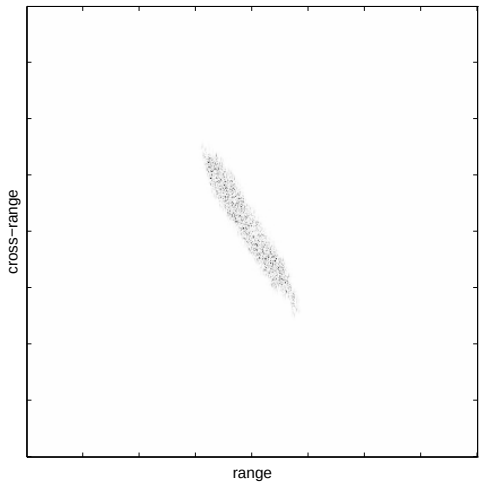

Restored image with ship velocity estimation from 0.3sec subaperture, with $\hat{v}_r = v_r + \sigma_{vr}$ and $\hat{v}_c = v_c + \sigma_{vc}$ (400×400 pixels)

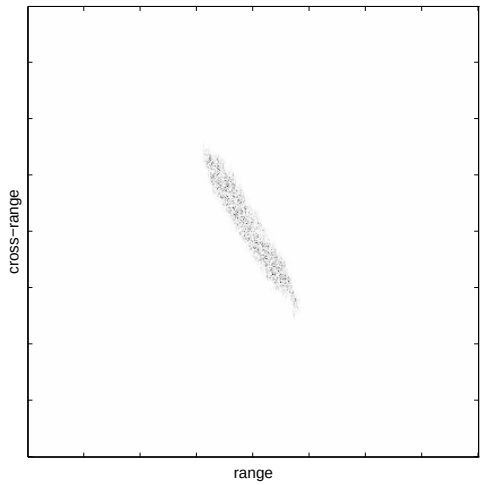

Restored image with ship velocity estimation from 0.3sec subaperture, with $\hat{v}_r = v_r - \sigma_{vr}$ and $\hat{v}_c = v_c - \sigma_{vc}$ (400×400 pixels)

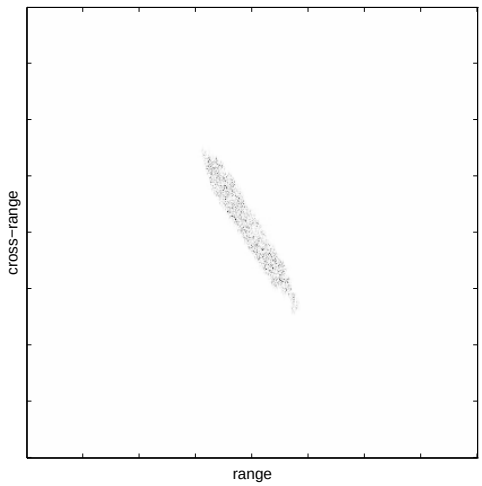

Restored image with ship velocity estimation from 1.5sec subaperture, with $\hat{v}_r = v_r + \sigma_{vr}$ and $\hat{v}_c = v_c + \sigma_{vc}$ (400×400 pixels)

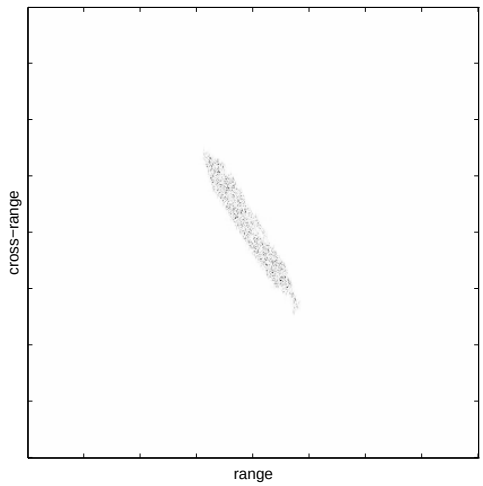

Restored image with ship velocity estimation from 1.5sec subaperture, with $\hat{v}_r = v_r - \sigma_{vr}$ and $\hat{v}_c = v_c - \sigma_{vc}$ (400×400 pixels)

Figure 5.26: Restored images with ship speed $4m/sec$ and heading 45 degrees

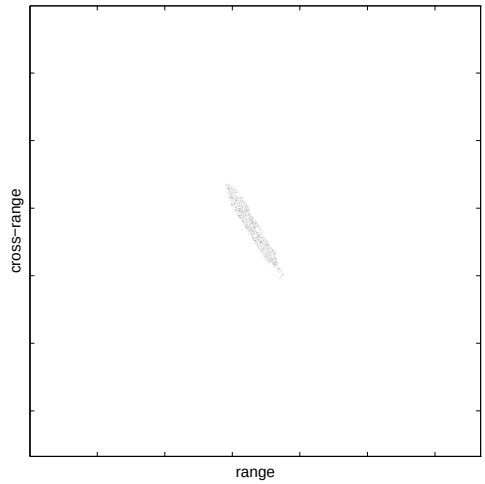

Speckled unsmeared image
(667×667 pixels)

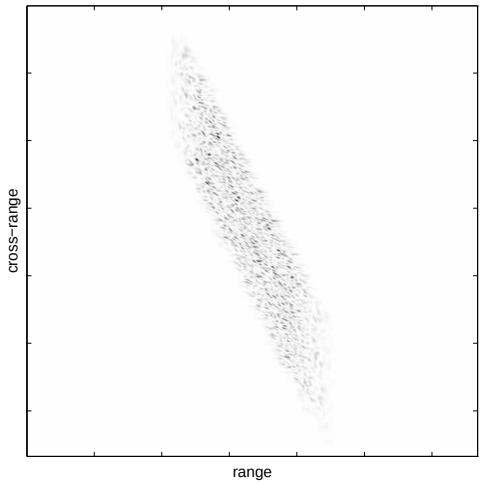

Smeared image with ship velocity
$v = 8m/sec$ (667×667 pixels)

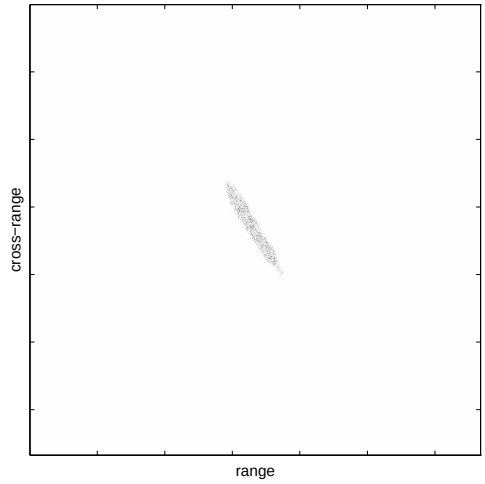

Restored image with ship velocity
estimation from 1.5sec
subaperture, with $\hat{v}_r = v_r + \sigma_{vr}$
and $\hat{v}_c = v_c + \sigma_{vc}$ (667×667 pixels)

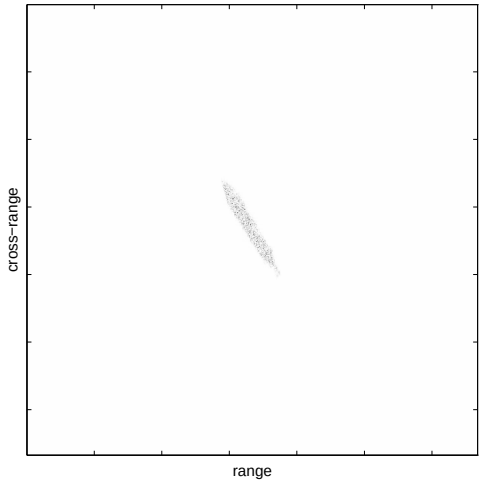

Restored image with ship velocity
estimation from 1.5sec
subaperture, with $\hat{v}_r = v_r - \sigma_{vr}$
and $\hat{v}_c = v_c - \sigma_{vc}$ (667×667 pixels)

Figure 5.27: Restored images with ship speed $8m/sec$ and heading 45 degrees

5.7 Summary

In this chapter, we used a Kalman filter to estimate ship velocity from ship centroid estimations of the subaperture images, and then used the estimated ship velocity to restore the smeared high-resolution SAR image. The results show that even when the measurement noise covariance matrix in our Kalman filter does not match the true measurement noise, we can still estimate the ship velocity well. No *a priori* knowledge of ship velocity is required for the ship velocity estimation. The performance of the Kalman filter and the conclusions for the velocity estimation have been given in Section 5.4. Unsmeared high-resolution images can be obtained only if we have an accurate knowledge of ship velocity. However, within the velocity estimation accuracy from the Kalman filter, we may restore the smeared image to an extent which is good enough for ship classification.

Chapter 6

Summary

In the final chapter, we summarize the research contributions in this thesis, and propose a number of ways in which this thesis work may be further extended.

6.1 Summary

We first recapitulate the problem wanted to solve in this thesis. In spotlight mode SAR, a long integration time is necessary for a high-resolution image. However, if our imaging target is a moving ship at sea, the ship's motion during the long integration time will smear the image. How can we get an unsmeared, high-resolution spotlight SAR image? In this thesis, a novel method is provided to solve the problem.

The contributions of this thesis are:

1. A mathematical model of the smear effect due to a target's constant translational motion is derived in Chapter 3 for airborne spotlight SAR. It is found that in the phase-history domain, the data for a smeared image is equal to the data for an unsmeared image multiplied by a phase error term. The image degradation is investigated from the mathematical model first, and then confirmed by the simulated images. The relationship between image degradation and target velocity is quantified.

2. A novel method is developed in Chapters 4 and 5 to achieve motion compensation, and thus obtained unsmeared, high-resolution spotlight SAR images for

moving ships. In our method, the ship velocity is estimated by a Kalman filter from ship centroid measurements obtained from subaperture images. The estimated ship velocity is used to compensate the phase error term in the phase-history data for a smeared image. Thus, an unsmeared, high-resolution image can be obtained. No *a priori* knowledge of ship velocity is required for the velocity estimation in this method.

In the experiments, a mismatched measurement noise covariance matrix is used in the Kalman filter to estimate the ship velocity, since we do not know the true ship velocity. However, it is shown that we can still estimate the ship velocity with reasonable accuracy by Kalman filter with the mismatched measurement noise. The design implications are that the subaperture integration time may be optimized using the methods developed in this thesis. In the examples given in the thesis, the smaller the true ship velocity, the better we can estimate the ship velocity. In addition, we found that with the same ship velocity, 1.5sec subaperture integration time can achieve more accurate ship velocity estimates than a 0.3sec integration time within a 15.8sec total integration time.

3. The variance of target centroids have been analytically derived for both unsmeared and smeared images in Chapter 4. The derivation for unsmeared images is more general than the work reported in [4] and [27], while the derivation for smeared images, to the best of our knowledge, does not appear in the open literature. These analyses are verified by simulation results from Monte-Carlo runs.

6.2 Future Work

1. In Chapter 5, the measurement noise covariance matrix in the Kalman filter for ship velocity estimation does not reflect the true measurement noise, since the true measurement noise is related to the true ship velocity which we do not know. More work is needed to estimate the ship centroid measurement noise from the subaperture images, such that the Kalman filter model reflects the true system more closely.

2. The restored high-resolution ship images from the proposed scheme can be used as the input to a ship classifier to enable automatic ship identification.

3. The proposed scheme may be modified to apply to stripmapping SAR images. Since the image formation of stripmapping SAR is different from that of spotlight SAR, a mathematical model of smear effect due to target motion in stripmapping SAR has to be derived first.

Appendix A

Approximation of Δu

In this Appendix, the approximation for the slant range variation Δu is shown in detail. The expression of the slant range variation Δu is shown in Equation (3.8), which is

$$\Delta u = \sqrt{(R_0 + y_0 + v_r t')^2 + (V_{radar} t' - v_c t' - x_0)^2} - \sqrt{(R_0 + y_0)^2 + (V_{radar} t' - x_0)^2}. \tag{A.1}$$

Both of the terms are expanded by Maclaurin series to second order. The first term is

$$\begin{aligned} & \sqrt{(R_0 + y_0 + v_r t')^2 + (V_{radar} t' - v_c t' - x_0)^2} \\ = \quad & \sqrt{(R_0 + y_0)^2 + x_0^2} + t' \frac{(R_0+y_0)v_r - x_0(V_{radar} - v_c)}{\sqrt{(R_0+y_0)^2 + x_0^2}} \\ & + \frac{t'^2}{2} \frac{v_r^2 + (V_{radar} - v_c)^2}{\sqrt{(R_0+y_0)^2 + x_0^2}} - \frac{t'^2}{2} \frac{[(R_0+y_0)v_r - x_0(V_{radar} - v_c)]^2}{[(R_0+y_0)^2 + x_0^2]^{3/2}}, \end{aligned}$$

and the second term is

$$\begin{aligned} & \sqrt{(R_0 + y_0)^2 + (V_{radar} t' - x_0)^2} \\ = \quad & \sqrt{(R_0 + y_0)^2 + x_0^2} + t' \frac{-x_0 V_{radar}}{\sqrt{(R_0+y_0)^2 + x_0^2}} \\ & + \frac{t'^2}{2} \frac{V_{radar}^2}{\sqrt{(R_0+y_0)^2 + x_0^2}} - \frac{t'^2}{2} \frac{(x_0 V_{radar})^2}{[(R_0+y_0)^2 + x_0^2]^{3/2}}. \end{aligned}$$

Therefore, (A.1) is rewritten into:

$$\begin{aligned} \Delta u \quad = \quad & t' \frac{(R_0 + y_0)v_r + x_0 v_c}{\sqrt{(R_0 + y_0)^2 + x_0^2}} + \frac{t'^2}{2} \frac{v_r^2 + v_c^2 - 2V_{radar} v_c}{\sqrt{(R_0 + y_0)^2 + x_0^2}} \\ & - \frac{t'^2}{2} \frac{(R_0 + y_0)^2 v_r^2 - 2v_r x_0 (R_0 + y_0)(V_{radar} - v_c) + x_0^2 v_c^2 - 2x_0 V_{radar} v_c}{[(R_0 + y_0)^2 + x_0^2]^{3/2}} \end{aligned} \tag{A.2}$$

In airborne spotlight SAR collection geometry, $R_0 \gg y_0$ and $R_0 \gg x_0$. If x_0 and x_0 are small, which means the point target is close to the patch center at $t' = 0$, then

$$\sqrt{(R_0 + y_0)^2 + x_0^2} \approx R_0 + y_0. \tag{A.3}$$

With the approximation in (A.3), (A.2) can be simplified to:

$$\begin{aligned} \Delta u &= v_r t' + t' \frac{x_0 v_c}{R_0 + y_0} + \frac{v_c^2}{2(R_0 + y_0)} t'^2 - \frac{V_{radar} v_c}{(R_0 + y_0)} t'^2 \\ &\quad - \frac{v_r x_0 (V_{radar} - v_c)}{(R_0 + y_0)^2} t'^2 + \frac{x_0^2 v_c^2 - x_0 V_{radar} v_c}{(R_0 + y_0)^3} t'^2 \end{aligned} \tag{A.4}$$

In airborne spotlight SAR, the patch size is usually relative small. To make sure that the moving point target is in the patch during the long integration time, we assume that the target's velocity is small. If $V_{radar} \gg v_r$, $V_{radar} \gg v_c$, and with the assumptions on x_0 and y_0, we can have the following approximations:

$$\begin{aligned} t' \frac{x_0 v_c}{R_0 + y_0} &\approx 0 \\ \frac{v_c^2}{2(R_0 + y_0)} t'^2 &\approx 0 \\ - \frac{v_r x_0 (V_{radar} - v_c)}{(R_0 + y_0)^2} t'^2 &\approx 0 \\ \frac{x_0^2 v_c^2 - x_0 V_{radar} v_c}{(R_0 + y_0)^3} t'^2 &\approx 0 \end{aligned}$$

Thus Δu in (A.4) is further simplified to:

$$\begin{aligned} \Delta u &= v_r t' - \frac{V_{radar} v_c}{R_0 + y_0} t'^2 \\ &\approx v_r t' - \frac{V_{radar} v_c}{R_0} t'^2. \end{aligned} \tag{A.5}$$

As a result, Δu is not related to x_0 and x_0. Equation (A.5) is the same as Equation (3.9).

Appendix B

Impulse Response Function

In this Appendix, we are going to examine the inverse Fourier transform $F^{-1}_{X',Y'}\{H_1(X',Y')\}$ and $F^{-1}_{X',Y'}\{H_2(X',Y')\}$ in Section 3.3, where X' and Y' are considered as continuous variables. X' represents the spatial frequency for cross-range, and Y' represents the spatial frequency for slant range.

Let $v_r \frac{T\lambda}{4\pi\Delta\theta} = a$ and $\frac{V_{radar}}{R_0} v_c (\frac{T\lambda}{4\pi\Delta\theta})^2 = b$, and $H_1(X',Y')$ and $H_2(X',Y')$ can be rewritten as:

$$H_1(X',Y') = e^{jaX'Y'} \tag{B.1}$$

and

$$H_2(X',Y') = e^{jbY'X'^2}. \tag{B.2}$$

We recall that Y' is confined to the region $\frac{2}{C}(\omega_0 + \alpha\tau_c) \leq Y' \leq \frac{2}{C}(\omega_0 - \alpha\tau_c)$, and X' is confined to $-\frac{2\pi}{\lambda}\Delta\theta \leq X' \leq \frac{2\pi}{\lambda}\Delta\theta$. That is to say, the Fourier data is confined by a rectangular window.

The 2-D inverse Fourier transform of $F(U,V)$ is defined as

$$f(u,v) = \frac{1}{4\pi^2} \int_{-\infty}^{\infty} \int_{-\infty}^{\infty} F(U,V) e^{i(Uu+Vv)} dU dV, \tag{B.3}$$

which can be viewed as two successive 1-D inverse Fourier transforms.

B.1 $F^{-1}_{X',Y'}\{H_1(X',Y')\}$

We assume that x' and y' are the continuous variables for cross range and slant range in image domain respectively.

$$\begin{aligned}
h_1(x',y') &= F^{-1}_{X',Y'}\{e^{jaX'Y'}\} \\
&= \frac{1}{4\pi^2}\int_{-2\pi\Delta\theta/\lambda}^{2\pi\Delta\theta/\lambda}[\int_{\frac{2}{C}(\omega_0-\alpha\tau_c)}^{\frac{2}{C}(\omega_0+\alpha\tau_c)} e^{jaX'Y'}e^{jY'y'}dY']e^{jX'x'}dX' \\
&= \frac{1}{4\pi^2}\int_{-2\pi\Delta\theta/\lambda}^{2\pi\Delta\theta/\lambda}\frac{4}{C}\alpha\tau_c e^{j\frac{2}{C}\omega_0(y'+aX')}sinc[\frac{2}{C\pi}\alpha\tau_c(y'+aX')]e^{jX'x'}dX' \\
&= \frac{1}{4\pi^2}\int_{-2\pi\Delta\theta/\lambda}^{2\pi\Delta\theta/\lambda}\frac{4}{C}\alpha\tau_c e^{j\frac{2}{C}\omega_0 a(X'+\frac{y'}{a})}sinc[\frac{2}{C\pi}\alpha\tau_c a(X'+\frac{y'}{a})]e^{jX'x'}dX' \\
&= F^{-1}_{X'}\{\frac{2}{C\pi}\alpha\tau_c e^{j\frac{2}{C}\omega_0 a(X'+\frac{y'}{a})}sinc[\frac{2}{C\pi}\alpha\tau_c a(X'+\frac{y'}{a})]W(X')\} \\
&= F^{-1}_{X'}\{\frac{2}{C\pi}\alpha\tau_c e^{j\frac{2}{C}\omega_0 a(X'+\frac{y'}{a})}sinc[\frac{2}{C\pi}\alpha\tau_c a(X'+\frac{y'}{a})]\} \\
&\quad *F^{-1}_{X'}\{W(X')\} \qquad \text{(B.4)}
\end{aligned}$$

where the *sinc* function is defined as

$$sinc(x) = \frac{sin(\pi x)}{\pi x}. \qquad \text{(B.5)}$$

$W(X')$ is a window function defined as

$$W(X') = \begin{cases} 1 & -2\pi\Delta\theta/\lambda \le X' \le 2\pi\Delta\theta/\lambda \\ 0 & \text{otherwise} \end{cases}. \qquad \text{(B.6)}$$

The inverse Fourier transform of $W(X')$ is $w(x')$,

$$w(x') = \frac{4\pi\Delta\theta}{\lambda}sinc(\frac{2\Delta\theta}{\lambda}x'). \qquad \text{(B.7)}$$

The inverse Fourier transform of the *sinc* function is

$$f(x') = F^{-1}_{X'}\{sinc[\frac{2}{C\pi}\alpha\tau_c aX']\} = \begin{cases} \frac{C}{4\alpha\tau_c a} & \mid x' \mid \le \frac{2\alpha\tau_c a}{C} \\ 0 & \text{otherwise} \end{cases}. \qquad \text{(B.8)}$$

Therefore, $h_1(x',y')$ in (B.4) becomes

$$h_1(x',y') = \frac{2}{C\pi}\alpha\tau_c f(x'+\frac{2}{C}\omega_0 a)e^{-jx'y'/a} * \frac{2\Delta\theta}{\lambda}sinc(\frac{2\Delta\theta}{\lambda}x'). \qquad \text{(B.9)}$$

As we can see in (B.9), $f(x')$ is shifted in cross-range dimension, which means the image is shifted by

$$\frac{2}{C}\omega_0 a = \frac{2}{C}\omega_0 v_r \frac{T\lambda}{4\pi\Delta\theta} = v_r T/\Delta\theta = v_r R_0/V_{radar}. \tag{B.10}$$

Since $f(x')$ is of rectangular shape, the image is smeared in cross-range dimension as well, where the smear length is given by

$$\frac{4\alpha\tau_c a}{C} = \frac{4\alpha\tau_c v_r \frac{T\lambda}{4\pi\Delta\theta}}{C} = \frac{2\alpha\tau_c}{\omega_0}\frac{v_r}{V_{radar}}R_0. \tag{B.11}$$

B.2 $F^{-1}_{X',Y'}\{H_2(X',Y')\}$

$$\begin{aligned} h_2(x',y') &= F^{-1}_{X',Y'}\{e^{jbX'^2Y'}\} \\ &= \frac{1}{4\pi^2}\int_{-2\pi\Delta\theta/\lambda}^{2\pi\Delta\theta/\lambda}\frac{4}{C}\alpha\tau_c e^{j\frac{2}{C}\omega_0(y'+bX'^2)} sinc[\frac{2}{C\pi}\alpha\tau_c(y'+bX'^2)]e^{jX'x'}dX' \\ &= \frac{1}{4\pi^2}\int_{-2\pi\Delta\theta/\lambda}^{2\pi\Delta\theta/\lambda}\frac{4}{C}\alpha\tau_c e^{j\frac{2}{C}\omega_0 b(X'^2+\frac{y'}{b})} \\ &\quad sinc[\frac{2}{C\pi}\alpha\tau_c b(X'^2+\frac{y'}{b})]e^{jX'x'}dX' \end{aligned} \tag{B.12}$$

Calculating the above integral at $y' = 0$ numerically, Figures B.1 and B.2 show the results with the parameters in Table 3.1. Figure B.1 shows the integral result for v_c=0.2m/sec, while Figure B.2 shows the result for v_c=0.5m/sec. We can see that there is no image shift in cross-range dimension. However, there is smear in cross-range dimension, where the smear length is proportional to v_c.

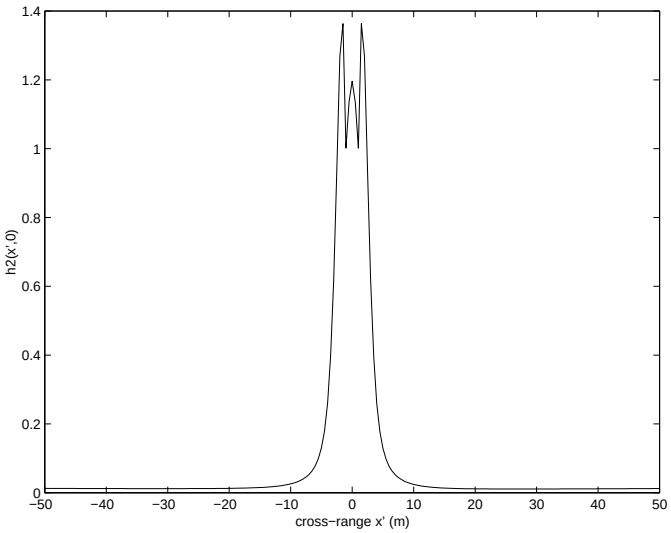

Figure B.1: Eq. (B.11) with v_c=0.2m/sec

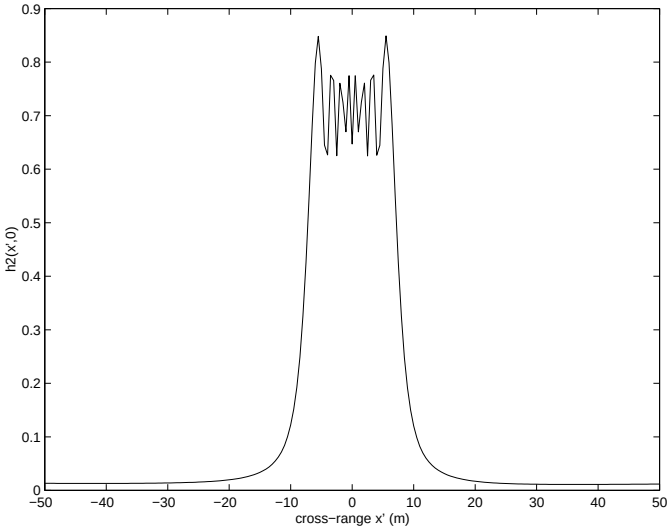

Figure B.2: Eq. (B.11) with v_c=0.5m/sec

Appendix C

Related Calculation in Centroid Estimation for Smeared Image

In this Appendix, the expressions for $E(I_i)$,$VAR(I_i)$ and $E[(I_i - E(I_i))(I_j - E(I_j))]$ are given, which are needed in Section 4.8 for the analysis of the centroid estimation variance in smeared images.

Recall that I_i is pixel intensity in smeared images. It is a weighted summation of pixel intensities in the corresponding unsmeared images as shown in (4.23). Here, we write down (4.23) again:

$$I_i = \mid h_1 \mid^2 I'_1 + \cdots + \mid h_{N-1} \mid^2 I'_{N-1} + \sum_{k<j} 2Re[h_k h_j^* v_k v_j^*]. \tag{C.1}$$

$\{h_i\}_{i=0}^{N-1}$ represents the impulse response due to the target motion. $\{I'_i\}_{i=0}^{N-1}$ represents the unsmeared image pixel intensity with mean intensity $\{I'_{i0}\}_{i=0}^{N-1}$, while $\{v_i\}_{i=0}^{N-1}$ is the unsmeared complex image. $\{I'_i\}_{i=0}^{N-1}$ are independent random variables. From Section 2.7, we know that

$$E(I'_i) = I'_{i0} \tag{C.2}$$

$$VAR(I'_i) = I'^2_{i0} \tag{C.3}$$

In addition, if we express v_i as $v_i = a_i + b_i i$, then a_i and b_i are independent and zero-mean Gaussian random variables with equal variance $I'_{i0}/2$. We denote a_i and b_i as: $a_i \sim N(0, I'_{i0}/2)$ and $b_i \sim N(0, I'_{i0}/2)$.

C.1 $E(I_i)$

From (C.1) and (C.2), we have

$$E(I_i) = \mid h_1 \mid^2 I'_{1\ 0} + \cdots + \mid h_{N-1} \mid^2 I'_{N-1\ 0} + 2\sum_{k<j} E(Re[h_k h_j^* v_k v_j^*]). \tag{C.4}$$

To find $E(Re[h_k h_j^* v_k v_j^*])$, we suppose $h_k h_j^* = x + yi$, $v_k = a_k + b_k i$, and $v_j = a_j + b_j i$. Then

$$\begin{aligned} E(Re[h_k h_j^* v_k v_j^*]) &= E(Re[(x+yi)(a_k+b_k i)(a_j - b_j i)]) \\ &= E(x(a_k a_j + b_k b_j) - y(b_k a_j - a_k b_j)) \\ &= x[E(a_k a_j) + E(b_k b_j)] - y[E(b_k a_j) - E(a_k b_j)] \end{aligned} \tag{C.5}$$

Since a_k, b_k, a_j and b_j are independent random variables with $a_k \sim N(0, I'_{k0}/2)$, $b_k \sim N(0, I'_{k0}/2)$, $a_j \sim N(0, I'_{j0}/2)$ and $b_j \sim N(0, I'_{j0}/2)$,

$$E(a_k a_j) = E(a_k)E(a_j) = 0. \tag{C.6}$$

With the same reason, $E(b_k b_j) = 0$, $E(b_k a_j) = 0$ and $E(a_k b_j) = 0$. Thus

$$E(Re[h_i h_j^* v_i v_j^*]) = 0. \tag{C.7}$$

As a result, (C.4) becomes

$$E(I_i) = \mid h_1 \mid^2 I'_{1\ 0} + \cdots + \mid h_{N-1} \mid^2 I'_{N-1\ 0}. \tag{C.8}$$

C.2 $VAR(I_i)$

With the expression of $E(I_i)$, $VAR(I_i)$ can be expanded as

$$\begin{aligned} VAR(I_i) &= E[(I_i - E(I_i))^2] \\ &= E[(\sum_k \mid h_k \mid^2 (I'_k - I'_{k0}) + \sum_{k<j} 2Re[h_k h_j^* v_k v_j^*])^2] \\ &= \sum_k \mid h_k \mid^4 I'^2_{k0} + \sum_{k<j} 4E(Re^2[h_k h_j^* v_k v_j^*]) \\ &\quad + \sum_{k<j} 2 \mid h_k \mid^2 \mid h_j \mid^2 E[(I'_k - I'_{k0}))(I'_j - I'_{j0})] \\ &\quad + \sum_{k1 \neq j1 \text{ or } k2 \neq j2} 8Re[h_{k1} h_{k2}^* v_{k1} v_{k2}^*] Re[h_{j1} h_{j2}^* v_{j1} v_{j2}^*] \\ &\quad + \sum_{l;k<j} 4 \mid h_l \mid^2 E\{(I'_l - I'_{l0}) Re[h_k h_j^* v_k v_j^*]\} \end{aligned} \tag{C.9}$$

To find out the second term in (C.9), we suppose $h_k h_j^* = x + yi$, $v_k = a_k + b_k i$, and $v_j = a_j + b_j i$. Since a_k, b_k, a_j and b_j are independent and zero-mean,

$$\begin{aligned} E(Re^2[h_i h_j^* v_i v_j^*]) &= E\{[x(a_k a_j + b_k b_j) - y(b_k a_j - a_k b_j)]^2\} \\ &= x^2 E[(a_k a_j + b_k b_j)^2] + y^2 E[(b_k a_j - a_k b_j)^2] \\ &= x^2[E(a_k^2 a_j^2) + E(b_k^2 b_j^2)] + y^2[E(b_k^2 a_j^2) + E(a_k^2 b_j^2)] \end{aligned} \quad (C.10)$$

Recall that for a zero-mean Gaussian random variable $x \sim N(0, \sigma^2)$,

$$E(x^2) = \sigma^2. \quad (C.11)$$

Hence, with the independence of a_k and a_j, $a_k \sim N(0, \frac{I'_{k0}}{2})$ and $a_j \sim N(0, \frac{I'_{j0}}{2})$ we have

$$\begin{aligned} E(a_k^2 a_j^2) &= E(a_k^2) E(a_j^2) \\ &= \frac{I'_{k0}}{2} \frac{I'_{j0}}{2}. \end{aligned} \quad (C.12)$$

With the same reason, we have

$$E(b_k^2 b_j^2) = E(b_k^2 a_j^2) = E(a_k^2 b_j^2) = \frac{I'_{k0}}{2} \frac{I'_{j0}}{2} \quad (C.13)$$

As a result, the second term in (C.9) becomes

$$\begin{aligned} E(Re^2[h_k h_j^* v_k v_j^*]) &= (x^2 + y^2) \frac{I'_{k0} I'_{j0}}{2} \\ &= | h_k h_j^* |^2 \frac{I'_{k0} I'_{j0}}{2} \\ &= | h_k |^2 | h_j |^2 \frac{I'_{k0} I'_{j0}}{2}. \end{aligned} \quad (C.14)$$

Since I'_k and I'_j are independent, the third term in (C.9)

$$E[(I'_k - I'_{k0})(I'_j - I'_{j0})] = 0. \quad (C.15)$$

With v_{k1},v_{k2},v_{j1} and v_{j2} are independent random variables, it can be shown that the fourth and fifth term in (C.9) are

$$E(Re[h_{k1} h_{k2}^* v_{k1} v_{k2}^*] Re[h_{j1} h_{j2}^* v_{j1} v_{j2}^*]) = 0 \quad (C.16)$$

and

$$E\{(I'_l - I'_{l0})Re[h_k h_j^* v_k v_j^*]\} = 0. \tag{C.17}$$

Therefore, $VAR(I_i)$ in (C.9) is simplified to

$$VAR(I_i) = \sum_k \mid h_k \mid^4 I'^2_{k0} + \sum_{k<j} 2 \mid h_k \mid^2 \mid h_j \mid^2 I'_{k0} I'_{j0}. \tag{C.18}$$

C.3 $E[(I_i - E(I_i))(I_j - E(I_j))]$

To calculate $E[(I_i - E(I_i))(I_j - E(I_j))]$, we suppose

$$I_i = \mid \sum_k h_{ik} v_k \mid^2 \tag{C.19}$$

$$I_j = \mid \sum_k h_{jk} v_k \mid^2 \tag{C.20}$$

Due to the independence of $\{I'_i\}_{i=0}^{N-1}$, it can be shown that

$$\begin{aligned}
& E[(I_i - E(I_i))(I_j - E(I_j))] \\
= \; & E\{[\sum_k \mid h_{ik} \mid^2 (I'_k - I'_{k0}) + \sum_{k<l} 2Re[h_{ik} h_{il}^* v_k v_l^*]] \\
& [\sum_k \mid h_{jk} \mid^2 (I'_k - I'_{k0}) + \sum_{k<l} 2Re[h_{jk} h_{jl}^* v_k v_l^*]]\} \\
= \; & \sum_k \mid h_{ik} \mid^2 \mid h_{jk} \mid^2 I'^2_{k0} + \sum_{k<l} E(4Re[h_{ik} h_{il}^* v_k v_l^*] Re[h_{jk} h_{jl}^* v_k v_l^*])
\end{aligned} \tag{C.21}$$

Let $h_{ik} h_{il}^* = x_1 + y_1 i$, $h_{jk} h_{jl}^* = x_2 + y_2 i$, $v_k = a_k + b_k i$, and $v_l = a_l + b_l i$, then

$$\begin{aligned}
& E(Re[h_{ik} h_{il}^* v_k v_l^*] Re[h_{jk} h_{jl}^* v_k v_l^*]) \\
= \; & E\{[x_1(a_k a_l + b_k b_l) - y_1(b_k a_l - a_k b_l)][x_2(a_k a_l + b_k b_l) - y_2(b_k a_l - a_k b_l)]\} \\
= \; & E[x_1 x_2 (a_k a_l + b_k b_l)^2 + y_1 y_2 (b_k a_l - a_k b_l)^2] \\
= \; & x_1 x_2 \frac{I'_{k0} I'_{l0}}{2} + y_1 y_2 \frac{I'_{k0} I'_{l0}}{2} \\
= \; & Re[h_{ik} h_{il}^* h_{jk}^* h_{jl}] \frac{I'_{k0} I'_{l0}}{2}.
\end{aligned} \tag{C.22}$$

As a result, (C.21) becomes

$$\begin{aligned}
& E[(I_i - E(I_i))(I_j - E(I_j))] \\
= \; & \sum_k \mid h_{ik} \mid^2 \mid h_{jk} \mid^2 I'^2_{k0} + 2 \sum_{k<l} Re[h_{ik} h_{il}^* h_{jk}^* h_{jl}] I'_{k0} I'_{l0}.
\end{aligned} \tag{C.23}$$

Bibliography

[1] H. C. Andrews and B. R. Hunt. *Digital Image Restoration.* Prentice-Hall, Inc., 1977.

[2] D. A. Ausherman, A. Kozma, J. L. Walker, H. M. Jones, and E. C. Poggio. "Developments in radar imaging". *IEEE Transactions on Aerospace and Electronic Systems*, 20(7):363–400, 1984.

[3] Y. Bar-Shalom and T. E. Fortmann. *Tracking and Data Association.* Academic Press, Inc., 1988.

[4] Y. Bar-Shalom, H. M. Shertukde, and K. R. Pattipati. "Use of measurements from an imaging sensor for precision target tracking". *IEEE Transactions on Aerospace and Electronic Systems*, 25(6):863–871, 1989.

[5] K. Brammer and G. Siffling. *Kalman-Bucy Filters.* Artech House Publishers, 1989.

[6] W. G. Carrara, R. S. Goodman, and R. M. Majewski. *Spotlight Synthetic Aperture Radar: Signal Processing Algorithms.* Artech House Publishers, 1995.

[7] C. K. Chui and G. Chen. *Kalman Filtering with Real-time Applications.* Springer-Verlag, 1987.

[8] J. C. Curlander and R. N. Mcdonough. *Synthetic Aperture Radar Systems and Singal Processing*, volume 1. John Wiley & Sons, 1991.

[9] J. C. Dainty. *Laser Speckle and Related Phenomena.* Springer-Verlag, 1975.

[10] J. P. Fitch. *Synthetic Aperture Radar.* Springer-Verlag, 1988.

[11] G. Franceschetti, V. Pascazio, and G. Schirinzi. "Iterative homomorphic technique for speckle reduction in synthetic aperture radar imaging". *Journal of the Optical Society of American, A: Optics and Image Science*, 12(4):686–694, 1995.

[12] R. C. Gonzalez and P. Wintz. *Digital Image Processing.* Addison-Wesley, 1977.

[13] A. D. Hillery and R. T. Chin. "Iterative wiener filters for image restorations". *IEEE Transactions on Signal Processing*, 39(8):1892–1899, 1991.

[14] T. Itoh, H. Sueda, and Y. Watanabe. "Motion compensation for ISAR via centroid tracking". *IEEE Transactions on Aerospace and Electronic Systems*, 32(3):1191–1197, 1996.

[15] A. Jain and I. Patel. "SAR/ISAR imaging of a nonuniformly rotating target". *IEEE Transactions on Aerospace and Electronic Systems*, 28(1):317–321, 1992.

[16] A. K. Jain. *Fundamentals of Digital Image Processing.* Prentice-Hall, Inc., 1989.

[17] C. V. Jakowatz, D. E. Wahl, P. H. Eichel, D. C. Ghiglia, and P. A. Thompson. *Spotlight-Mode Synthetic Aperture Radar: A Signal Processing Approach.* Kluwer Academic Publishers, 1996.

[18] D. T. Kuan, A. A. Sawchuk, T. C. Strand, and P. Chavel. "Adaptive noise smoothing filter for images with signal-dependent noise". *IEEE Transactions on Pattern Analysis and Machine Intelligence*, 7(2):165–177, 1985.

[19] D. T. Kuan, A. A. Sawchuk, T. C. Strand, and P. Chavel. "Adaptive restoration of images with speckle". *IEEE Transactions on Acoustics, Speech, and Signal Processing*, 35(3):373–382, 1987.

[20] N. Levanon. *Radar Principles.* John Wiley & Sons, 1988.

[21] J. S. Lim. *Two-Dimensional Signal and Image Processing.* Prentice-Hall, Inc., 1990.

[22] A. Lopes, R. Touzi, and E. Nezry. "Adaptive speckle filters and scene heterogeneity". *IEEE Transactions on Geoscience and Remote Sensing*, 28(6):992–1000, 1990.

[23] D. C. Munson. "A tomographic formulation of spotlight-mode synthetic aperture radar". *Proceedings of the IEEE*, 71(8):917–925, 1983.

[24] D. C. Munson and J. L. C. Sanz. "Image reconstruction from frequency-offset Fourier data". *Proceedings of the IEEE*, 72(6):661–669, 1984.

[25] D. C. Munson and R. L. Visentin. "A signal processing view of strip-mapping synthetic aperture radar". *IEEE Transactions on Acoustics, Speech, and Signal Processing*, 37(12):2131–2147, 1989.

[26] A. V. Oppenheim and R. W. Schafer. *Discrete-Time Signal Processing.* Prentice-Hall, Inc., 1989.

[27] E. Oron, A. Kumar, and Y. Bar-Shalom. "Precision tracking with segmentation for imaging sensors". *IEEE Transactions on Aerospace and Electronic Systems*, 29(3):977–987, 1993.

[28] H. M. Osman, L. Pan, S. D. Blostein, and L. Gagnon. "Classification of ships in airborne sar imagery using backpropagation neural networks". In *Radar Processing, Technology, and Applications, Proc. SPIE*, volume 3161, pages 126–136, 1997.

[29] A. Papoulis. *Probability, Random Variables, and Stochastic Processes.* McGraw-Hill, Inc., 1984.

[30] H. V. Poor. *An Introduction to Signal Detection and Estimation.* Springer-Verlag, 1988.

[31] R. K. Raney. "Synthetic aperture imaging radar and moving targets". *IEEE Transactions on Aerospace and Electronic Systems*, 7(3):499–505, 1971.

[32] Technology Service Corporation. "RIG - the radar imagery generator, version 3.0", 1996.

[33] S. Werness, W. Carrara, L. Joyce, and D. Franczak. "Moving target imaging algorithm for SAR data". *IEEE Transactions on Aerospace and Electronic Systems*, 26(1):57–67, 1990.

Vita

Yi Song

EDUCATION

Queen's University	M.Sc.	Electrical and Computer Engineering	1996–98
Shanghai Jiao Tong University	B.Sc.	Electrical Engineering	1991–95

EXPERIENCE

Research Assistant (1996–1998), Electrical and Computer Engineering, Queen's University

Teaching Assistant (1996–1997), Electrical and Computer Engineering, Queen's University